Optical properties of a two-dimensional electron gas in magnetic fields.

Marcin Z Drozdowa Byszewski

Thèse

Présentée par

Marcin Z DROZDOWA BYSZEWSKI

né 6 juillet 1975

Pour obtenir le titre de Docteur
de l'Université Joseph Fourier - Grenoble I
Spécialité : Physique

(Arrêtés ministériels du 5 juillet 1984 et 25 avril 2002)

Optical properties of a two–dimensional electron gas in magnetic fields.

Soutenue publiquement le 22 juillet 2005

Composition du jury :		
Gérard	Chouteau	président
Marek	Potemski	directeur de thèse
André	Raymond	rapporteur
Luis	Viña	rapporteur
Paul	Voisin	membre
Zbysław	Wilamowski	directeur de thèse

Thèse préparée au sein du
Laboratoire des Champs Magnétiques Intenses, CNRS, Grenoble

Abstract

This work presents the optical studies of the two–dimensional electron gas in magnetic fields. High magnetic fields part of the study concentrates on the effects resulting from electron – electron interactions in the regime of the fractional quantum Hall effect. The second, low magnetic fields part describes the recently discovered intriguing properties of the 2DEG under microwave irradiation.

The fractional quantum Hall effect is well known in the transport measurements and displays characteristic, easily recognisable series of features. Such series were until now not seen in optical experiments where only specific fractional filling factors were observed. The present work reports on optical detection of a whole family of $\nu = {}^{1}\!/_{2}$ fractional states that have been observed in photoluminescence in a series of samples. The features fall into easily recognisable pattern analogous to the one reflected by the magneto–resistivity traces. The strongest features observed in the photoluminescence experiments include $\nu = {}^{3}\!/_{7},\ {}^{2}\!/_{5},\ {}^{1}\!/_{3}$ and $\nu = {}^{3}\!/_{5},\ {}^{2}\!/_{3}$, 1 states on either side of the $\nu = {}^{1}\!/_{2}$ state, and are observed even in the raw data.

The analysis of the observed features as a function of well widths of the studied samples is presented. Applying similar reasoning as in the case of $\nu = 1$ it is said that the diametrally different behaviour shown by the samples photoluminescence is due to the interplay of the 2D electron – electron interactions and the 2DEG – valence band hole interactions.

The observed changes of the emission energy are interpreted as the effects of different states of the 2DEG that is being probed by an optically injected valence band hole. Depending on the 2DEG state, namely its incompressibility, the ability of the 2D electrons to screen the hole and form different quasi–excitonic complexes is changed. In the incompressible state the liquid is rigid, complexes can not be formed and emission occurs at higher energy. Thus, the region of higher energy emission is assumed to be an analogue of a R_{xy} quantum Hall plateau.

The initial and final states of the photoluminescence transitions at $\nu = {}^{1}\!/_{3}$ have been identified by numerical calculation and the peculiar temperature evolution of the measured spectra has been explained.

The inelastic light scattering experiments were performed to detect the excitations of the 2DEG. Two resonant Raman scattering signals originating

from the 2DEG excitations have been found. They have been interpreted as a spin–flip process and a scattering process to the Fermi energy of composite fermions. Additionally, a Raman scattering spin–flip process in a bulk GaAs has been identified.

The last chapter of the work describes the studies of the new effect of microwave resistance induced oscillations (MIROs). Very recently, this new effect has been discovered in the low magnetic field range. When irradiated with microwaves, the behaviour of 2DEG transport properties deviates strongly from the familiar Shubnikov – de Haas oscillations. The magneto–resistance traces exhibit series of vanishing resistance states.

The frequency dependence of transport data shows a gradual changeover from transport traces reflecting MIROs in low microwave frequencies, to traces showing nearly the cyclotron resonance only.

The experimental results of the direct absorption measurements presented here seem to validate the theoretical description of the MIROs as the result of oscillatory density of states. Also, the existence of two separate absorption processes are suggested to explain the microwave polarisation independence of MIROs, and the crossover from MIROs–like transport data at low frequencies to cyclotron–like traces at higher frequencies.

This work is organised as follows :

Chapter 1 introduces the concept of a two–dimensional electron gas and presents its basic properties in a magnetic field. Later, the quantum Hall effect is presented, based on transport measurements.

Chapter 2 presents the techniques and experimental set–ups used in the studies. Optical fibre systems for photoluminescence and photoluminescence excitation measurements are presented along with set–ups for microwave absorption and transport measurements.

In Chapter 3 describes the parameters of the studied systems.

Next, Chapter 4 contains results of transport and optics experiments performed to characterise the systems. The first part presents mostly the effect of illumination on the transport properties of the systems. The inter-band optics part presents studies of the zero field and integer quantum Hall effect regime studies and introduces the importance of the influence of the well width on the photoluminescence spectra.

Chapter 5, is focused on the optical studies of the 2DEG in the fractional quantum Hall regime. After a brief historical outline, it presents the novel experimental results with a theoretical description of the case of filling factor $\nu = {}^{1}\!/_{3}$. Then, the results of the inelastic light scattering experiments are presented.

Chapter 6 presents the studies of microwave absorption of a 2DEG in magnetic fields The effects of microwave irradiation on transport properties and direct microwave absorption studies are presented.

General conclusions are presented in Chapter 7.

Résumé

Propriétés optiques d'un gaz d'électrons bidimensionnel soumis à un champ magnétique.

Le sujet de ce travail de thèse est l'étude des propriétés d'un gaz électronique bidimensionnel (2DEG) soumis à un champ magnétique par des techniques de spectroscopie optique. Les effets à champs magnétiques intenses et à bas champs magnétiques sont étudiés : l'effet Hall quantique fractionnaire est étudié par photoluminescence et diffusion inélastique de la lumière, puis l'effet oscillatoire de la résistance induit par micro-ondes est étudié par transport et absorption des micro-ondes.

Les effets des interactions entre électrons du gaz bidimensionnel sont à l'origine de l'effet Hall quantique fractionnaire qui a fortement été étudié dans le passé par des techniques de transport. Le facteur de remplissage $\nu = {}^1\!/_3$ est le plus prononcé et a été découvert le premier. Une vraie gamme de fractions a en suite été observée. La symétrie et la forme des résultats en transport, similaires à celle de l'effet Hall quantique entier, ont suggéré l'introduction du model de fermions composites, un nouveau genre de quasi-particules.

Jusqu'à maintenant, les expériences d'optiques n'ont pas permis les études des interactions entre électrons sur toute la gamme de fractions. Les travaux précédents ne concernent que des fractions particulières.

Le travail présent rapporte l'observation des états de l'effet Hall quantique fractionnaire par photoluminescence. Les fractions $\nu = {}^1\!/_3,\ {}^2\!/_5,\ {}^3\!/_7,\ {}^3\!/_5,\ {}^2\!/_3$ et $\nu = 1$ sont clairement observées dans les spectres non traités et montrent une symétrie autour du facteur de remplissage $\nu = {}^1\!/_2$. Ces spectres sont analogues aux courbes de magnétorésistance d'un échantillon de haute qualité. La symétrie des fermions composites observée dans les états fractionnaires est un comportement bien connu de la résistance longitudinale.

Les variations d'énergie ont été attribuées au changement d'état du 2DEG. L'incompressibilité à un facteur de remplissage fractionnaire résulte de l'incapacité du 2DEG à écranter le potentiel positif du trou optique conduisant à une énergie d'émission élevée. Par contre, cette énergie est

diminuée à l'extérieur d'un état incompressible de 2DEG, car les électrons ont la possibilité de répondre au potentiel du trou.

Des estimations théoriques ont été faite pour le cas du facteur de remplissage $\nu = {}^1\!/_3$. L'émission de haute énergie a été attribuée à un quasi-exciton et l'émission de basse énergie observée en dehors d'un facteur de remplissage fractionnaire prévient d'un complexe formé d'un quasi-exciton et d'une quasi-particule.

Les zones de champ magnétique dans lesquelles l'énergie d'émission est élevée, ont été interprétées comme des analogues aux plateaux de Hall observés dans les mesures de transport. Ceci a été confirmé par des mesures de transport et de photoluminescence simultanées. Les mesures simultanées ont été précèdes par des études d'effet d'illumination sur les propriétés de transport. Les changements dramatiques de la densité électronique et des formes des courbes ont été observés. Enfin, un état stable a été trouvé correspondant à l'état détecté par les mesures optiques.

La dépendance de la luminescence en température montre un rétrécissement de la largeur de l'étendue d'énergie d'émission élevée, un effet connu des mesures de transport. Si la température est augmentée, le saut d'énergie d'émission se déplace en champ magnétique vers le centre du plateau de Hall. Cet effet est clairement visible à $\nu = {}^1\!/_3$.

Les mesures dans le régime de l'effet Hall quantique fractionnaire ont été précédées par des caractérisations des échantillons. Les paramètres standard du 2DEG, comme la concentration d'électrons et la masse effective ont été déterminées par des mesures optiques et de transport.

Les trois échantillons avec des puits quantiques ont été classifiés en fonction des différents rapports entre les énergies d'interaction électron - électron et électron - trou. Ce rapport détermine les caractéristiques de la luminescence de chaque échantillon.

L'influence de la largeur de la puit quantique sur la photoluminescence est discutée par rapport à l'exemple connu du facteur de remplissage $\nu = 1$. Les trois échantillons sont les représentants de trois valeurs différentes de l'interaction électron - trou par rapport à l'interaction électron - électron. L'émission de l'échantillon de puit quantique 10nm est approximativement indépendante du facteur du remplissage car le trou induit optiquement retient un électron et forme un exciton neutre ou un exciton chargé négativement. Dans les deux cas, les corrélations entre électrons sont détruites.

L'émission des autres puits quantiques présente un changement d'énergie. L'émission de puit quantique de 20nm montre une augmentation de l'énergie d'émission et l'émission de puit quantique NTT-C de 50nm montre une diminution de l'énergie d'émission. Les deux se situent dans le régime ou l'interaction entre électrons et l'interaction électron - trou sont comparables. Dans le puit quantique de 20nm, l'interaction électron - trou est plus grande, alors que dans le puit quantique de 50nm l'interaction entre les électrons est plus grande. Ces régimes différents seront utilisés pour l'explication des différents

comportements dans la région d'effet Hall quantique fractionnaire.

La deuxième partie de la thèse, présente les études d'un nouvel effet oscillatoire de la résistance induit sous irradiation micro-onde. A bas champ magnétique, sous irradiation micro-onde, les propriétés de transport s'écartent nettement des oscillations bien connues de Shubnikov - de Haas pour évoluer vers une série d'états de résistance zéro. Les oscillations sont définies par le rapport de la fréquence des micro-ondes et de la fréquence de la résonance cyclotron. La dépendance du transport en fonction de la fréquence et la puissance de micro-ondes est présentée. Un changement de courbes de transport des MIROs vers une forme qui ressemble à la résonance cyclotron est présenté.

Aussi, les résultats des mesures d'absorption des micro-ondes sont présentés pour deux échantillons avec des mobilités d'électrons différentes. L'échantillon de basse mobilité montre seulement une absorption autour de la résonance cyclotron. Par contre, le deuxième échantillon de haute mobilité montre aussi des signaux d'absorption aux harmoniques de la résonance cyclotron. Ces spectres différents d'absorption sont accompagnés par des courbes de transport différentes car l'échantillon de haute mobilité montre des MIROs beaucoup plus prononcés.

Les mesures ont permis d'inférer l'existence de deux processus d'absorption différents et séparés. L'absorption non résonante est mieux visible en transport et observée comme les MIROs, qui vraisemblablement ne respectent pas les règles de polarisation. Au contraire, l'absorption résonante, mieux observée dans les mesures d'absorption des micro-ondes, suit probablement les règles de polarisation de résonance cyclotron.

Acknowledgements

I would like to thank Marek Potemski, my thesis supervisor in the Grenoble High Magnetic Field Laboratory, for accepting me as his PhD student. I am grateful for his invaluable guidance, support and understanding.

I would like to thank Zbysław Wilamowski, my thesis supervisor in the Institute of Physics, Polish Academy of Sciences, in Warsaw, first for accepting me as his PhD student, and later giving me the possibility to continue my research in Grenoble.

I would like to thank the members of the jury: Gérard Chouteau, the president of the jury, Luis Viña and André Raymond, the two referees that had to struggle with reading through the manuscript in such a short time. Paul Voisin, for agreeing to take part in the jury.

I would like to thank Gérard Martinez, the director of the GHMFL for giving me the opportunity to work in the laboratory and providing with financial support for scientific conferences I participated.

Special thanks must go to Marcin Sadowski, for the task of proofreading the manuscript. Any mistakes left are there because he was finally overwhelmed by their number. I also greatly enjoyed working together with Sergei Studenikin from IMS–NRC, Ottawa, both in Grenoble and in Ottawa, and would like to thank him and Andy Sachrajda for their warm welcome during my stay in Canada.

During my stay in the laboratory I have met many people to whom I should say *thank you*: Roman Stępniewski, Andrzej Wysmołek, Adam Babiński, for many enlightening hours in the laboratory. Herbert Krath, methodical guardian of our lasers. Jean Florentin, magician, who brings into existence any dreamt-up part of any experimental setup. Duncan Maude, Wilfried Desrat, for bringing me a bit closer to transport measurements and the help with the dilution fridge. Stéphane Linger, for the introduction into the workings of the production of high magnetic fields. Sébastien Buisson, for carrying on his mundane task of keeping in shape the now essential part of the everyday work. Adeline Richard, struggling to create a computerised PL measurement centre. Ingrid Girardet, Walter Joss, for taking care of my relationships with the Max-Planck-Institut headquarters in Stuttgart. Paweł Hawrylak, Arkadiusz Wójs for the discussions on the photoluminescence in the regime of FQHE as seen from the point of view of

a theoretical physicist. Gislaine Meneroud, Amélie Pic, for all the help they have given while guiding me through the administrative labyrinths of the CNRS. Eric Mossang, Christiane Warth-Martin for their efficient planning of magnet time. Laurent Lozano, Régis Milanole, for late night discussions and weekends at the laboratory magnet sites. Sébastien Moreau, Benjamin Piot, the PhD students I worked with who helped me greatly by turning my phrases into proper French. Barbara Chwalisz, Oleh Fedorych, Andreas Gröger, Clemens Koerdt, Francisco Teran, Markus Weiss, with whom I had the pleasure to share an office.

I am grateful to the Studium Doktoranckie, IFPAN for financial support during my stay in Institute of Physics, PAN in Warsaw. I am grateful to the Max-Planck-Institut für Festkörperforschung for financial support since I started my PhD studies in Grenoble.

Again, I want to thank Marek and Marcin for their time, which I valued the most.

Last, I would like to thank my Friends, who can not be mentioned, who remembered me when I was away in the laboratory, and above all my Parents and Kamila for their love.

Grenoble, 3rd August 2005

Table of Contents

Chapter 1

Introduction

Ce premier chapitre d'introduction présente les propriétés de base d'un système bidimensionnel électronique sous champs magnétiques dans l'approximation d'un électron unique. La quantification de Landau des niveaux d'énergie et le concept d'énergie de Fermi sont présentés. Les phénomènes connus, observés dans les expériences de transport sont particulièrement discutés. Les oscillations de Shubnikov - de Haas à bas champ magnétique sont suivies par l'effet Hall quantique entier puis fractionnaire dans la limite quantique. L'effet fractionnaire est présenté avec une brève présentation de la théorie de Laughlin et du modèle de fermions composites.

1.1 2D electron gas in magnetic fields

A two–dimensional electron gas can be obtained by using different methods. The materials of choice are GaAs and AlGaAs as their different energy gaps provide the confining potential while roughly the same (Fig. 1.1) lattice constants allow high quality interfaces and thus, high mobility 2D electron systems.

The 2DEG in GaAs/AlGaAs based structures can be realised in two types of structures: heterojunctions (HJ) and quantum wells (QW). Both are grown by the molecular beam epitaxy (MBE) method.

The heterojunctions have, in general, higher mobilities as only one interface is present in the vicinity of the 2DEG. Quantum well structures usually have lower mobility 2DEG than heterojunctions because of the existence of material interfaces on both sides of the 2DEG.

The achieved mobilities in GaAs/AlGaAs structures are as high as $\sim 50 \cdot 10^6 cm^2/Vs$, which corresponds to a mean scattering time $\tau = 2 \cdot 10^{-9} s$ or mean free path $l \sim 0.26 mm$. Such high mobilities are important for high speed electronics.

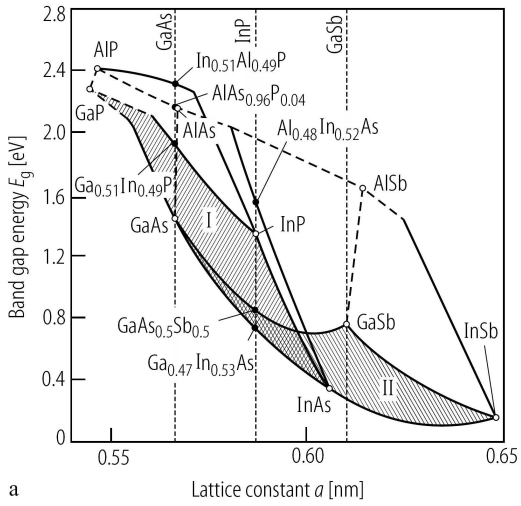

Figure 1.1: *The band gap as a function of the lattice constant for various ternary III-V alloys. Figure from [1].* $E_g(GaAs) = 1.5191eV$, $E_g(Al_xGa_{1-x}As)_{x=0.35} = 2.02eV$

1.1.1 Energy structure

Without an external magnetic field the motion of electrons in a quantum well is unconstrained in the quantum well plane but confined along the crystal growth direction. This confinement gives rise to the appearance of energy subbands. Each energy subband has a constant density of states (DOS) (Figure 1.2, left) which is given by:

$$D_{2D} = \frac{m*}{\pi\hbar^2} \tag{1.1}$$

where m* is the effective mass. For $m^* = 0.067m_0$, characteristic for GaAs, the density of states is equal to $D_{2D} = 2.79 \cdot 10^{10} meV^{-1}cm^{-2}$ (including the spin degeneracy).

The introduction of a magnetic field B perpendicular to the 2DEG plane results in an additional quantisation of the particles' motion into cyclotron orbits. The frequency of the precession is called *cyclotron frequency* and is equal to:

$$\omega_c = \frac{eB}{m^*} \tag{1.2}$$

and the cyclotron motion orbit radius is given by the magnetic length:

$$l_B = \sqrt{\frac{\hbar}{eB}} \tag{1.3}$$

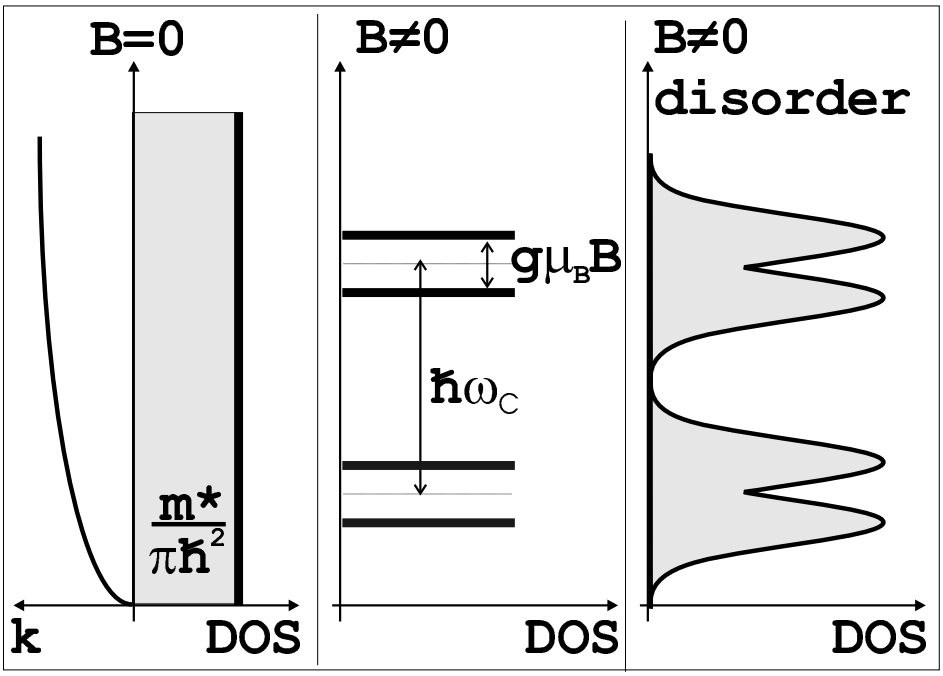

Figure 1.2: *DOS quantisation in magnetic fields. Left. Zero field case. Energy dispersion and constant DOS in an energy subband. Centre. Landau level quantisation at an arbitrary magnetic field in a disorder free system. Right. Landau level broadening due to disorder.*

$l_B(10T) = 8nm$ and $l_B(30T) = 4.6nm$.

The cyclotron motion in the plane of the 2DEG introduces an energy quantisation into the harmonic oscillator eigenenergies determined by the quantum number n. The cyclotron energy gap is equal to $\hbar\omega_c = 1.728meV/T$ for $m* = 0.067m_0$ The introduction of the electron spin splits the energy levels into spin–up and spin–down states by the Zeeman energy $E_Z = q\mu_B B = 25\mu eV/T$ for $g = -0.44$, characteristic for GaAs. The total energy of a Landau level is given by:

$$E_{n,\pm} = \left(n + \frac{1}{2}\right)\hbar\omega_c \pm \frac{1}{2}g\mu_B B \tag{1.4}$$

where g is the electron g-factor and μ_B is the Bohr magneton. Figure 1.2, centre, presents a Landau level quantisation of the density of states in the absence of disorder. The arrows represent characteristic values of energy gaps present in the one–particle picture.

The disorder broadens the δ–like energy levels into energy bands pictured on the right–hand side of Figure 1.2. The shape of the broadened levels may be described by a Lorentz function with $\Gamma \sim \sqrt{B}$ width [2].

For small enough magnetic fields the broadened Landau levels overlap, producing a modulation of the density of states without creating any energy gap (Figure 1.3). In the case of a strong magnetic field, when the cyclotron energy $\hbar\omega_c$ is greater than Landau level width, an energy gap exists (at least in terms of the mobility gap). Each Landau level degeneracy is given by:

$$D = \frac{e}{h}B \tag{1.5}$$

which is equal to $D = 2.4 \cdot 10^{10} cm^{-2}/T$ states per Landau spin–split level.

The density of states $G(E, B)$ can be described by a sum of Lorentz functions centred around E_n, $n = 0, 1 \ldots$:

$$g(E,B) = \frac{G(E,B)}{G_0} = \frac{\hbar\omega_c}{\pi\Gamma}\sum_n^{\infty}\frac{1}{1+\left(\frac{E-E_n}{\Gamma}\right)^2} \tag{1.6}$$

where Γ is the level width. In the case of sufficiently strong overlap of Landau levels, i.e. low magnetic fields, the density of states can be approximated by a simple oscillatory function:

$$\begin{aligned} g(E,B) &= 1 + 2\cdot\sum_s^{\infty} e^{-\frac{2\pi\Gamma s}{\hbar\omega_c}}\cdot\cos\left(\frac{2\pi E s}{\hbar\omega_c} - \pi s\right) \\ &\approx 1 + 2\cdot e^{-\frac{2\pi\Gamma}{\hbar\omega_c}}\cdot\cos\left(\frac{2\pi E}{\hbar\omega_c} - \pi\right) \end{aligned} \tag{1.7}$$

It is worth noting that even at high magnetic fields when the centres of Landau levels are well separated, there might be still a non – vanishing density of states in between the levels. These states in between are considered to be localised, i.e. they do not contribute to transport but may be seen by other methods [3, 4, 5].

1.1.2 Properties

The Fermi energy

The total number of electrons n_e can be defined as the number of occupied states which at a given temperature is written as:

$$n_e = \int_{-\infty}^{+\infty} G(E)\cdot f(E,kT)\, dE \tag{1.8}$$

where $G(E)$ is the density of states and $f(E, kT)$ is the Fermi distribution function of 2D electrons at temperature T. The Fermi distribution function

defines a Fermi energy E_F as the energy value where $f(E_F) = {}^1\!/_2$. Due to the constant density of states in a two–dimensional system (Eq. 1.1) the Fermi energy is determined by the electron concentration:

$$E_F = n_e \frac{\pi\hbar^2}{m*} \tag{1.9}$$

As an example, the Fermi energy for a 2D electron concentration $n_e = 2 \cdot 10^{11} cm^{-2}$ in the NTT-A GaAs/AlGaAs quantum well (i.e. one of the samples investigated in this work) is $E_F = 2/2.79 \cdot 10 = 7.16 meV$.

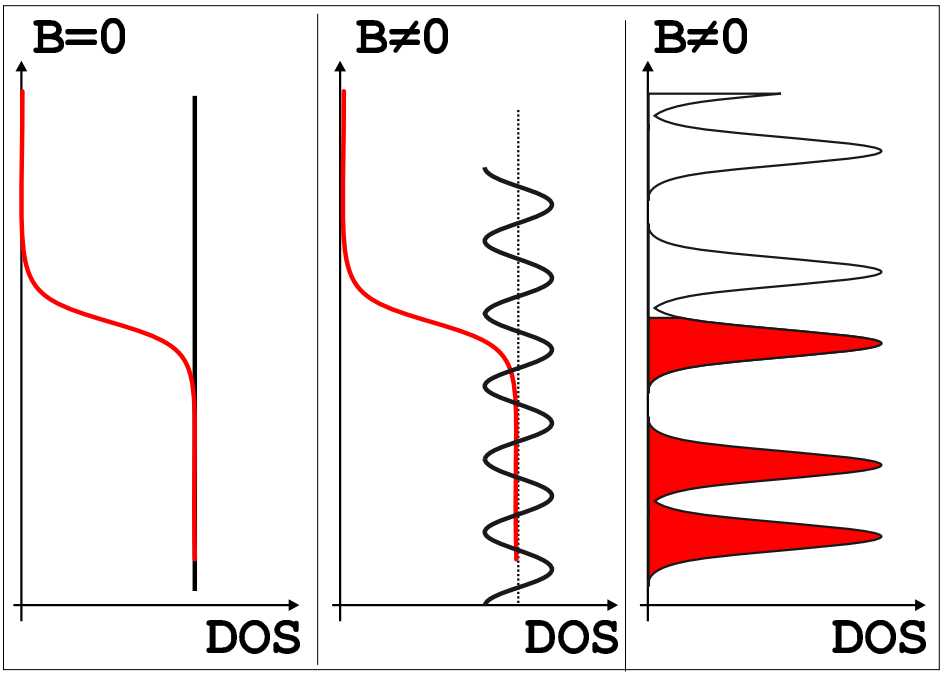

Figure 1.3: *DOS modulation in a magnetic field. Electron Fermi distribution function (red).*

Filling factor

In the high field limit the DOS is quantised into Landau levels. The Fermi energy is determined by the magnetic field via the cyclotron gap and the degeneracy of Landau levels. One can define a *filling factor* ν as:

$$\nu = \frac{n_e}{D} = \frac{n_e}{\frac{e}{h}B} \tag{1.10}$$

indicating the number of occupied Landau levels at a given magnetic field. The position of filling factor $\nu = 1$ where the first Landau level is fully

occupied while higher Landau levels are empty (at zero temperature) is related to the Fermi energy (at zero field) and electron concentration by the relation (for GaAs):

$$B_{\nu=1}(T) \;=\; 4.14 \cdot n_e(10^{11} cm^{-2}) \;=\; 1.155 \cdot E_F(meV) \qquad (1.11)$$

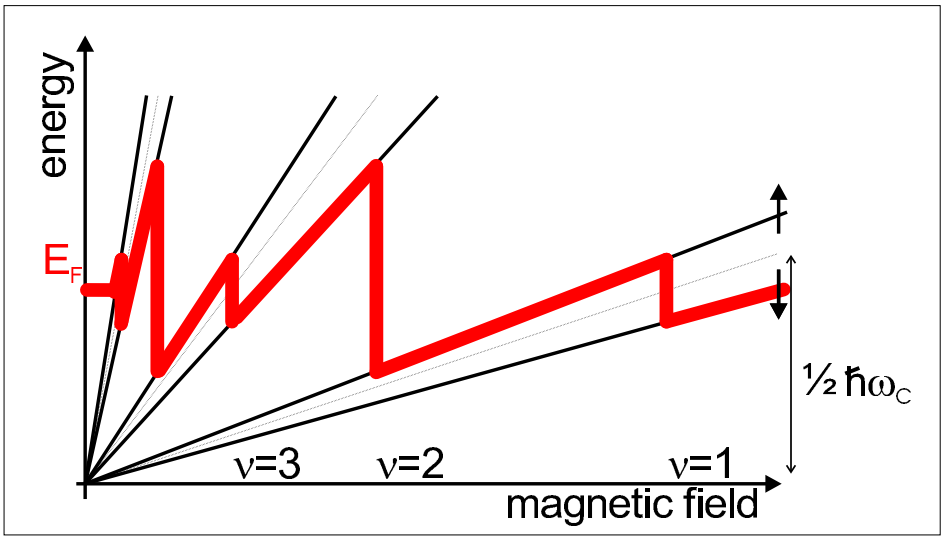

Figure 1.4: *Landau level fan chart. The zero field Fermi energy can be found in the middle between two subsequent Landau levels exactly at integer filling.*

Figure 1.4 illustrates changes in the Fermi energy due to the Landau level quantisation at zero temperature and assuming discrete levels. Due to the changes in the level degeneracy more electron can be accommodated into each Landau level as the magnetic field is increased.

Specific values of the magnetic field exist at which a Landau level (n) is fully occupied while level $(n+1)$ is completely empty. Those values of magnetic field correspond to integer values of the filling factor $\nu = 2(n+1)$. At these points the Fermi energy exhibits a discontinuity and jumps between the two levels. The Fermi energy exactly at integer filing factors is equal to the zero field value and is placed in the middle between the subsequent levels.

In between the integer filling factors the Fermi energy follows a given Landau level.

1.2 Conductivity in magnetic field

A possible geometry of a transport measurement of the 2DEG conductivity is shown in Figure 1.5. The external magnetic field $\overrightarrow{B}$ is applied perpendicular

to the 2D electron gas plane, along the z axis. The electric field $\overrightarrow{E}$ is applied along the x axis. The magneto–resistivity (conductivity) is determined by measuring the voltage V_X parallel to $\overrightarrow{E}$. The measurement is accompanied by simultaneous measurement of the Hall voltage V_H, perpendicular to $\overrightarrow{E}$ and $\overrightarrow{B}$.

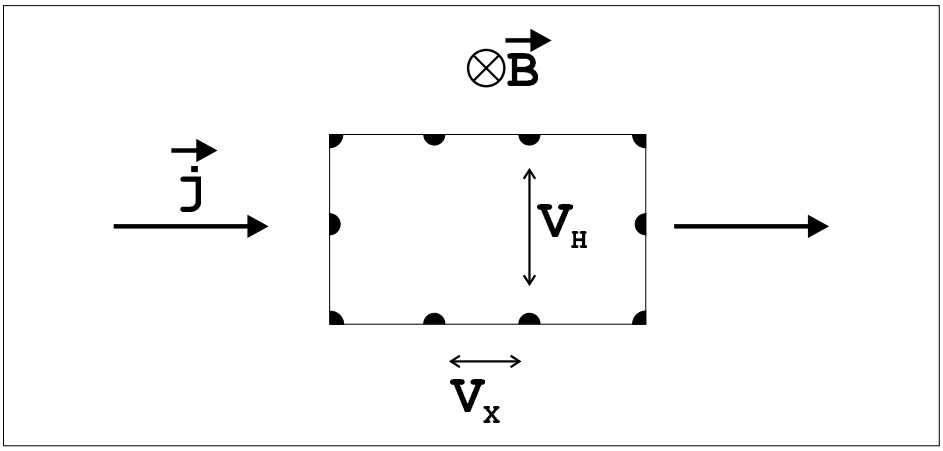

Figure 1.5: *Geometry of the NTT-A sample for transport measurements.*

1.2.1 Resistivity tensor

The current density $\overrightarrow{j}$ due to the applied electric field $\overrightarrow{E}$ along the x axis is equal to:

$$\overrightarrow{j} = \widehat{\sigma} \cdot \overrightarrow{E} = \begin{pmatrix} \sigma_{xx} & \sigma_{xy} \\ -\sigma_{xy} & \sigma_{yy} \end{pmatrix} \cdot \overrightarrow{E} \tag{1.12}$$

where $\widehat{\sigma}$ is the conductivity tensor. Defining the resistivity tensor $\widehat{\rho} = \widehat{\sigma}^{-1}$ one can write the expressions for the longitudinal and transverse components of the resistivity, values usually measured in experiment, as:

$$\begin{aligned} \rho_{xx} &= \frac{\sigma_{xx}}{\sigma_{xx}^2 + \sigma_{xy}^2} \\ \rho_{xy} &= \frac{\sigma_{xy}}{\sigma_{xx}^2 + \sigma_{xy}^2} \end{aligned} \tag{1.13}$$

given that $\sigma_{xx} = \sigma_{yy}$ and $\sigma_{xy} = -\sigma_{yx}$.

From the above equations it is evident that if $\rho_{xx} \to 0$ then $\sigma_{xx} \to 0$. In the high field limit when $\sigma_{xx} \ll \sigma_{xy}$ we can write a simple approximation:

$$\rho_{xx} \sim \frac{\sigma_{xx}}{\sigma_{xy}^2} \tag{1.14}$$

$$\sigma_{xx} \sim \frac{\rho_{xx}}{\rho_{xy}^2} \tag{1.15}$$

1.2.2 Shubnikov – de Haas oscillations — low magnetic fields

The modulation of the density of states by the applied magnetic field changes the conductivity of the 2DEG. The resultant oscillations are called Shubnikov – de Haas (SdH) oscillations [6]. In a simple approximation, the conductivity can be described by the following formula:

$$\rho_{xx}(B) \sim \sigma_{xx}(B) \cong \int_{-\infty}^{\infty} g(E,B)\left(-\frac{df}{dE}\right)dE \tag{1.16}$$

Substituting the Fermi distribution function and the density of states from Eq.1.7 one can write:

$$\Delta\sigma_{xx} \approx \frac{\frac{2\pi^2 kT}{\hbar\omega_c}}{sh\left(\frac{2\pi^2 kT}{\hbar\omega_c}\right)} \cdot e^{\frac{-2\pi\Gamma}{\hbar\omega_c}} \cdot \cos\left(\frac{2\pi E_F}{\hbar\omega_c}\right) \tag{1.17}$$

The above equation can be simplified into two temperature regimes:

$$\Delta\sigma_{xx} \approx \begin{cases} e^{\frac{-2\pi\Gamma}{\hbar\omega_c}} \cdot \cos\left(\frac{2\pi E_F}{\hbar\omega_c}\right) & for\ \frac{2\pi^2 kT}{\hbar\omega_c} \ll 1 \\ \frac{2\pi^2 kT}{\hbar\omega_c} \cdot e^{\frac{-\left(2\pi^2 kT + 2\pi\Gamma\right)}{\hbar\omega_c}} \cdot \cos\left(\frac{2\pi E_F}{\hbar\omega_c}\right) & for\ \frac{2\pi^2 kT}{\hbar\omega_c} \gg 1 \end{cases} \tag{1.18}$$

In the low temperature regime the temperature does not enter into the equation and does not produce any change in the oscillation amplitude. The damping parameter of the oscillations is determined solely by the Γ Landau level width.

On the other hand, when the temperature is increased the thermal distribution becomes important in the exponent $\sim (2\pi^2 kT + 2\pi\Gamma)$ of the damping factor.

Figure 1.6 presents a modulated density of states (G, red) due to a non–zero magnetic field. The Fermi distribution function (f) at a finite temperature is presented in black. Its derivative (blue) selects the region where σ_{xx} is sensitive to the density of states according to Eq. 1.16.

In the presented case the thermal distribution of the electrons spans over several Landau levels. Thus the oscillations will be blurred by the thermal effects (see 1K,red in Figure 1.7). In the low temperature case,

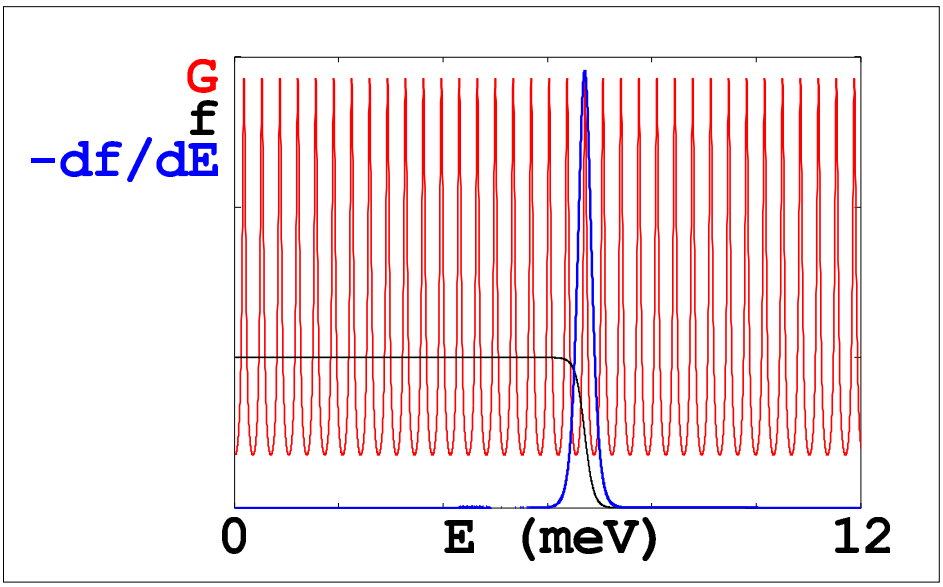

Figure 1.6: *Schematic presentation of DOS modulation (red), Fermi distribution function and its derivative. Parameters for the calculation are as follows:* $B = 0.2T$, $\Gamma = 0.05meV$, $E_f = 6.7meV$, $T = 1K$

the thermal distribution is narrow, the thermal blurring is suppressed and the SdH oscillations become intense. The case of T=30mK is presented in Figure 1.7, blue.

Figure 1.8 presents, for comparison, a R_{xx} trace of a very high quality sample. At bath temperature T=30mK the SdH oscillations are visible at magnetic fields as low as $\sim 23mT$. Spin splitting of the Landau levels becomes visible at $\sim 0.1T$.

1.2.3 Integer quantum Hall effect — high magnetic fields

The quantum Hall effect was discovered in 1980 by K. von Klitzing et al. [8].

At some value of the magnetic field, the R_{xx} trace starts to deviate from the Shubnikov – de Haas oscillations (see Figure 1.9). Whenever the system approaches an integer filling factor ν the magneto–resistivity displays minima which eventually transform into broad zero resistance states. In the regions of the magnetic field where the longitudinal resistance vanishes the transverse (Hall) resistivity has a constant value. The value of R_{xy} at the plateaus is quantised to:

$$R_{xy} = \frac{1}{n}\frac{h}{e^2} \tag{1.19}$$

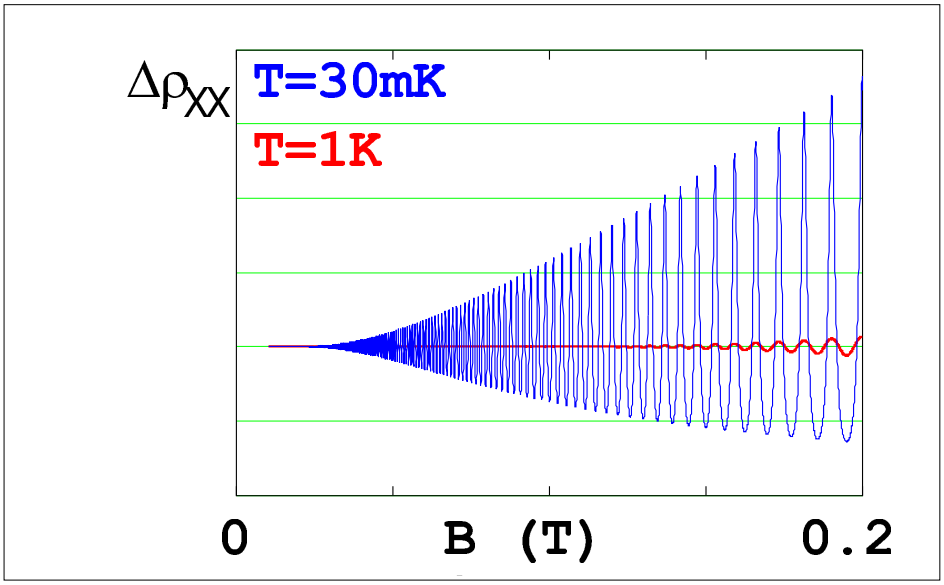

Figure 1.7: *Calculated SdH oscillations for two different temperatures:* $T = 1K$, $T = 30mK$. *Other parameters are the same as in previous figure:* $\Gamma = 0.05meV$, $E_f = 6.7meV$

where n is an integer, $h/e^2 = 25.812k\Omega$.

The quantisation of the density of states into the Landau levels alone can not explain the observation of the plateaus in an ideal (disorder free) system.

The existence of localised states in the tails of the impurity-broadened Landau level has been proposed (Figure 1.10). The electrons in the localised states do not contribute to the conductivity. The energy region where localised states exist is called the mobility gap. Whenever the Fermi energy lies in the mobility gap the system becomes insulating and the transport curves display integer quantum Hall plateaus.

On the other hand the extended states exist in the centre of a Landau level. The system enters a metallic phase whenever the Fermi energy lies in the region of extended states.

1.2.4 Fractional quantum Hall effect — quantum limit

Below the last integer filling factor $\nu = 1$ the changes between the metallic and insulating phases continue to be observed, even though the system is fully spin polarised in the lowest Landau level and no energy gap is expected to exist in the single particle picture used so far.

The most pronounced feature of the fractional quantum Hall effect is visible at a fractional filling factor $\nu = {}^1\!/_3$. The discovery of a mobility gap at

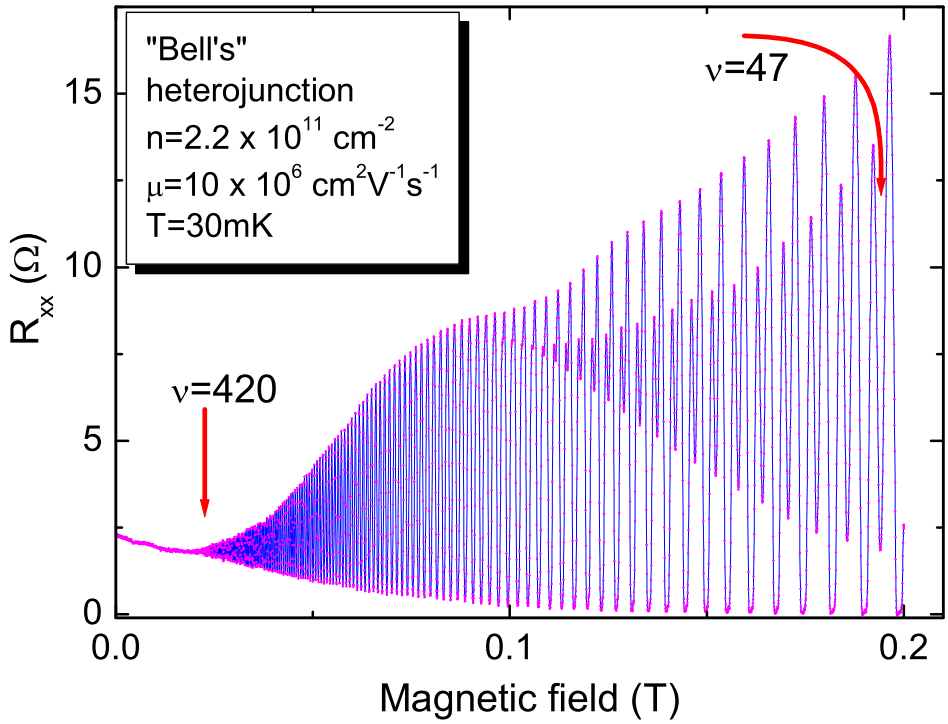

Figure 1.8: *SdH oscillations in a very high mobility heterojunction sample at* $T = 30mK$*.[7]*

this filling factor was made by Tsui et al. [9] in 1982. The magneto–transport experiment on a GaAs/AlGaAs heterojunction structure showed, at low temperature, a R_{xy} deviation from the linear dependence at a magnetic field exactly three times greater than that of the filling factor $\nu = 1$.

From the experimental point of view the fractional quantum Hall effect resembles the integer effect in the behaviour of both Hall and longitudinal resistivity. The former has plateaus quantised to *fractional* values of h/e^2 and the latter drops to zero at corresponding magnetic fields.

Later experiments showed that the series of possible fractions can be described by:

$$\nu = \frac{p}{2mp \pm 1} \tag{1.20}$$

where m and p are integers. A hierarchical scheme has been conceived to explain the appearance of different states. In the scheme all known *daughter states* $\nu = {}^{p}/_{q}$ (q-odd) are based on the primitive $\nu = {}^{1}/_{q}$ states.

The following properties of the odd-denominator fractions have been established:

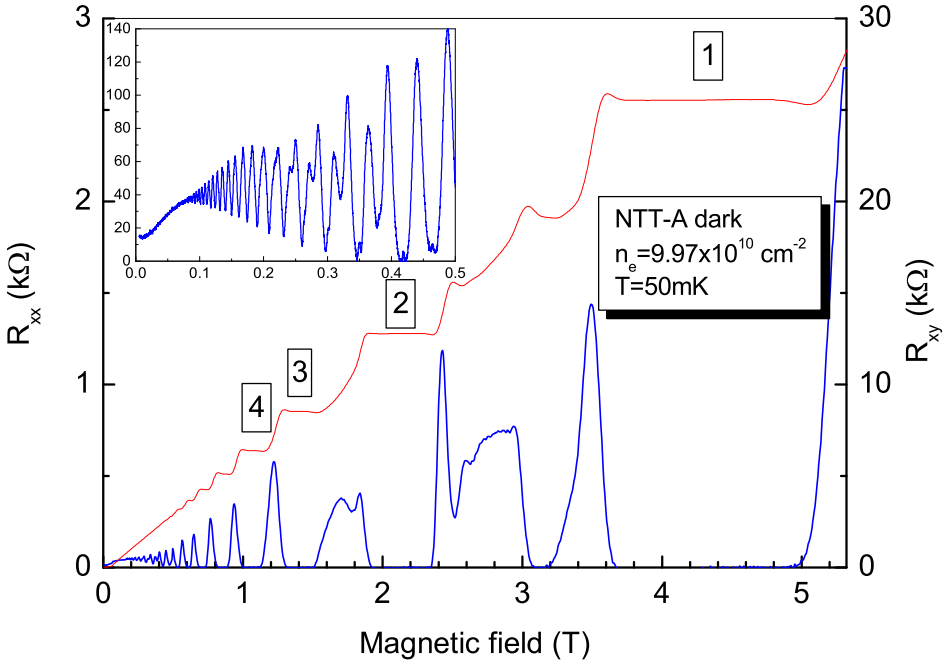

Figure 1.9: *Example of the integer quantum Hall effect measured on one of the samples investigated in this work. (unilluminated NTT-A quantum well sample).*

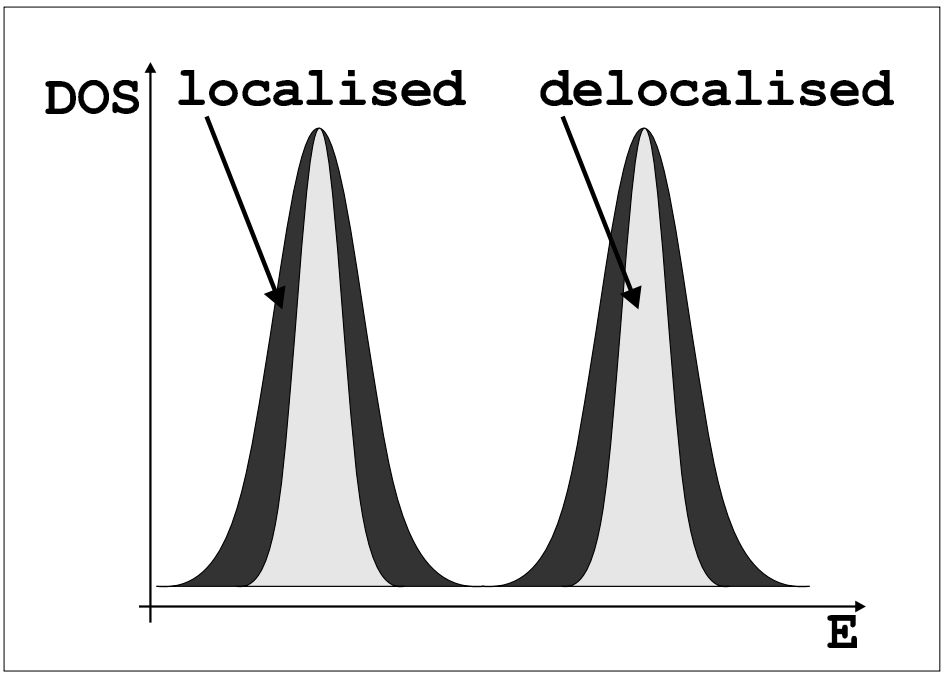

Figure 1.10: *Localised and extended states in a broadened Landau level.*

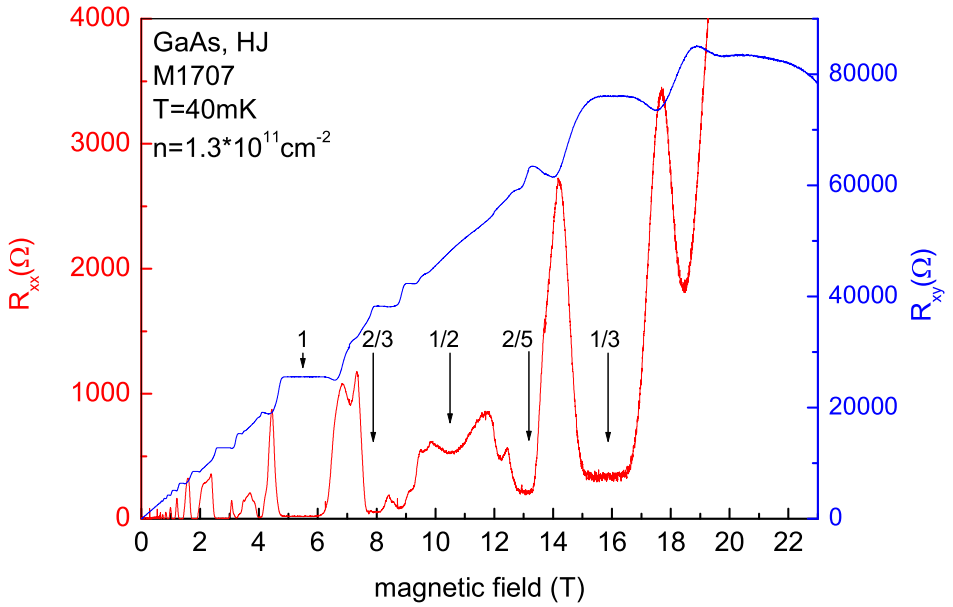

Figure 1.11: *Example of the fractional quantum Hall effect visible in R_{xx} and R_{xy} in the M1707 heterojunction sample. A few main fractions are marked with arrows. Other less visible fractions below $\nu = 1$ are $\nu = {}^3/_5$ and $\nu = {}^3/_7$. The effects of bad contact geometry and/or parallel conduction channel slightly deform the R_{xx} and R_{xy} traces.*

- The effects are sensitive to disorder, as low mobility samples do not show FQHE — on the other hand, the disorder is essential for the existence of the quantum Hall effects as the plateaus' width is determined by the disorder. In a perfect "disorder free" sample the effects would probably not be observed as the plateaus would approach zero width.
- They are also sensitive to temperature, having characteristic energies much smaller than, as an example, Zeeman ($0.25meV = 2.9K$) and cyclotron gaps ($17.28meV = 200K$) at 10T. Numerical values are for GaAs.
- Usually the higher the denominator the weaker is the observed structure — as it has smaller energy gaps.
- Higher magnetic fields facilitate the observation of the FQHE.

The resemblance to the integer effect is remarkable but the fractional quantum Hall effect is a many–body effect due to electron correlations. The electrons in partially filled Landau levels have empty states at their disposition to minimise their energy by rearranging their positions. Earlier [10, 11] many–body explanations that suggested a Wigner crystallisation did not

explain the singularity at $\nu = {}^1\!/_3$. (It seems that the long range ordering of the Wigner crystal is possible at $\nu \leq {}^1\!/_6$ [12, 13].

The early theory of FQHE proposed by Laughlin [14] in 1983 based on the introduction of a new state of the 2DEG namely the *(Laughlin) incompressible liquid state* is now widely accepted. A complementary, appealing approach of *composite fermions* theory by Jain [15] is in agreement with many experiments but still its detailed justification is under discussion. The two theories will be presented briefly.

Laughlin wavefunction

In the description of the FQHE by Laughlin [14] the exact eigenstates of the 2DEG in an odd m, $\nu = {}^1\!/_m$ state are described by the many–electron wave function:

$$\psi_m \quad = \quad \prod_{i<j}(z_i - z_j)^m \prod_k exp(-|z_k|^2/4l_B^2) \tag{1.21}$$

where $z = x + iy$ is the position of the jth electron.

The most striking consequence of the incompressible liquid state described by Eq. (1.21) is the appearance of a *fractional charge*. The incompressibility and the fractionally charged elementary excitations are two concepts that form the core of present understanding of the fractional quantum Hall effect.

With the observation of higher denominator fractions than $\nu = {}^1\!/_3$ a sort of a hierarchy has been observed. It has been recognised that the values at which the fractional effects are observed are lined in a series of fractions. The hierarchy has been explained as the formation of a different type of quasi–particles that are typical for a given fraction when moving from one fractional filling factor to another.

Dispersion of fractionally charged excitations

A schematic energy dispersion of an excitation in the fractional quantum Hall state is presented in Figure 1.12. The energy dispersion has a *magnetoroton* [16] minimum at $k \sim {}^1\!/_{l_B}$ due to the symmetry of wavefunction.

Incompressibility

The incompressibility at zero temperature in the absence of disorder is a necessary condition for the occurrence of the quantum Hall effect [17].

The compressibility (K) defined by:

$$K^{-1} \quad = \quad V\frac{\partial^2 E}{\partial^2 V} \tag{1.22}$$

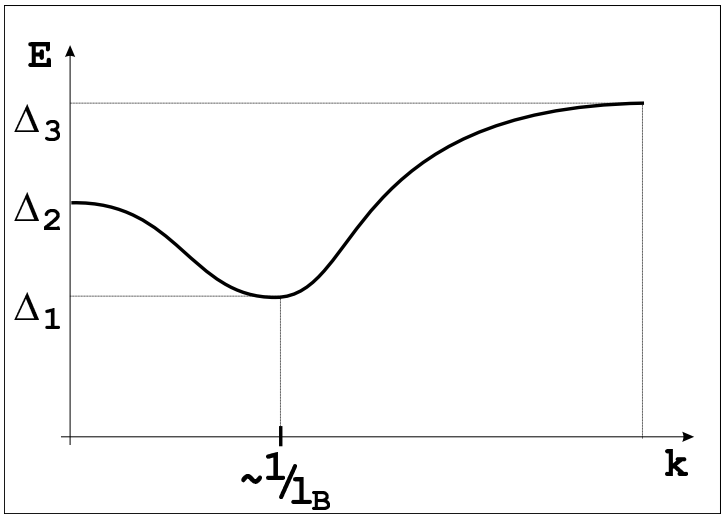

Figure 1.12: *Schematic dispersion of an excitation in $^1/_3$- fractional quantum Hall state. A magnetoroton minimum at $k \sim {}^1/_{l_B}$*

can be connected to the chemical potential: $\mu = \partial E/\partial N = d(n\epsilon(n))/dn$ by:

$$K^{-1} = n^2 \frac{d\mu}{dn} \tag{1.23}$$

When $d\mu/dn = \infty$ that is the chemical potential increases discontinuously with the change of n then $K = 0$ and the system is incompressible. In other words when the system is incompressible the creation of a particle-hole pair costs a finite energy. This in turn implies the existence of an energy gap.

Fractionally charged quasiparticles

A gedanken experiment [17] argues the existence of fractionally charged quasi–particles in the case of an incompressible system in the $\nu = {}^p/_q$ state.

When a flux through an imaginary, infinitely thin solenoid at the origin is changed from 0 to $\Phi_0 = hc/e$ the system is back in the initial eigenstate.

However, we can show that this state has charge eq/p added or removed from an area surrounding the axis of the solenoid. According to the Faraday induction law the time dependent flux gives rise to an azimuthal electric field around the solenoid:

$$E_\phi = \frac{1}{c}\frac{d\phi}{dt}\frac{1}{2\pi R} \tag{1.24}$$

At the incompressible state at filling factor ν the conductivity $\sigma_{xy} = \nu e^2/h$. It follows that, if we look along a ring far enough from the origin, the azimuthal electric field gives rise to a radial current:

$$j_r = \nu \frac{e^2}{h} \frac{1}{c} \frac{d\phi}{dt} \frac{1}{2\pi R} \tag{1.25}$$

and the total *fractional* change in the charge inside the ring — localised within the microscopic length scale is:

$$Q = 2\pi R \int j_r dt = \nu \frac{e^2}{h} \frac{1}{c} \frac{hc}{e} = \nu e \tag{1.26}$$

The concept of fractionally charged particles has been confirmed in measurements of *shot noise* by Saminadayar et al. [18] and Griffiths et al. [19].

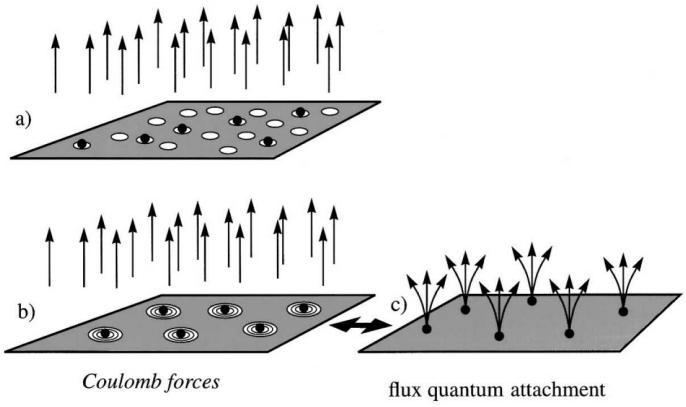

Figure 1.13: *Schematic picture for the $\nu = {}^1/_3$ fractional quantum Hall state. Electrons marked as dots, vortices as discs, magnetic flux quanta as arrows. a) One vortex on each electron with ${}^2/_3$ of vortices unattached. b) The e-e repulsion is reduced by placing additional vortices on the electrons. c) Situation b) viewed as composite particles made from electrons and the attached flux quanta. Picture from [20].*

Composite Fermions

The *composite fermion* (CF) theory was conceived basing on the observation that the fractional quantum Hall effect can be viewed as an integer effect of composite particles, and while it is still discussed whether the particles truly exist and the picture is valid, the model proposed by Jain [15, 21] is helpful in understanding the FQHE.

Difficult to interpret, the strongly correlated system of 2D electrons can be presented in a picture of noninteracting (weakly interacting) new particles (Figure 1.13). These particles possess charge, spin and statistics.

The basic characteristics of the composite fermion theory can be summarised as follows[22]:

- The basic particles in the lowest Landau level (LLL) are the composite fermions created from electrons that have captured an *even number* (2p) of vortices.

- The composite fermions are weakly interacting and can be treated by a single particle description as ordinary fermions

- The effective magnetic field that the composite fermions experience is reduced to:

$$B^* = B - 2m\phi_0\rho \tag{1.27}$$

  where 2m is the number of $\phi_0 = hc/e$ flux quanta, ρ is the density of electrons. The values corresponding to CF are usually marked with an asterisk (*) to differentiate from values corresponding to "normal" electrons. From the above equation the effective magnetic field at $\nu = {}^1\!/_2$ for composite fermions is $B^* = 0$

- The existence of hierarchical structure comes from the IQHE of composite fermions. The CF filling factors ν^* are related to ν by:

$$\nu = \frac{|\nu^*|}{2m|\nu^*| \pm 1} \tag{1.28}$$

Since the vortices are attached to CF, the identification of vortices as flux quanta is a useful simplification. It allows to define a new effective magnetic field as the remainder of the external field that is not attached to the CFs.

A more sophisticated theoretical treatment, the Chern-Simons theory, results from rewriting the original (many body) problem in such a way as to obtain the composite fermion description as a mean–field theory. The obtained CF description is later tested for its self-consistence. See references [23, 24, 25, 26] for the description of the theory.

The *effective mass* m^*_{CF} of composite fermions:

$$\hbar\omega_c^{CF} = \frac{\hbar e B^*}{m^*_{CF}} \tag{1.29}$$

has been determined experimentally by the Shubnikov–de Haas oscillations around $\nu = {}^1\!/_2$ by Leadley et al. [27] as well as by optical methods by Kukushkin et al. [28].

The *cyclotron resonance* of composite fermions experiments showed that CFs execute a cyclotron motion when the magnetic field is changed from $B^* = 0$. One of the important ingredients of the composite fermion theory is that the new particles form a spin–polarised Fermi sea system at $B^* = 0$ analogical to the Fermi sea of electrons at $B = 0$.

Local charge of a composite fermion. On may view a composite fermion as being made of an electron and an even number of vortices. Thus, its intrinsic charge is that of an electron $(-e)$. The correlation with other quasi–electrons produces a *correlation hole* around the quasi–electrons. The *local charge* (e^*) defined as the sum of the intrinsic charge and the correlation hole measured relative to the background state gives a fraction of $-e$ at the $\nu = {}^p\!/_{2mp+1}$ state:

$$-e^* = \frac{-e}{2mp+1} \tag{1.30}$$

When an electron is added to the system, $2mp$ quasi–electrons are generated, each having a local charge $-e^*$. A composite fermion quasi–hole in a CF–Landau level has a charge $+e^*$.

Unification of the Laughlin approach and the composite fermion theory leads for example to the interpretation of the $\nu = {}^1\!/_3$ energy gap at $k \to \infty$ as the cyclotron gap of the composite fermions.

Bibliography

[1] *Landolt-Börnstein - Group III Condensed Matter, Optical Properties. Part 1*, vol. 34-C1 (Springer-Verlag GmbH, 2001).

[2] T. Chakraborty and P. Pietiläinen, *The quantum Hall effects*, Solid-State Sciences (Springer-Verlag, Berlin, Heidelberg, 1995), 2nd ed.

[3] J. P. Eisenstein, H. L. Stormer, V. Narayanamurti, A. Y. Cho, A. C. Gossard, and C. W. Tu, Phys. Rev. Lett. **55**, 875 (1985).

[4] E. Gornik, R. Lassnig, G. Strasser, H. L. Störmer, A. C. Gossard, and W. Wiegmann, Phys. Rev. Lett. **54**, 1820 (1985).

[5] T. P. Smith, B. B. Goldberg, P. J. Stiles, and M. Heiblum, Phys. Rev. B **32**, 2696 (1985).

[6] C. Kittel, *Introduction to solid state physics* (Wydawnictwo Naukowe PWN SA, 1999), Polish ed.

[7] S. Studenikin, M. Potemski, A. Sachrajda, M. Hilke, L. N. Pfeiffer, and K. W. West, Phys. Rev. B **71** (2005), accepted and cond-mat/0411338.

[8] K. von Klitzing, G. Dorda, and M. Pepper, Phys. Rev. Lett. **45**, 494 (1980).

[9] D. C. Tsui, H. L. Stormer, and A. C. Gossard, Phys. Rev. Lett. **48**, 1559 (1982).

[10] D. Yoshioka, B. I. Halperin, and P. A. Lee, Physical Review Letters **50**, 1219 (1983).

[11] D. Yoshioka and P. A. Lee, Phys. Rev. B **27**, 4986 (1983).

[12] H. A. Fertig, *Properties of the Electron Solid*, chap. 3, p. 75, in [29] (1997).

[13] H. Buhmann, W. Joss, K. von Klitzing, I. V. Kukushkin, A. S. Plaut, G. Martinez, K. Ploog, and V. B. Timofeev, Phys. Rev. Lett. **66**, 926 (1991).

[14] R. B. Laughlin, Phys. Rev. Lett. **50**, 1395 (1983).

[15] J. K. Jain, Phys. Rev. Lett. **63**, 199 (1989).

[16] S. M. Girvin, A. H. MacDonald, and P. M. Platzman, Phys. Rev. B **33**, 2481 (1986).

[17] A. H. MacDonald, *Introduction to the physics of the quantum Hall regime*, cond-mat/9410047, Indiana University, Bloomington, IN 47405, USA (1994).

[18] L. Saminadayar, D. C. Glattli, Y. Jin, and B. Etienne, Phys. Rev. Lett. **79**, 2526 (1997).

[19] T. G. Griffiths, E. Comforti, M. Heiblum, A. Stern, and V. Umansky, Physical Review Letters **85**, 3918 (2000).

[20] H. Stormer, Rev. Mod. Phys. **71**, 875 (1999).

[21] J. K. Jain, Phys. Rev. B **41**, 7653 (1990).

[22] J. K. Jain and R. K. Kamilla, *Composite fermions: Particles of the lowest Landau level*, chapter 1, p. 1, in [25] (1998).

[23] A. Lopez and E. Fradkin, Phys. Rev. B **44**, 5246 (1991).

[24] B. I. Halperin, P. A. Lee, and N. Read, Phys. Rev. B. **47**, 7312 (1993).

[25] O. Heinonen, ed., *Composite Fermions* (World Scientific Publishing, Singapore, 1998).

[26] B. I. Halperin, *Fermion Chern-Simons theory and the unquantised quantum Hall effect*, chap. 6, p. 225, in [29] (1997).

[27] D. R. Leadley, R. J. Nicholas, C. T. Foxon, and J. J. Harris, Phys. Rev. Lett **72**, 1906 (1994).

[28] I. V. Kukushkin, J. H. Smet, K. von Klitzing, and W. Wegscheider, Nature **415**, 409 (2002).

[29] S. Das Sarma and A. Pinczuk, eds., *Perspectives in quantum Hall effects* (John Wiley & Sons, Inc., New York, 1997).

Chapter 2

Experimental techniques

Les techniques expérimentales utilisées pour les mesures de photoluminescence, diffusion inélastique de la lumière, transport et absorption des micro-ondes, sous champs magnétiques, sont détailles dans ce chapitre. Les champs magnétiques ont été produits par une bobine supraconductrice de 14T essentiellement pour des mesures de caractérisation aux températures de l'hélium liquide (4.2K - 1.7K). Les champs plus intenses, jusqu'à 28T, ont été produits par les aimants résistifs. Les expériences à très basses températures au dessous de 1K ont été faites dans un réfrigérateur à dilution. Principalement toutes les expériences optiques effectuées utilisent un laser argon (L=514.5nm) pour l'excitation au-dessus de l'énergie de la barrière, ou un laser Ti : Saphir de longueur d'onde ajustable pour l'excitation résonante. La détection de la lumière émise a été faite par un spectromètre optique. Différents systèmes de mesures sont réalisés au bout des fibres optiques utilisées pour la transmission de la lumière et ont été adapté dans un diamètre d'environ 33mm pour un cryostat à hélium liquide et 22mm pour le réfrigérateur à dilution. Le système de mesure de la photoluminescence n'a qu'une fibre optique et permet d'effectuer les mesures de la lumière polarisée circulairement grâce à un polarisateur linéaire et une lame quart d'onde. Les mesures de la diffusion inélastique de la lumière ont été fait avec une géométrie quasi Faraday. Un arrangement de deux fibres pour les mesures de la diffusion inélastique de la lumière permet de minimisation de la détection de la lumière laser diffusée. Un système des mesures simultanées de transport et de luminescence est présenté ainsi que des systèmes de mesure d'absorption des micro-ondes dans une cavité du spectromètre ERP à fréquence ajustable et de détection optique de la résonance cyclotron.

Several experimental techniques have been used to determine the properties of the studied 2D electron systems. The optical measurements included photoluminescence (PL), photoluminescence excitation (PLE), inelastic light scattering (Raman) and Fourier spectroscopy. Luminescence

studies simultaneous with transport measurements were accomplished on the NTT-A quantum well and the M1707 heterojunction. The influence of microwave irradiation on transport properties (MIROs) and on luminescence (ODCR) has also been studied. Those various experimental methods need different experimental setups. The following sections describe the experimental techniques employed during the study.

All the experiments were performed in a magnetic field perpendicular to the 2DEG plane.

The low and moderate field experiments were performed using an Oxford superconducting coil magnet with a maximum achievable magnetic field of 14T. The coil has a 50mm warm bore inside which a liquid helium (LH2) cryostat was inserted. The experiments were performed in a temperature range of $4.2K - 1.7K$.

Higher fields were achieved by one of the resistive magnets in the Laboratory. The maximum magnetic fields produced by the 10MW and 20MW resistive magnets is 23T and 28T, respectively. Inside the 50mm bore of the magnets a liquid helium cryostat was inserted for the experiments performed at helium temperatures ($4.2K - 1.7K$).

The lowest temperature measurements (below $1K$) down to the base bath temperature $T \approx 50mK$ were performed in the dilution fridge installed in place of a LH2 cryostat in a resistive magnet site. An optical insert had to be prepared to allow the photoluminescence and light scattering experiments in the dilution refrigerator.

Common characteristic

The optical setup consisted of a excitation source and a spectrometer. The light was transmitted by optical fibres to and from the sample placed inside a cryostat.

The excitation part of the optical setup was common for all measurements. Above bandgap excitation was done by a continuous–wave Ar^+ laser. The emission line $\lambda_L = 514.5$nm was selected by an interference filter placed in the laser beam. When non resonant excitation was used a low–pass filter was placed at the entrance to the spectrometer to avoid stray light entering the spectrometer.

For resonant excitation either a low–power 670nm solid state laser diode was used or a continuous–wave tunable wavelength Ti::sapphire laser. Specifically, the diode was employed for low–power excitation when simultaneous transport and photoluminescence experiments were done. The Ti:Sapphire laser was used for PL, PLE and Raman measurements.

A different technique had to be used for Raman scattering experiments (see below). The collected emission light was analysed in either a single–grating (1m long, available gratings: 1800 and 3600 lines/mm) or a double-grating (2m long, available gratings: 300 and 1800 lines/mm) optical spec-

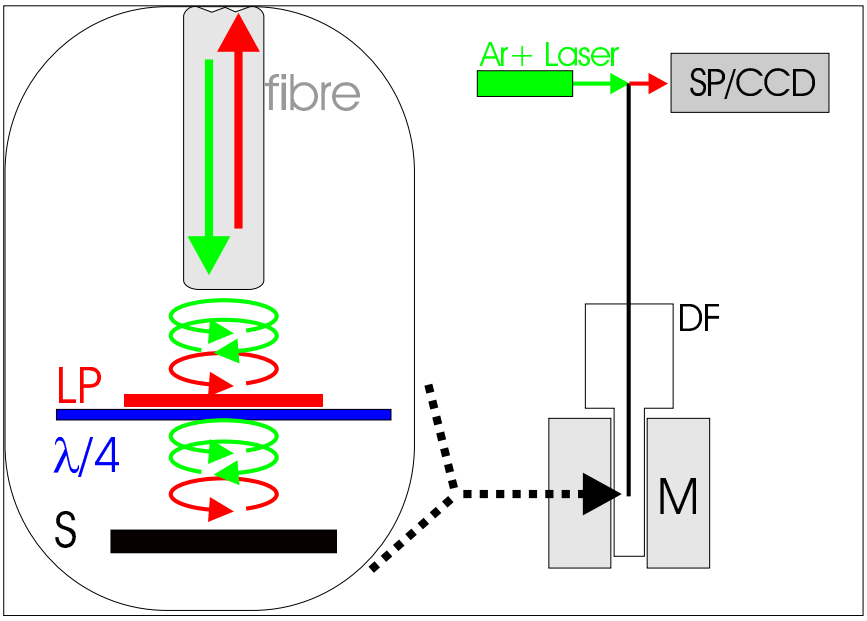

Figure 2.1: *One fibre setup for circularly polarised photoluminescence measurements. The laser light reaching the sample from the fibre is mainly unpolarised. The polarisation of the detected light can be selected by a circular polariser.*

trometer. Both spectrometers were equipped with a 1024x512 CCD camera. The double–grating spectrometer offers a better resolution at the cost of reduced luminosity.

A 1800 lines/mm grating was used in the single–grating spectrometer in the 800nm wavelength range and the available resolution was $0.02nm$ per pixel in a $20nm$ window.

Two sets of gratings of 300 and 1800 lines/mm for the double–grating spectrometer allow the measurements in the wavelength range of interest. The high density grating allowed a resolution of $0.005nm$ per pixel in a $2.5nm$ window while the 300lines/mm grating resolution was $0.05nm$ in a $25nm$ window.

The most important part of the experimental setup is in the vicinity of the measured sample connected by optical fibres to a laser and a spectrometer. The 50mm magnet bore had to accommodate the cryostat and the sample holder so the effective diameter available for the experimental setup was $\sim 33mm$ in a LH2 cryostat and $\sim 22mm$ in the dilution refrigerator. The following section will briefly describe the experimental setups used for different measurements.

2.1 Photoluminescence

A thick $600\mu m$ optical fibre was used to transmit both the exciting beam and the photoluminescence light from the sample in the dilution refrigerator (Figure 2.1). A circular polariser consisting of a linear polariser and a quarter–wave plate was placed between the fibre and the sample. The polariser and the quarter–wave plate have been calibrated for the wavelength range around 800nm (the emission of GaAs). Thus, the sample was excited by mostly unpolarised laser light (green) as the optical fibre did not preserve polarisation. On the other hand, only one circular polarisation of the emitted light was allowed to pass through from the sample into the optical fibre.

To detect the emission in the opposite polarisation the magnetic field direction had to be inverted. The emitted light was analysed by the spectrometer equipped with a CCD camera.

When the emission intensity was expected to be very low e.g. when very low laser intensities were planned to be used the photoluminescence was measured without light polarisation. The usual gain in the detection sensitivity of the emitted light was about 10 times.

All experiments performed in the dilution refrigerator were performed using sufficiently low excitation power to avoid heating of the sample. The maximum power where no change in the measured bath temperature was observed at static magnetic field was less than $1mW$ at base temperature.

2.2 Inelastic light scattering

The inelastic light scattering setup differs from the PL setup by the use of two separate optical fibres for excitation and detection. The optical fibres usually used have a diameter of $200\mu m$. When the excitation energy is similar to the emission energy one can not use a low–pass filter in front of the spectrometer to eliminate the laser light. To minimise the intensity of the laser light entering the spectrometer one has to carefully arrange the two fibres in the proximity of the sample.

In the geometry presented on Figure 2.2 most of the laser light is reflected from the sample surface away from the collecting fibre. The only laser light that can enter the fibre is the one scattered from the surface imperfections. A fixed position of the optical fibres does not allow k–vector dependence measurements. The presented geometry is *almost* a Faraday configuration as the magnetic field (upwards on the picture) is not completely parallel to the k-vector of the incident light. Nevertheless, due to the large value of the GaAs refraction coefficient ($n = 3.3$) the incident light enters the sample almost parallel to the magnetic field direction.

A good fibre arrangement with a good sample surface sample can result

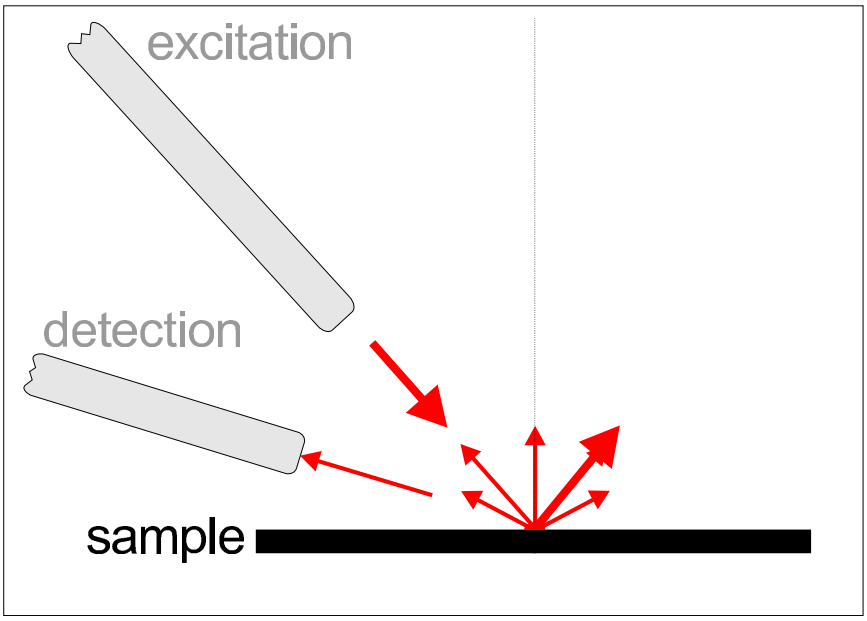

Figure 2.2: *Geometry of a two-fibre system to minimise the gathered laser light. Reflected laser light is rejected from the system.*

in a detection system where the collected laser intensity is comparable to the Raman scattering signal.

2.3 Transport

Every sample studied in this work had at least one corresponding piece with contacts for transport measurements.

In case of the NTT samples it has been found that it was basically impossible to measure transport on samples illuminated with an Ar^+ laser even if unilluminated samples did not pose any problems. Even a short illumination with a 514.5nm laser resulted in a parallel conductance that rendered the measurements impossible. The sample had to be warmed up in order to measure its resistivity.

Thus, very low power, below the barrier excitation by a solid state lasing diode with emission wavelength $\lambda_L = 670nm$ has been used. Such illumination also induced changes in the transport properties but in much longer timescales and allowed to reach a stable state with good transport properties that corresponded to optically detected parameters.

A single optical fibre was placed close to the sample to minimise the illumination of the sample contacts but as far as possible to guarantee a uniform excitation power (Figure 2.3). The presence of the electrical contacts did

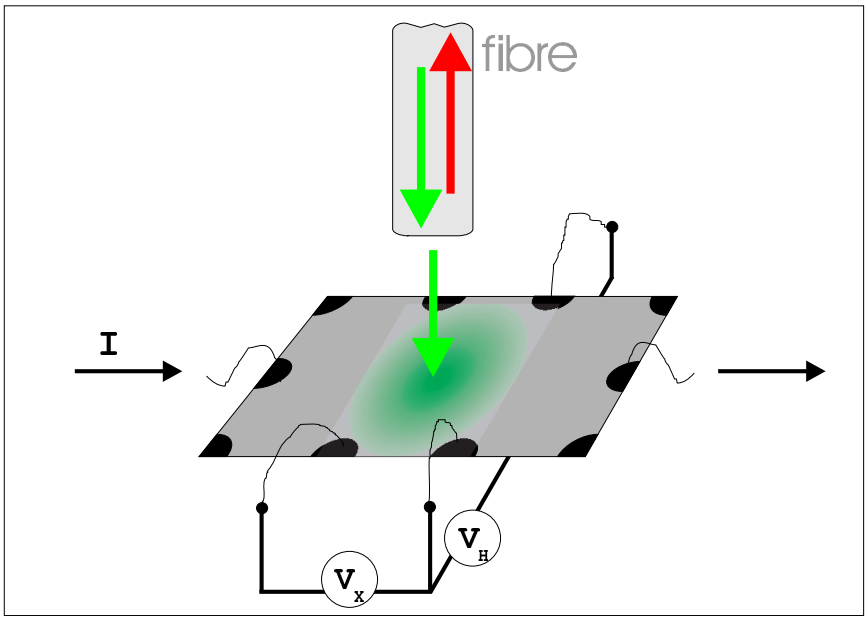

Figure 2.3: *Luminescence and transport, simultaneously. The excitation wavelength used in measurements is* 670*nm.*

not allow easy use of an optical polariser.

2.4 Microwave absorption

The direct microwave absorption experiments were performed in a home–made EPR spectrometer [1, 2]. The spectrometer allows measurements in the microwave frequency range of 40-60 GHz. The maximum power is 5mW .

The critical part of the spectrometer is the multi mode cavity. The cavity is tuned to the microwave frequency by changing the distance between a moving plunger and the top wall of the cavity. The geometry of the magnetic and electrical microwave fields of the main mode are presented in Figure 2.4.

A thin fibre was put through the plunger, which allowed measurements of photoluminescence or light irradiation effects on microwave absorption.

2.5 Optically detected cyclotron resonance

The characteristics of the microwave sources used in the ODCR measurements are presented in Table 2.1.

The system to detect changes due to microwave irradiation in magneto – photoluminescence is a slightly modified PL setup (Figure 2.5). With-

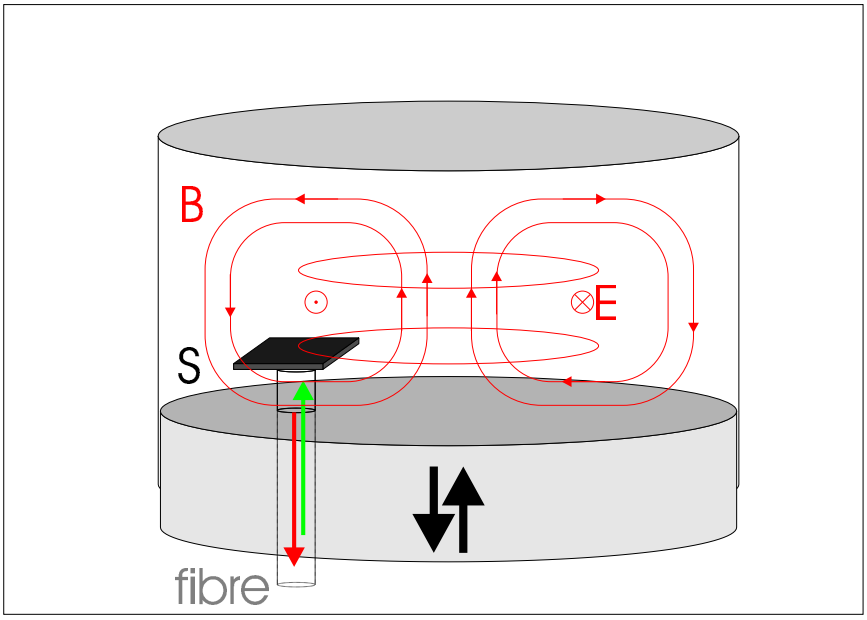

Figure 2.4: *Cavity of a tunable EPR spectrometer. Frequency range is 40-60GHz. For a CR measurement the sample is moved away from the cavity wall into the electric microwave field. An optical fibre allows for an optical excitation or PL measurements. The system is tuned to the microwave frequency by changing the height of the cavity.*

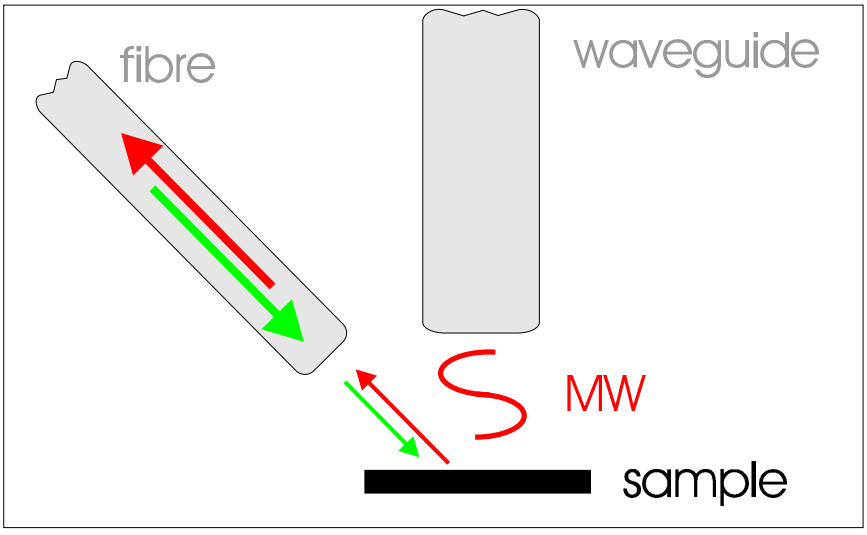

Figure 2.5: *Setup for optical detection of cyclotron resonance. One fibre serves to excite and detect the photoluminescence. Microwaves are transmitted to the sample by an oversized waveguide.*

source	range (GHz)	maximal power (mW)
EPR spectrometer	$40 - 60$	5
Gunn diode	95 ± 1	50
Backward wave oscillator (BWO)	$77.35 - 119.5$	50
BWO with doubler	$154.7 - 239$	5

Table 2.1: *Microwave sources used in the ODCR measurements. Characteristic frequency ranges and maximum powers are indicated.*

out light polarisation the optical part consists only of a single fibre. The modification introduces a microwave oversized waveguide to allow sample irradiation. The use of a long oversized waveguide from the source to the sample inside the LH2 cryostat produces several experimental problems. The alignment of waveguide elements and presence of any edges might result in microwave scattering and lowering of the microwave irradiation power. A too high quality waveguide might result in superfluous cavity which will generate standing microwave waves that will disturb the experiment.

A carbon resistor can be mounted in the proximity of the sample and a measurements of absorbed microwave power can be done.

Bibliography

[1] M. Seck, Ph.D. thesis, Grenoble High Field Laboratory, Universität Konstanzt, Grenoble High Field Laboratory, 38042 Grenoble, France (1997).

[2] M. Seck and P. Wyder, Review of Scientific Instruments **69**, 1817 (1998).

Chapter 3

Investigated systems

Les propriétés des systèmes étudiés sont présentées dans ce chapitre suivies par des calculations auto - cohérentes des profils de bandes énergétiques des puits quantiques.

The presented studies were performed on three quantum well samples and two heterojunction samples. All samples are GaAs/AlGaAs structures and have a high mobility two–dimensional electron gas.

3.1 NTT quantum wells

The quantum well samples were grown at the NTT Basic Research Laboratories in Atsugi, Japan by the MBE method. Figure 3.1 presents the structure of the sample with $d = 20nm$ quantum well (NTT-A). All samples have exactly the same structure and differ only by the quantum well widths.

The high density 2DEG is achieved in the structures by the modulation doping technique [1]. In this case Si dopant atoms are added in the AlGaAs layer. The closest Si δ–doping layer is $75nm$ away from the 2DEG in the NTT structures. The spatial separation minimises the influence of the donor impurities on the 2DEG.

Name	width(nm)	dark		illuminated	
		$\mu\ (cm^2/Vs)$	$n_e\ (cm^{-2})$	$\mu\ (cm^2/Vs)$	$n_e\ (cm^{-2})$
NTT-A	20	$\sim 2.5 \cdot 10^6$	$\sim 1 \cdot 10^{11}$	$\sim 5.5 \cdot 10^6$	$\sim 2 \cdot 10^{11}$
NTT-B	10	$\sim 6 \cdot 10^5$	$0.92 \cdot 10^{11}$	$\sim 1 \cdot 10^6$	$2.15 \cdot 10^{11}$
NTT-C	50	$\sim 1.4 \cdot 10^6$	$0.95 \cdot 10^{11}$	$\sim 4 \cdot 10^6$	$2.29 \cdot 10^{11}$

Table 3.1: *Nominal parameters of the 'as grown' NTT quantum well samples. Mobility μ and 2D electron concentration n_e, dark and after illumination. Neither the illumination duration, wavelength nor the intensity are known.*

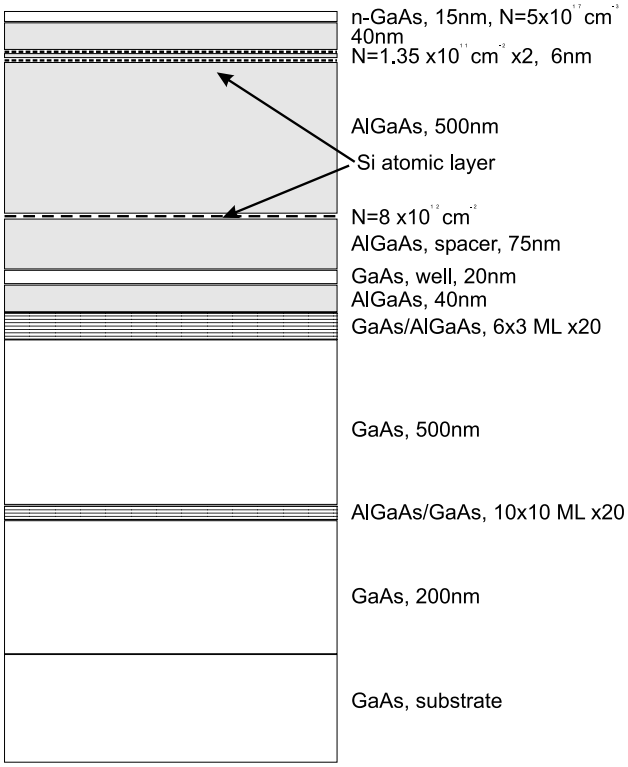

Figure 3.1: *The NTT-A (20nm QW) sample structure provided by the NTT. Other NTT samples differ by quantum well width only.*

The nominal parameters of the NTT samples are collected in Table 3.1. The 2D electron concentration after illumination corresponds to the values determined by PL experiments (see Table 4.1 on page 53). The change of n_e due to illumination is discussed below.

3.2 Bell heterojunction

A heterojunction sample with a very high mobility 2D electron gas was the subject of measurements of the effects of microwave irradiation on the sample resistance. The sample was kindly supplied to us by the Bell Laboratories, USA.

The 2DEG is formed in a triangular quantum well at the interface of a Si-modulation doped 100 $GaAs/Al_xGa_{1-x}As$ heterostructure with x=0.32. The undoped spacer was 800$\mathring{A}$ while the 2DEG was 1900$\mathring{A}$ below the surface.

name	μ (cm^2/Vs)	n_e (cm^{-2})
Bell	$10 \cdot 10^6$	$2 \cdot 10^{11}$

Table 3.2: *Parameters of the Bell heterojunction sample after brief illumination by a red LED at 2K.*

3.3 M1707 heterojunction

A GaAs/AlGaAs heterojunction sample was grown at the Institute for Microstructural Sciences (IMS) laboratories of the Canadian NRC in Ottawa. With a lower 2D electron concentration in the sample the filling factor $\nu = {}^1\!/_3$ was accessible in 10MW resistive magnets (below 23T).

name	μ (cm^2/Vs)	n_e (cm^{-2})
M1707, dark	$2 - 5 \cdot 10^6$	$1.3 \cdot 10^{11}$
M1707	$2 - 5 \cdot 10^6$	$\sim 2 \cdot 10^{11}$

Table 3.3: *Parameters of the dark and illuminated M1707 heterojunction sample.*

3.4 Structure calculation

Given the growth parameters of the NTT structures (presented on Fig. 3.1) it is possible to calculate the energy band positions and the carrier concentration. To simulate the structures a freely available computer program

1DPoisson written by Greg Snider [2] was used. The program allows to self–consistently solve Poisson and Schrödinger equations.

Band profiles. Subband energies

The calculated conduction band energies for the three NTT samples are presented in Figure 3.2. Three (two in the case of $10nm$ QW) lowest electron subbands are also presented. The energy bands were calculated by self–consistently solving Poisson and Schrödinger equations. Then the subband energies were calculated by solving the Schrödinger equation based on the results of the previous calculations.

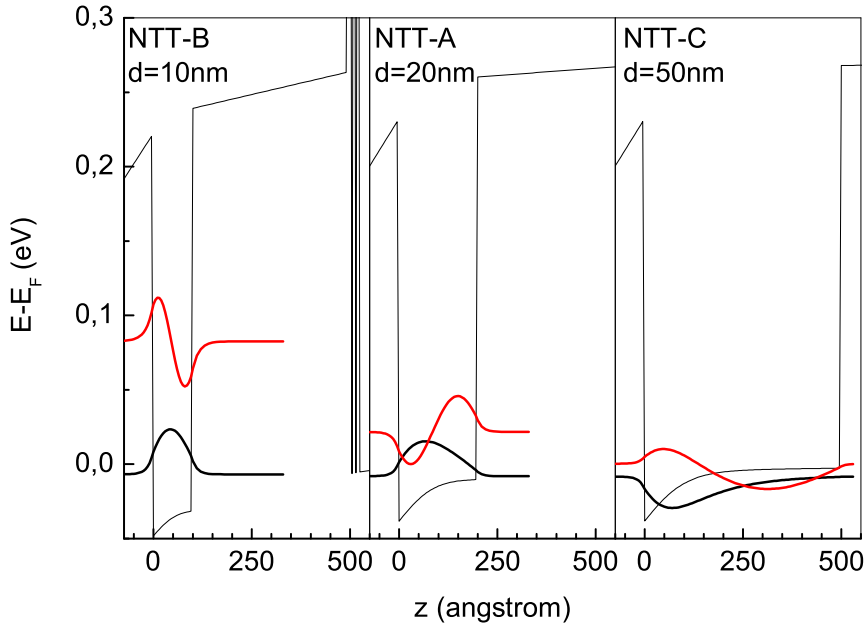

Figure 3.2: *Calculated conduction band profile and first three electron subband wavefunctions. Well widths correspond to samples NTT-B (10nm), NTT-A (20nm), NTT-C (50nm), respectively.*

		Electron subband energy (meV)	
sample	width (nm)	1^{st} subband	2^{nd} subband
NTT-A	20	-8.1	21.7
NTT-B	10	-6.8	82.5
NTT-C	50	-8.3	0.3

Table 3.4: *Calculated conduction band subband energies.* E_f*=0meV.*

		Heavy hole subband energy (eV)	
sample	width (nm)	1^{st} subband	2^{nd} subband
NTT-A	20	-1.5235	-1.5320
NTT-B	10	-1.5498	-1.5679
NTT-C	50	-1.5120	-1.5139

Table 3.5: *Calculated valence band heavy hole subband energies.* E_f*=0meV.*

		Transition energy (eV)		
sample	width (nm)	E_1H_1	E_1H_2	E_2H_1
NTT-A	20	1.5155	1.5537	1.5452
NTT-B	10	1.5430	1.6504	1.6324
NTT-C	50	1.5036	1.5142	1.5123

Table 3.6: *Calculated transition energies.* $dE = E_x - H_y$

Tables 3.4 and 3.5 contain calculated electron and heavy hole subband energies. The subband energy is the distance from the Fermi energy.

It is possible to compare the calculated transmission energies in Table 3.6 with the PL data for the NTT-C sample as both the first subband ($E_1H_1 = 1.508eV$) and the second subband ($E_2H_1 = 1.516eV$) are visible at $B = 0T$. The absolute calculated value differs from the PL recombination energy by $\sim 4meV$. On the other hand, the energy difference $8meV$ between the levels in the PL spectra agrees with the difference between the calculated transition energies $\sim 8meV$.

To compare the subband positions in the NTT-A sample one can analyse the magneto–reflectance data presented in Figure 3.3. The arrow marks the possible signal from the second subband. Its energy position is $E_2 = 1.548eV$ and differs by $\sim 32meV$ from the 1^{st} subband energy $E_1 = 1.516eV$. This difference corresponds to the calculated subband separation value $\sim 30meV$. The very rich magneto–reflectance spectra contain additional lines that are not yet identified.

Electron concentration

Figure 3.4 presents the calculated conduction and valence band profiles along with the square of the wavefunctions $|\Psi|^2$ of the first electron and the first heavy–hole subbands. The wavefunction overlap is minimal in the case of the 50nm quantum well and nearly complete in the case of the $10nm$ QW. The extension of the wavefunctions in the z direction is relevant as it determines

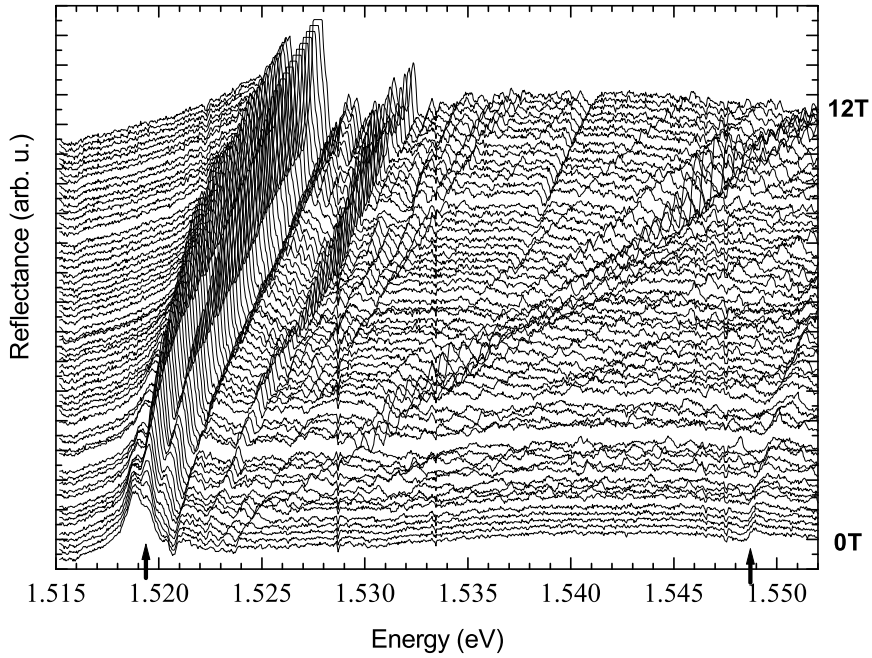

Figure 3.3: *Reflectance data. The 1^{st} and 2^{nd} subband signal marked with arrows. Data from [3]*

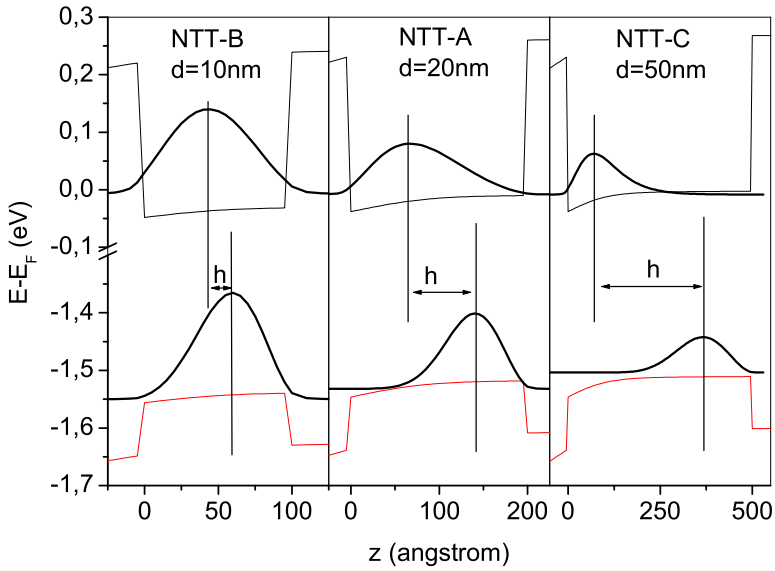

Figure 3.4: *Calculated electron and hole concentration profiles.*

the 2DEG – hole wave functions overlap, which in turn will be an important parameter in the analysis of the PL recombination data in the integer and fractional quantum Hall regime.

sample	width (nm)	$n_e(cm^{-2})$
NTT-A	20	$2.25 \cdot 10^{11}$
NTT-B	10	$1.87 \cdot 10^{11}$
NTT-C	50	$2.34 \cdot 10^{11}$

Table 3.7: *Calculated electron concentrations.*

Table 3.7 contains calculated electron concentrations in the quantum wells that correspond to n_e profiles presented in Figure 3.4. The profiles were calculated as a square of the wave–functions of the occupied energy subbands.

Results show that only the first electron subbands are occupied. The exception is NTT-C, were the 2^{nd} subband has an energy $E_2 = 0.3meV$ above the Fermi energy. The energy corresponds to $T = 3.5K$ ($k_BT = 0.086meV/K$) and its occupancy is determined by temperatures used in experiments.

The calculated values of n_e in samples NTT-B and NTT-C (Table 3.7) differ by the order of $\sim 0.3 \cdot 10^{11}cm^{-2}$, from the electron concentrations estimated from the photoluminescence experiments (Table 4.1, p. 53). Additional simulations were performed where the input parameters describing the structure have been changed, namely the concentration of the dopant at $z = -690\mathring{A}$, to achieve the correct n_e in the quantum wells (Table 3.8).

		$n_e(cm^{-2})$	
sample	width (nm)	$N_d = 0.6 \cdot 10^{12}$	$N_d = 200 \cdot 10^{12}$
NTT-A	20	$2 \cdot 10^{11}$	$2.46 \cdot 10^{11}$
NTT-B	10	$1.64 \cdot 10^{11}$	$2.07 \cdot 10^{11}$
NTT-C	50	$2.12 \cdot 10^{11}$	$2.57 \cdot 10^{11}$

Table 3.8: *Changes of the calculated electron concentrations due to different impurity concentrations:* $N_d = 0.6 \cdot 10^{12}cm^{-2}$ *and* $N_d = 200 \cdot 10^{12}cm^{-2}$.

N_d was adjusted to $0.6 \cdot 10^{12}cm^{-2}$ to correct the calculated concentration in the $50nm$ quantum well. Unfortunately, this new parameter value was still not good for the other quantum wells. Another parameter value $N_d = 200 \cdot 10^{12}cm^{-2}$ corrected the calculated n_e in the NTT-B sample.

The concentration variations were not accompanied by either great energy levels position change or changes in the subband wavefunctions.

Bibliography

[1] R. Dingle, H. L. Stormer, A. C. Gossard, and W. Wiegmann, Appl. Phys. Lett. **33**, 665 (1978).

[2] G. Snider, *1d Poisson* (2001), URL `http://www.nd.edu/$\sim$gsnider/`.

[3] B. Chwalisz, *Photoluminescence of high-mobility electron gas in GaAs/AlGaAs quantum well*, Report, Grenoble High Magnetic Field Laboratory (2003).

Chapter 4

2DEG in a magnetic field: introductory studies

Dans ce chapitre les études préliminaires présentées, constituent une caractérisation avancée des échantillons étudiés. La caractérisation par des mesures de transport, résonance cyclotron et photoluminescence dans le régime de l'effet Hall quantique entier sont faites pour déterminer les propriétés du gaz électronique bidimensionnel (2DEG) comme la masse effective électronique ou la grandeur de l'interaction électron - trou de la bande de valence. Cette connaissance de base des systèmes étudiés est nécessaire pour des études plus avancées de l'effet Hall quantique fractionnaire ou de l'effet d'irradiation des micro-ondes.

Les études des propriétés de transport d'échantillon NTT-A (d=20nm) montrent l'évolution de la concentration d'électrons pendant l'illumination. Les mesures de transport sur l'échantillon non illuminé ne correspondent pas aux mesures optiques ayant une concentration d'électron deux fois plus petite. Pendant les mesures d'évolution temporelle, deux états stationnaires ont été trouvés ; un avec une concentration d'électrons très basse et un autre avec une concentration qui correspond à l'état mesuré par photoluminescence.

La caractérisation d'un 2DEG par les études optiques a été faite dans le régime de l'effet Hall quantique entier et à très basses températures. L'analyse de l'éventail de Landau donne une valeur de masse réduite électronique et de concentration d'électrons. Un concept d'échelle énergétique décalée linéairement a été introduit de façon à mieux présenter les changements d'énergie d'émission.

L'influence de la largeur du puit quantique sur la photoluminescence est discutée par rapport à l'exemple connu du facteur de remplissage $\nu = 1$. Les comportements différents résultent de différentes valeurs d'interaction entre les électrons et le trou. Les trois échantillons NTT représentent trois valeurs différentes du rapport entre l'interaction électron - trou et l'interaction électron - électron. L'émission de l'échantillon NTT-B de puit quantique

10nm est approximativement indépendante du facteur du remplissage, car le trou induit optiquement retient un électron et forme un exciton neutre ou un exciton chargé négativement. Dans les deux cas, les corrélations entre les électrons sont détruites. L'émission des autres puits quantiques réveille un changement d'énergie. L'émission de puit quantique de 20nm montre une augmentation de l'énergie d'émission et l'émission du puit quantique NTT-C de 50nm montre une diminution de cette énergie. Les deux sont dans le régime ou l'interaction entre les électrons et l'interaction électron - trou sont comparables. Dans le 20nm puit quantique l'interaction électron - trou est plus grande et dans le puit quantique de 50nm l'interaction entre les électrons est plus grande. Ces différents régimes seront utilisés pour l'explication des différents comportements dans la région de l'effet Hall quantique fractionnaire.

The results presented in this chapter can be regarded as an advanced characterisation of our samples. The transport characterisation, cyclotron resonance and photoluminescence in the integer filling factor regime have been performed to determine the 2DEG properties such as the emission energy, the carrier concentration, the effective mass or the magnitude of the electron – hole interaction. This basic knowledge of the systems is needed for further studies of the fractional quantum Hall effect or effects of the microwave irradiation.

4.1 Transport properties

The preferred geometry for transport measurements is the Hall bar geometry, which ensures that effects such as those arising from finite size contacts are minimised. In the case of samples for optical measurements the Hall bar is usually an obstacle and the van der Pauw [1] method is used instead. In this geometry four contacts on the corners of a square sample are used. By measuring the resistance between different sets of contacts one can deduce sheet resistivity from the van der Pauw equation. The Hall resistance is measured by letting current flow across the sample and measuring the voltage on the other two contacts.

Samples measured in optical experiments usually do not have contacts on them to allow transport measurements. In case of resonant excitation the lack of a transport lithography structure is very important as the laser light could be scattered and too much stray light might enter into the collecting fibre. For this reason the samples were cleaved into parts beforehand and a second piece of each sample exists that is fitted with contacts for transport measurements.

The observation of the striking optical features (see Chapter 5) needs to be confirmed by transport measurements so it became apparent that a

simultaneous measurement of photoluminescence and transport in the fractional quantum Hall regime is indispensable. Thus, a lot of effort has been put into the measurements of the NTT-A sample, the representative sample for optical measurements. Simultaneous measurements of luminescence and transport were done on a sample with contacts in a van der Pauw geometry.

While the transport measurements of unilluminated NTT samples did not pose unusual problems it has turned out to be very difficult to measure the resistance after illumination.

The results of transport characterisation of heterojunction samples will be now discussed, followed by a brief presentation of the effect of illumination of the NTT-A sample on transport properties.

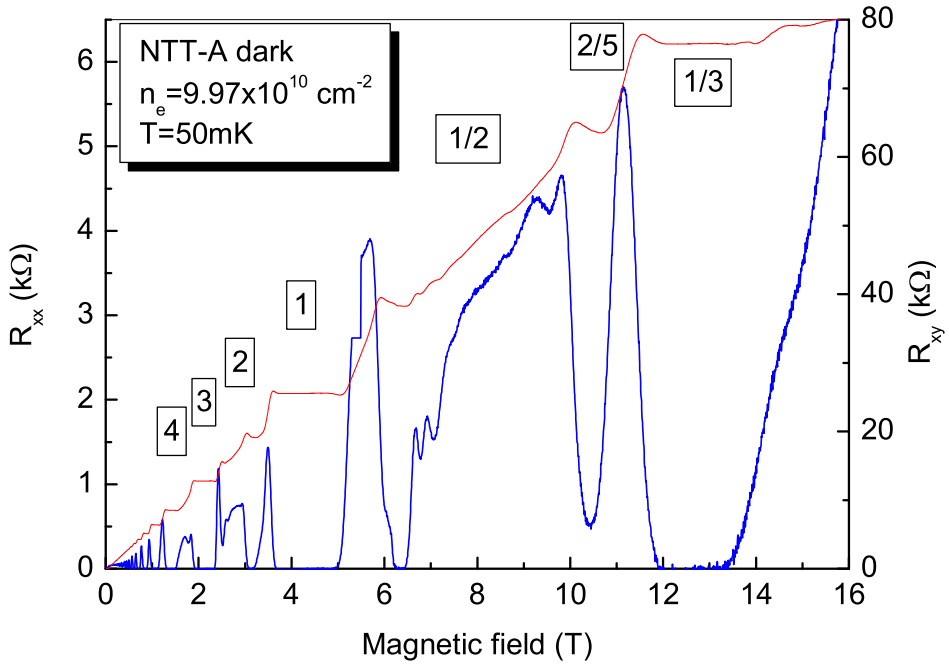

Figure 4.1: *Fractional and integer quantum Hall effect features in the R_{xx} and R_{xy} traces of the unilluminated NTT-A sample.*

4.1.1 Heterostructure "Bell labs"

The "Bell" heterojunction was the only one not measured in the optical interband spectroscopy experiments. It was assigned for the studies of the microwave induced resistance oscillations (MIROs)(see Chapter 6, p. 117).

As most samples, it needed a brief "forming " with light illumination to achieve a stable electron concentration and usual mobility for this sample (see Table 3.2, p. 33, for the final values).

4.1.2 Heterostructure M1707

Figure 1.11, p.13, presents an example of R_{xx} and R_{xy} traces of the unilluminated M1707 sample. Illumination increases the electron concentration to $\sim 2 \cdot 10^{11} cm^{-2}$ while increasing a parallel conductance which results in an increase in the magneto–resistance and worse R_{xx}, R_{xy} traces.

4.1.3 Quantum well NTT-A

Unilluminated

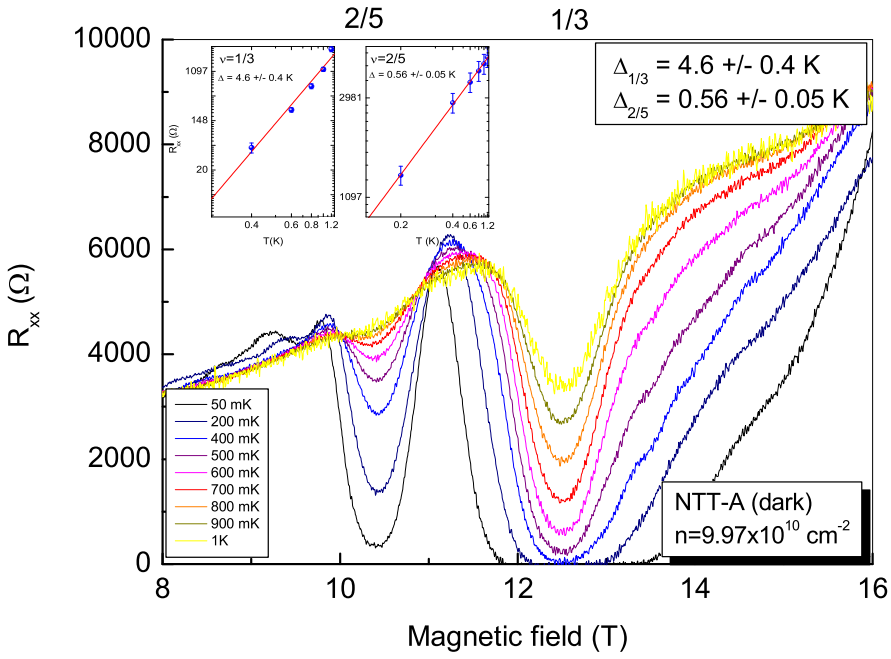

Figure 4.2: *Illustration of the temperature activated character of R_{xx} at $\nu = {}^1/_3$ and $\nu = {}^2/_5$. The obtained corresponding characteristic energy gaps are shown. The sample is the unilluminated NTT-A quantum well. Inset. Arrhenius plots of R_{xx} that were used to determine values of energy gaps at both fractions of filling factor.*

The NTT-A sample was the most studied in transport due to the need of verification of the optical features. Figure 4.1 presents measurements of the unilluminated sample. The electron concentration is $9.97 \cdot 10^{10} cm^{-2}$ i.e. two times lower than usually measured in the magneto–photoluminescence. Clearly the transport measurements "in dark" would not correspond to the optical measurements. Nevertheless, these experiments nicely illustrate the fractional quantum Hall effect and in particular allow us to show the activated character of the $\nu = {}^1/_3$ and $\nu = {}^2/_5$ states and evaluate the corre-

sponding energy gaps. The traces and the determined values of the energy gaps are presented on Figure 4.2 .

Evolution in illumination time

To measure the dependence of the transport properties on illumination the sample was placed in a dilution refrigerator. The evolution of the resistance was followed for several days of constant illumination with a very low power. The $\lambda = 670nm$ illumination had a total power of $\sim 1nW$. A few intermediate state traces of R_{xx} are plotted in Figure 4.3. A dramatic evolution of the resistance traces was observed.

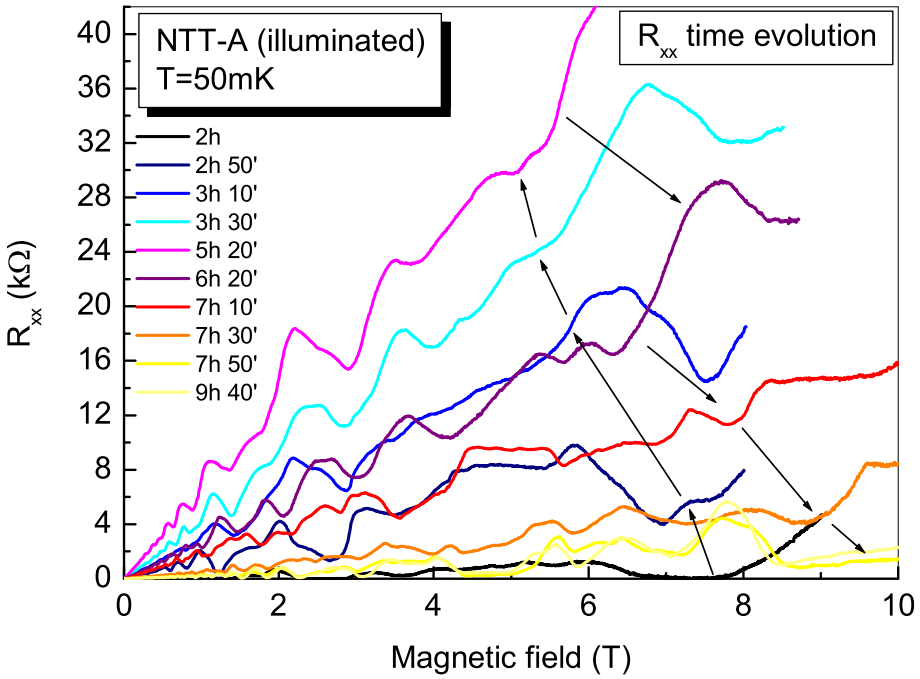

Figure 4.3: *Evolution of the R_{xx} trace in the NTT-A sample with illumination time. Curves correspond to between two hours and 10 hours of illumintion. Arrows mark the sequence in which the R_{xx} trace changes.*

Very low concentration

An intermediate, quasi-stationary state with a very low concentration of carriers was found during studies of the time evolution of the illumination effects. The lowest observed concentration with sufficiently good transport properties is $n_e = 6 \cdot 10^{10} cm^{-2}$. The corresponding transport curves are presented in Figure 4.4. This is a stable state and the transport properties do not change with time when the illumination is switched off.

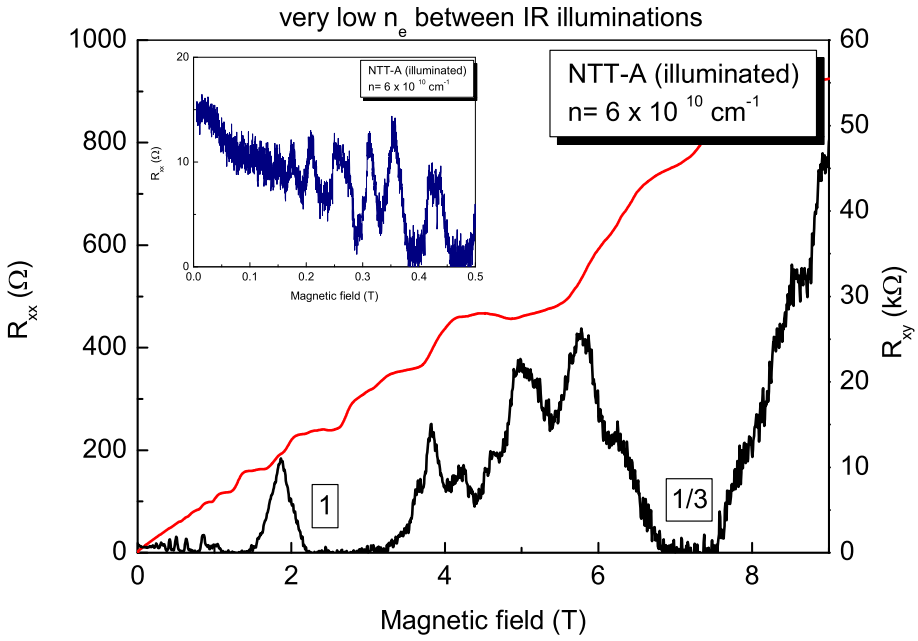

Figure 4.4: *An intermediate state after* $\sim$ 30 *hours of illumination* ($\lambda = 670nm$, $P = 1nW$) *at low temperatures, of very low electron concentration in the NTT-A sample.*

High concentration

A second relatively stable state has been found to be equivalent to the one determined by photoluminescence. The electron concentration $n_e = 2.2 \cdot 10^{11} cm^{-2}$ corresponds to the value found in optical experiments. Figure 4.5 presents transport curves of R_{xx} and R_{xy} of an illuminated NTT-A sample.

The traces shown in Figure 4.5 were relatively stable over a long time, even if the sample was *continuously* illuminated. They present the most reasonable quantum Hall effect curves obtained on these samples even under simultaneous illumination.

The main integer as well as fractional quantum Hall states are well pronounced in these traces. The $\nu = {}^1/_3$ fractional quantum Hall state is particularly well pronounced, with a clear minimum in R_{xx} and almost correct resistance of the R_{xy} plateau.

The evolution of the resistance traces with illumination, we think, are the results of quasi–persistent changes of the carrier concentration with the effect of inhomogeneous concentration playing an important role. A relatively homogeneous concentration can be achieved in the low and high concentration regimes but further illumination leads to the development of a parallel conduction channel.

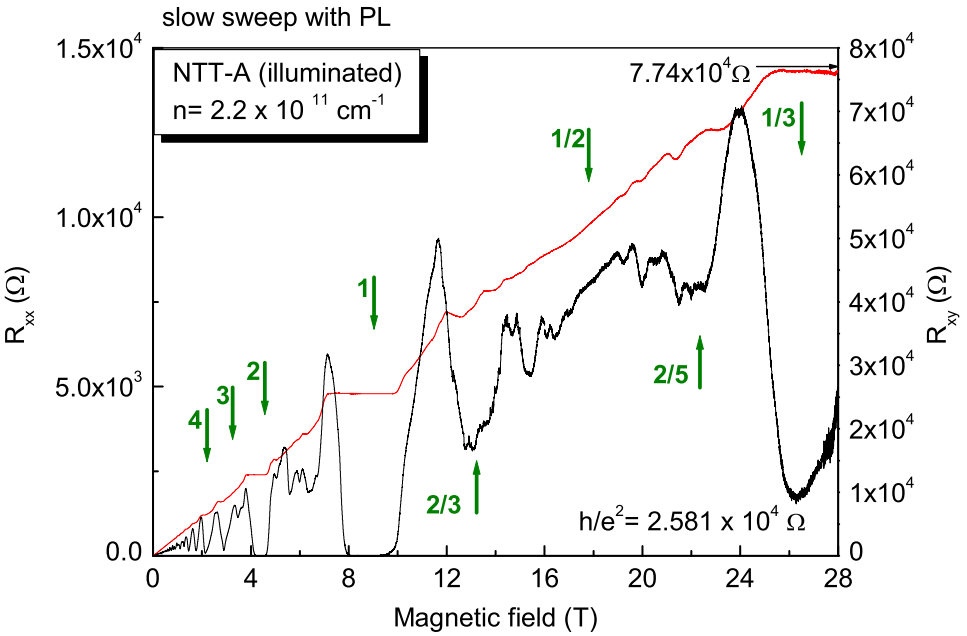

Figure 4.5: *Second relatively stable state of the illuminated NTT-A sample.* $n_e = 2.2 \cdot 10^{11} cm^{-2}$. *Illumination power* $\sim 1nW/mm^2$, $\lambda = 670nm$. *Achieved after further* ~ 8 *hours of illumination.*

The results of simultaneous measurements of photoluminescence in the vicinity of $\nu = {}^1/_3$ will be presented in Section 5.3.5, p. 96.

4.2 Cyclotron resonance

The cyclotron resonance effect occurs in the presence of an external magnetic field when the electromagnetic wave has the same frequency as the circular motion of the electrons. In such a case a resonant absorption occurs. In the 2DEG in quantising magnetic fields the cyclotron resonance can be seen as the transition between adjacent Landau levels in the vicinity of the Fermi level. The measurement of a transmission spectrum returns information about the energy at which the transition takes place. The CR after its first observation on 2D systems in 1976 by Abstreiter et al. [2] in a MOSFET structure has become a standard method in 2DEG characterisation.

The absorption takes place in the far infrared (FIR) region energy region ($10 - 500cm^{-1} = 1.24 - 62meV$). For the GaAs effective electron mass $m^* = 0.067$ the linear cyclotron resonance energy is $\hbar\omega_c = 1.72meV/T$.

The spectra have been measured using a standard Bruker Fourier transform infra–red spectrometer. The usual method is to divide the spectrum taken at a given field value by the zero field spectrum. The procedure results

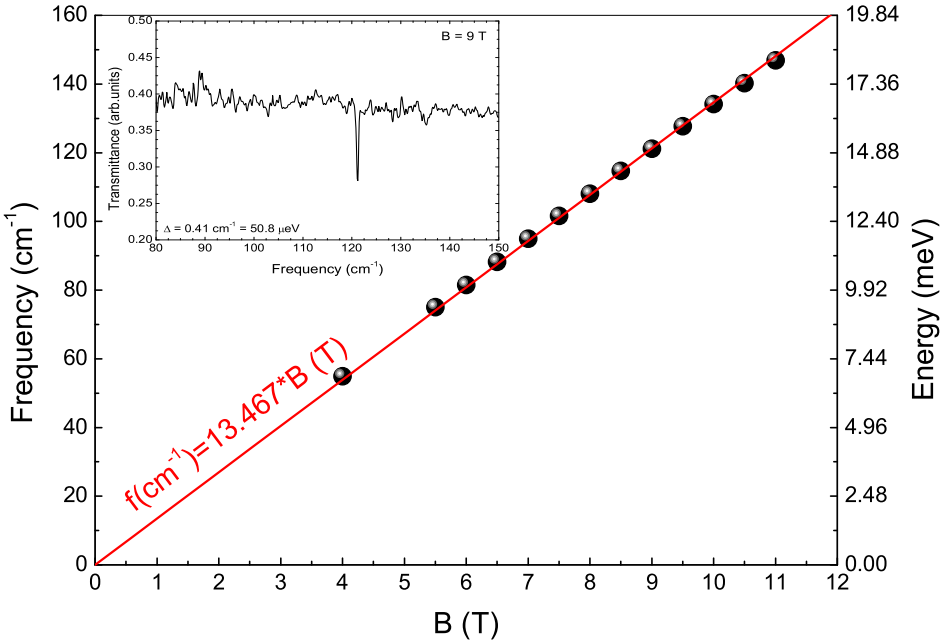

Figure 4.6: *Determination of the electron effective mass from cyclotron resonance measurements. Inset. Normalised transmission spectrum at B=9T of the NTT-A sample. Data from [3].*

in the spectra on which the difference due to the magnetic field is visible while the spectral features not dependent on the magnetic field should disappear. The inset in Figure 4.6 presents a representative normalised spectrum obtained for the NTT-A sample at B=9T. The absorption due to the cyclotron resonance is visible in the inset as a deep peak at around $121 cm^{-1}$ ($1\,meV = 8.0655\,cm^{-1}$). The linear dependence allowed to determine the electron effective mass in the NTT-A sample to be:

$$m_e^{CR} = 0.069 m_0 \tag{4.1}$$

4.3 Interband optics

4.3.1 Simple photoluminescence model

To analyse the PL spectra at zero magnetic field one can use a simple model. The model takes into account the wave–vector conservation law $\delta k = 0$ and a dependence of the recombination intensity for a given energy only on the density of states of occupied states in the conduction band and empty states in the valence band (see schematic view in Figure 4.7.)

The photoluminescence intensity is given by :

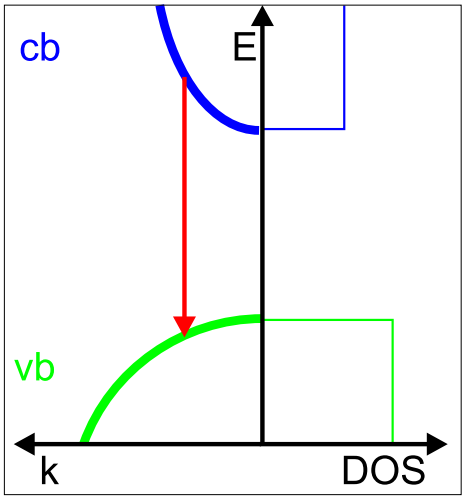

Figure 4.7: *Energy dispersion, density of states and a recombination process schematically presented for a quantum well.*

$$I\big(E(k)\big) \quad \sim \quad \int D_e(k) \cdot D_h(k')\delta(k,k')dk' \tag{4.2}$$

To model more closely a real system one should include the level broadening by a normalised gaussian function:

$$D(E,E') \quad = \quad \frac{1}{\sqrt{2\cdot\pi}\cdot\sigma} \cdot e^{-\frac{(E-E')^2}{2\cdot\sigma^2}} \tag{4.3}$$

$$\tag{4.4}$$

where σ is the broadening parameter.

As $I(E)$ depends on the number of occupied states in the conduction band and empty states in the valence band, it depends on the temperature. The temperature changes the occupancy of energy levels described by the Fermi distribution.

Within this simple model, the low temperature spectrum of a 2DEG rises sharply at the energy E_g^{2D} corresponding to the bandgap of a quantum well and has a high energy cutoff (see Figure 4.9) around

$$E_g^{2D} \quad + \quad E_F\left(1+\frac{m_e}{m_h}\right) \tag{4.5}$$

where E_F is the electron Fermi energy and m_e/m_h is the ratio of the electron to the hole mass.

4.3.2 Zero magnetic field

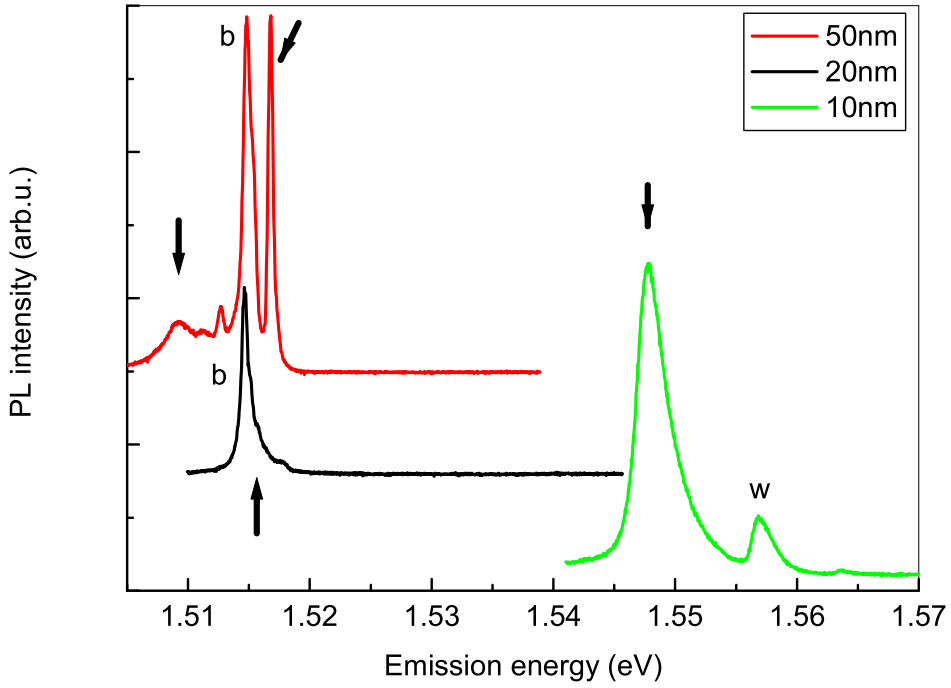

Figure 4.8: *Zero field PL spectra of (respectively from top) 50nm , 20nm, 10nm sample. The 2DEG emission is marked by arrows. Letter 'b' marks the emission from bulk GaAs, letter 'w' marks the emission from an empty quantum well present in all three NTT samples. Bath temperature is 30mK.*

The zero magnetic field photoluminescence spectrum allows to estimate the quality of the sample. Second, for the quantum wells, the photoluminescence spectral shape is the convolution of the distribution function of the 2D electrons and the photo-injected holes. Usually from a zero field spectrum one can estimate the electron concentration n_e and the Fermi energy E_F.

Figure 4.8 presents zero field spectra of the three NTT samples. The photoluminescence signal from the 2DEG is marked by arrows. The PL from the $20nm$ and $50nm$ samples lies in the vicinity of the GaAs bulk emission (b).

The 10nm sample emission is shifted to higher energy and is well separated from the bulk emission. There exists an unidentified empty quantum well (w, $E = 1.557eV$) whose emission overlaps the high energy tail of the 2DEG emission. This empty well exists in all three NTT samples but hampers the analysis of the 10nm PL only, as its emission lies around the expected Fermi energy.

In the case of the $d = 20nm$ sample the zero field emission from the

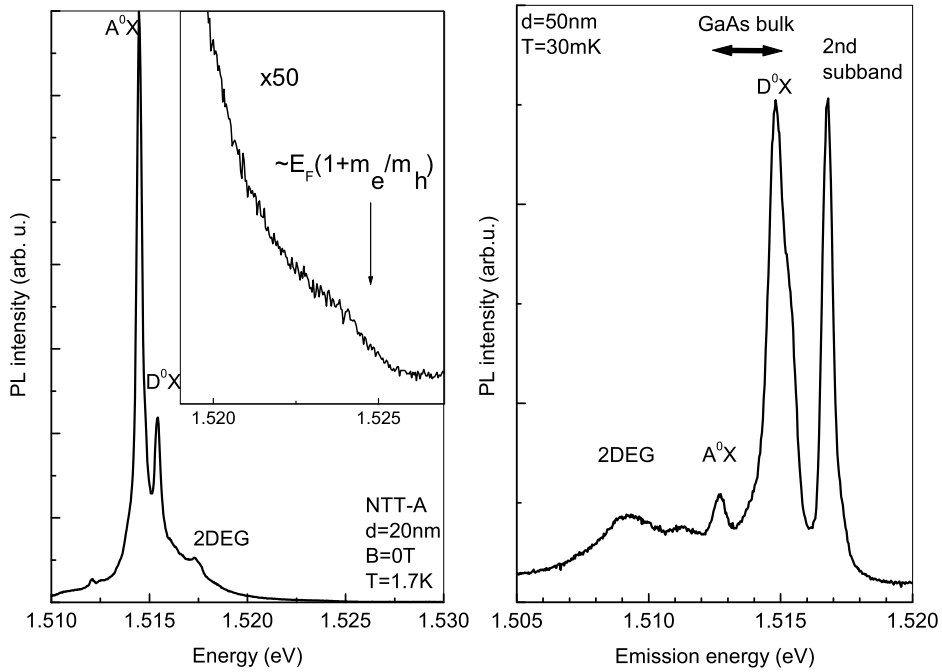

Figure 4.9: *Left. Zero field PL spectrum of the 20nm sample. Inset. The thermal distribution of electron occupied states visible at the Fermi energy. Right. Zero field PL spectra of the 50nm sample. The 2DEG emission is visible on the low energy side of the bulk emission. The following photoluminescence lines have been marked: 2DEG, bulk donor bound exciton, bulk acceptor bound exciton, 2DEG* 2^{nd} *subband*

2DEG lies on the high energy side of bulk excitons. It is the best sample for the magneto – photoluminescence as the different field dependences will allow to separate both lines, and most of Section 5 on the fractional quantum Hall effect will concentrate on experimental results from this sample. At zero field the 2DEG photoluminescence high–energy edge is visible and the Fermi energy may be determined if the low energy PL edge can be guessed correctly (Fig. 4.9, left). From later magneto – optical measurements the Fermi energy is $E_F = 8.95meV$ in the NTT-A sample.

Figure 4.9, right, presents the spectrum of the emission from the $50nm$ quantum well. The highest energy line visible is an emission from the 2^{nd} electronic subband in the quantum well. This emission from the 2^{nd} subband is visible only in the $d = 50nm$ sample. One can deduce the second subband offset to be $8meV$. In higher magnetic field the emission from the bulk GaAs overlaps the 2DEG emission, rendering the analysis of higher–field fractional filling factors impossible.

4.3.3 Magneto–optics in moderate fields

The measurements of the dependence of the photoluminescence on the filling factor are performed by varying the applied external magnetic field while the 2D electron concentration is assumed to be constant. This assumption implies careful control of the excitation power to avoid the effect of carrier depletion [4]. The stability of the 2D electron concentration is later checked against the magnetic field positions of the observed features of integer and fractional filling factor.

Polarisation

The external magnetic field lifts the spin degeneracy of the electron and hole energy levels. The $m_s = \pm 1/2$ electron spin states are split by the Zeeman energy: $Ez = 0.025meV/T$ for $|g^*| = 0.44$. Also, the heavy hole spin level degeneracy is lifted in quantum wells in a magnetic field. Figure 4.10 presents the schematic of the spin splitting for the electron and the $3/2$ heavy hole spin states. Additionally, optically allowed transitions ($\Delta m = \pm 1$) are schematically presented as vertical arrows.

The intensity depends on the occupancy of the corresponding energy levels. At low temperatures, when $kT \ll Ez$, ($kT(1K) = g\mu_B B(1.49T)$), the spin polarisation of the system is reflected in the ratio of the strong σ^- line to the weak σ^+ line.

Figure 4.11 shows magneto–PL spectra for two circular light polarisations σ^- (left) and σ^+ (right). For the presented $20nm$ NTT-A sample the bulk emission is below the 2DEG emission for shown magnetic field values. Spectra at very low fields below $B = 1T$, where the 2DEG relater lines overlap with bulk photoluminescence, were removed.

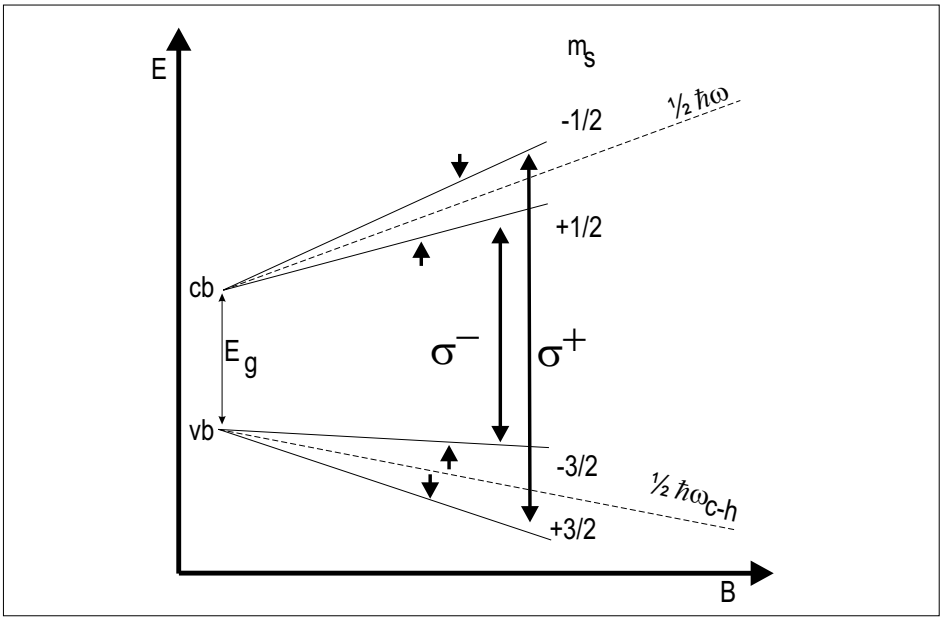

Figure 4.10: *Schematic magnetic field evolution of the conduction band (cb) electron and the valence band (vb) heavy hole energies.The orbital effect is marked by by dashed lines. The Zeeman energy splits each level into two (marked by solid lines). Vertical arrows mark allowed optical transitions for a given polarisation.*

Concentrating on the recombination from the lowest Landau level an obvious higher σ^- than σ^+ overall recombination intensity is observed. Looking closely one can discern a magnetic field range from $B \approx 3T$ to $B \approx 5T$ where σ^+ becomes more intense. This region corresponds roughly to the filling factor range $\nu = 2 \sim 3$ (See Sec. 4.3.6, p. 68 for $\nu = 2$).

Landau level fan chart

The emission from higher Landau levels is visible in the spectra in Figure 4.11. The field dependence of emission energies creates a Landau level fan chart (Fig. 4.12). The fan chart can be used to determine the 2D electron concentration, the reduced effective mass and the Fermi energy.

Electron concentration. The magnetic field where the disappearance of the emission from consecutive Landau levels is observed is deemed to correspond to an integer filling factor. While the exactness of the determination of the field of a single transition is uncertain, the series of transitions can determine the value of n_e quite precisely. This *low field* value is later compared with measurements in the fractional quantum Hall regime. The photoluminescence features in the fractional quantum Hall regime are not

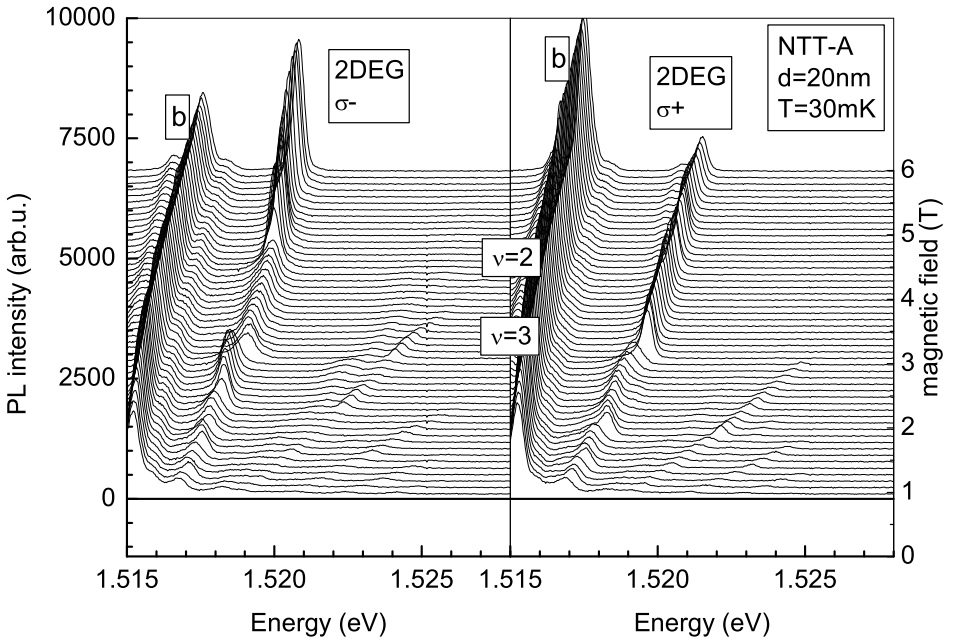

Figure 4.11: *Polarisation dependence of the low–field magneto – photoluminescence spectra of the 20nm quantum well sample. Visible filling factor dependent intensity variations in the $\nu = 3 \sim 2$ region. The spectra between $0 - 1T$ were omitted.*

used to determine n_e. The *a priori* knowledge of the electron concentration from the low field measurements allows to assign observed features to fractional filling factors. The n_e value determined independently from the high field measurements corresponds to the *low field* value, so n_e is determined to be constant. The measured positions of integer and fractional filling factors in optically measured samples are presented in Table 4.1.

Effective mass. The magnetic field dependence of the emission energy yields information on the *reduced effective mass*. According to Figure 4.10 the transition energy depends on both the electron and hole cyclotron energies (temporarily ignoring the Zeeman splitting).

$$E = \hbar\omega_{c-e} + \hbar\omega_{c-h} = \hbar\frac{eB}{c}\left(\frac{1}{m_e} + \frac{1}{m_h}\right) \tag{4.6}$$

Defining the reduced effective mass as:

$$\frac{1}{m_r} = \frac{1}{m_e} + \frac{1}{m_h} \tag{4.7}$$

	magnetic field position B(T)		
ν	NTT-A ($20nm$)	NTT-B ($10nm$)	NTT-C ($50nm$)
5	1.85		1.93
4	2.3	2.2	2.23
3	3.05	2.9	3.00
2	4.6	4.2	4.25
1	9.2	8.5	8.54
2/3	*13.8*		12.90
3/5	*15.3*		14.08
1/2	*18.4*		
3/7	*21.5*		
2/5	*23*		
1/3	*27.6*		
$n_e(cm^{-2})$	$2.22 \cdot 10^{11}$	$2.1 \cdot 10^{11}$	$2.05 \cdot 10^{11}$
$E_f(meV)$	8.95	*7.3*	*7.1*

Table 4.1: *Measured integer and fractional filling factor positions in the magneto – photoluminescence spectra, and corresponding 2D electron concentrations and measured Fermi energies in the NTT samples. Italics in the NTT-A column: The exact values were based on the integer fillings and the luminescence features. Values of E_f for NTT-B and NTT-C are calculated for $m_e^* = 0.069\, m_0$.*

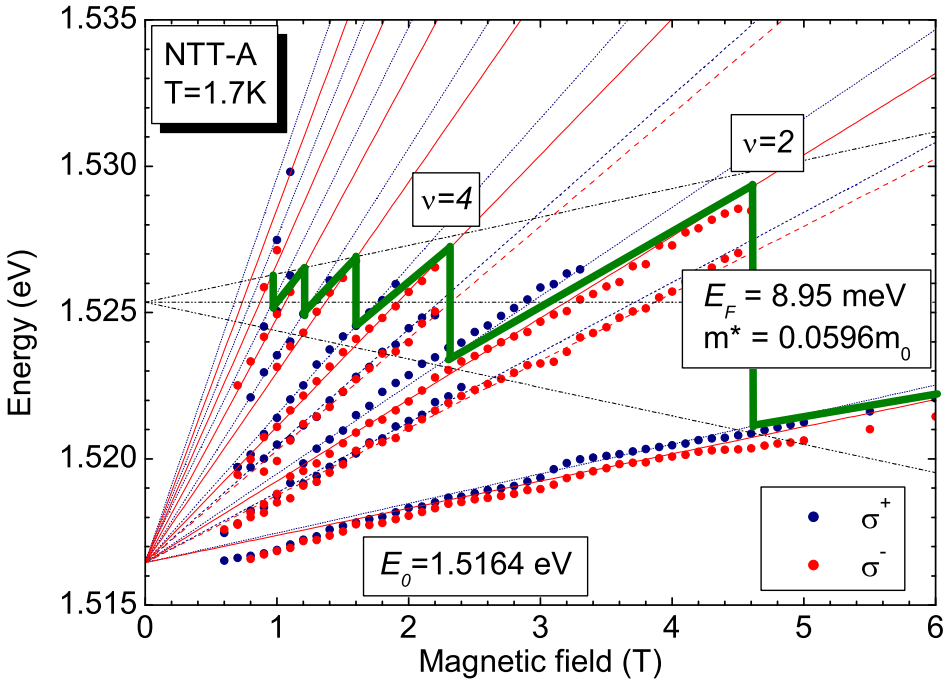

Figure 4.12: *Landau level fan chart of the NTT-A sample (d=20nm). Emission energy of σ^+ and σ^- emission vs. magnetic field. Calculated Landau levels are drawn as solid lines. The dashed lines mark forbidden transitions. Thick green line marks the Fermi energy oscillations. Figure after [3].*

we can write:

$$E = \hbar \frac{eB}{m_r c} \tag{4.8}$$

Thus the photoluminescence experiments allows to determine only the reduced effective mass:

$$m_r = 0.0586 m_0 \tag{4.9}$$

Using the electron effective mass, obtained for this sample from the cyclotron resonance measurements $m_e^* = 0.069\, m_0$ we conclude the hole effective mass $m_h = 0.4\, m_0$. This seems to be an acceptable value for the valence band heavy hole, which roughly validates the simple model used to analyse the data. It should be however noted that the cyclotron resonance measurements were performed on unilluminated sample and therefore above estimates can be only approximate.

Fermi energy. The oscillation of the Fermi energy of the 2DEG can be followed on the Landau level fan chart. At zero temperature it follows the energy position of the highest partially filled Landau level. At even filling factor the Fermi energy lies *exactly in the middle* between completely full and completely empty Landau levels. At odd filling factors the Fermi energy lies in the middle of the spin gap of the corresponding Landau level.

The observed oscillations can be extrapolated to zero magnetic field and the *zero field* Fermi energy can be determined. This is useful when the zero field emission is overlapped by other emission lines and can not be used for E_F evaluation. The wide quantum well NTT-C (d= 50nm) is such a case. Also the E_F in heterojunction samples, where the zero field emission is nonexistent, can be determined only from the oscillations analysis. Table 4.1 presents E_F values determined from the magneto – photoluminescence data.

Shifted energy scale

The features due to the many–body interactions in the 2DEG are weak and are lost in the scale of $\sim \hbar\omega_c$. A better visualisation of those features can be obtained by eliminating the huge cyclotron energy by the subtraction of a linear magnetic field function. The intercept is determined by the zero field emission energy and the slope by the magneto – photoluminescence field dependence. The choice of the slope is somewhat arbitrary as it reflects a supposed — single–particle picture dependence of the magneto – photoluminescence. Table 4.2 presents values of the parameters of the subtracted linear function. Different, acceptable slopes can give energies different by $\sim 1meV$ at $28T$. The resultant energy scale, called the *energy shift* scale, reflects the difference between the emission energy and the single–particle energy. Figures 4.13 - 4.14 compare the (raw data) of the magneto – photoluminescence of the NTT-C sample with the same raw data spectra represented on the *energy shift* scale.

	y=a · x + b	
sample	a (meV/T)	b (eV)
NTT-A	0.736	1.51615
NTT-B	0.63	1.5475
NTT-C	0.923	1.5084

Table 4.2: *Parameters of linear function subtracted from photoluminescence data with introduction of shifted energy scale.*

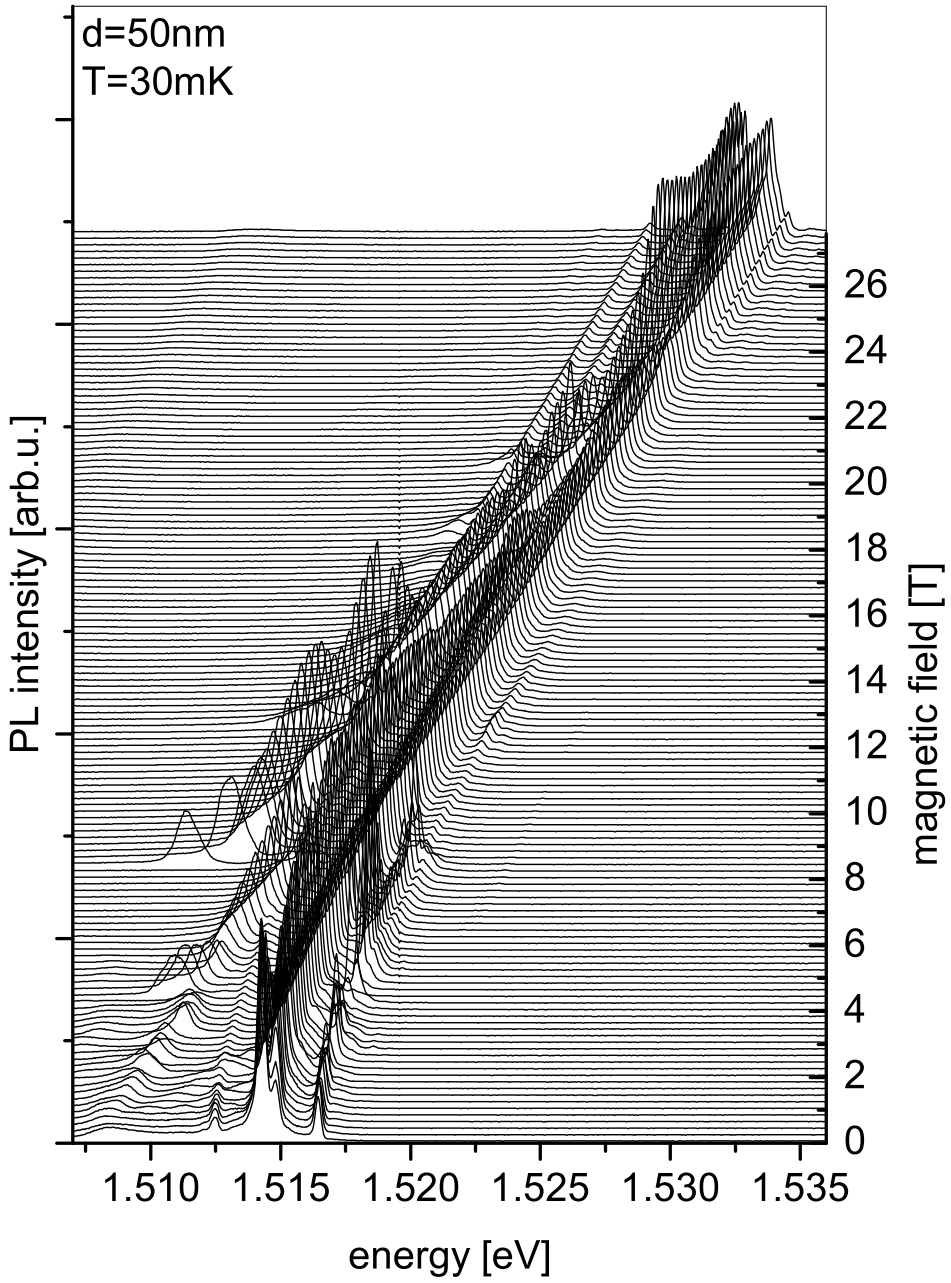

Figure 4.13: *Introduction of an energy shift scale allows better visualisation of the spectral features. Raw PL spectra of the NTT-C sample. See 4.14 for the same spectra moved in energy scale by a quantity linear with field (see text).*

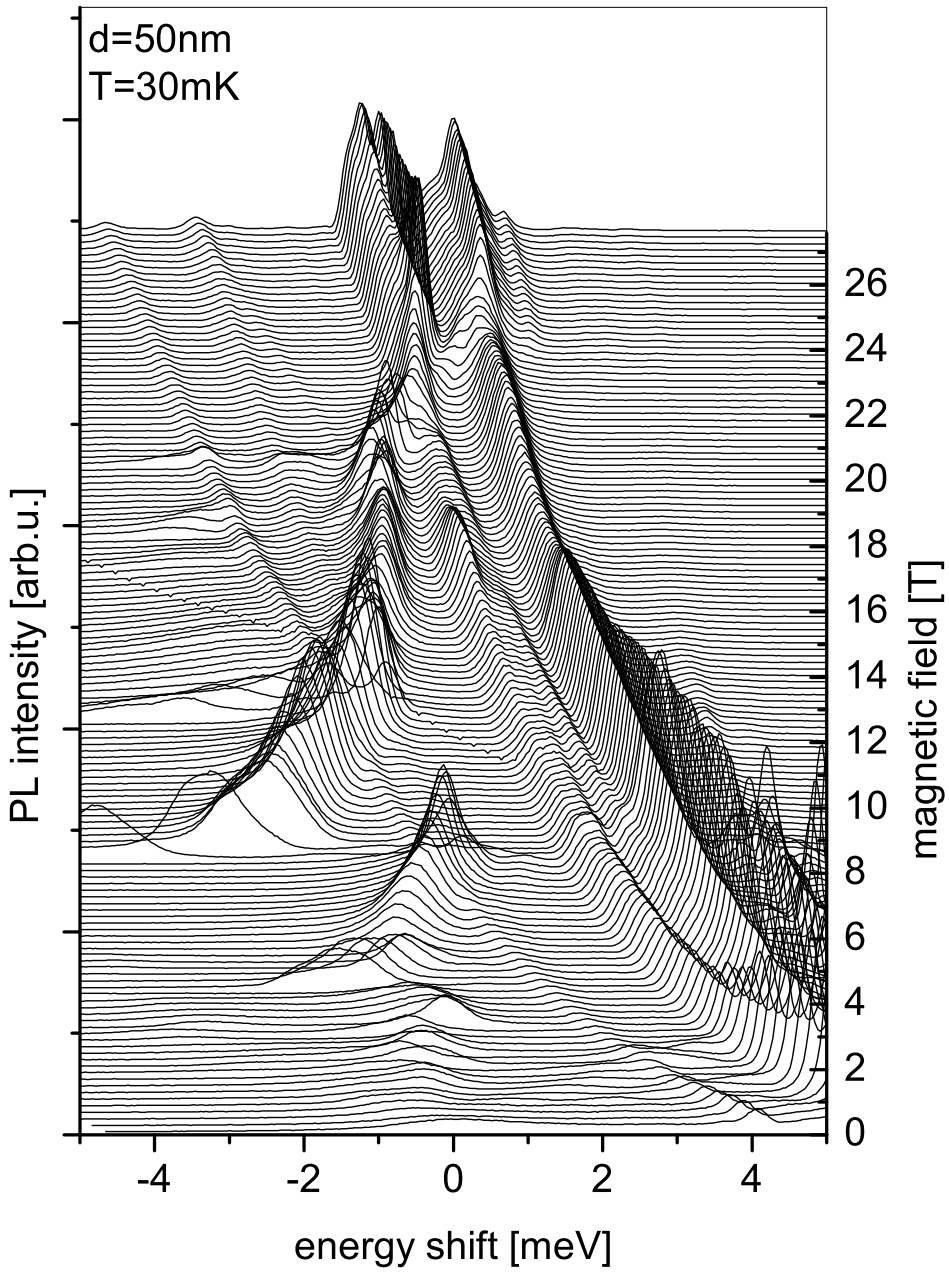

Figure 4.14: *Introduction of an energy shift scale allows better visualisation of the spectral features (see text). Spectra from Figure 4.13 moved in energy scale by a quantity linear with field: y=ax+b, where a=0.923meV/T b=1.5084eV .*

Band to band vs. exciton photoluminescence

The exact interpretation of photoluminescence from quantum well structures is still a subject of some controversy. Only two extreme cases of very low and very high electron concentration are well understood.

The primary parameter determining the two different cases is the ratio between the exciton radius, $a_B \sim 10nm$ in GaAs, and the mean distance between the 2D electrons [5]:

$$r_s \quad = \quad 1/\sqrt{\pi n_e} \approx 12nm \; for \; n_e = 2 \cdot 10^{11} cm^{-2} \tag{4.10}$$

In the case of very low concentrations the exciton radius is smaller than the mean $e - e$ distance and the formation of excitons is possible. In this case the exciton energy levels spectra can be described by models based on the description of the hydrogen atom [6, 7].

In the opposite case, individual electron hole pairs cannot be formed, instead a valence band hole interacts with the *whole* Fermi sea. In a simple approximation the optical spectra may be viewed as resulting from single particle transitions whereas the interactions are introduced in the form of a rigid shift of the bandgap (*bandgap renormalisation* [8]). Such a model may work to explain the zero field spectra but fails in magnetic fields where the interactions manifest themselves in the form of abrupt energy shifts or intensity variations at integer (and possibly fractional) filling factors.

The optical processes in the intermediate regime are the subject of great interest. In the lower density region ($\sim 10^{10} cm^{-2}$) the disorder plays an important role as it allows the formation of areas with finite electron density and completely depleted regions. The exciton (X) formation is possible in the regions without electrons while in the "electron puddles" three–particle complexes of one hole with two bound electrons (X^-, *charged exciton* or *trion*) have been observed in several materials (GaAs [9, 10], CdTe [11]).

The role of disorder in X^- formation is put into question by the experiments observing unbound charged exciton complexes that can drift freely in an applied electric field [12] which is opposed to the idea of charged excitons weakly localised by potential fluctuations from the remote ionised donors in the barriers [13].

The two possible spin configurations of bound electrons in the X^- give the possibility of creation of singlet (parallel) and triplet (anti–parallel) states of the charged exciton. The observation in the luminescence and magnetic field dependence of the two spin states is recently a subject of interest [14, 15, 16].

4.3.4 Photoluminescence in the quantum Hall regime

A single particle model, although useful to estimate the sample parameters, is clearly not sufficient to explain all features of the magneto – photolumi-

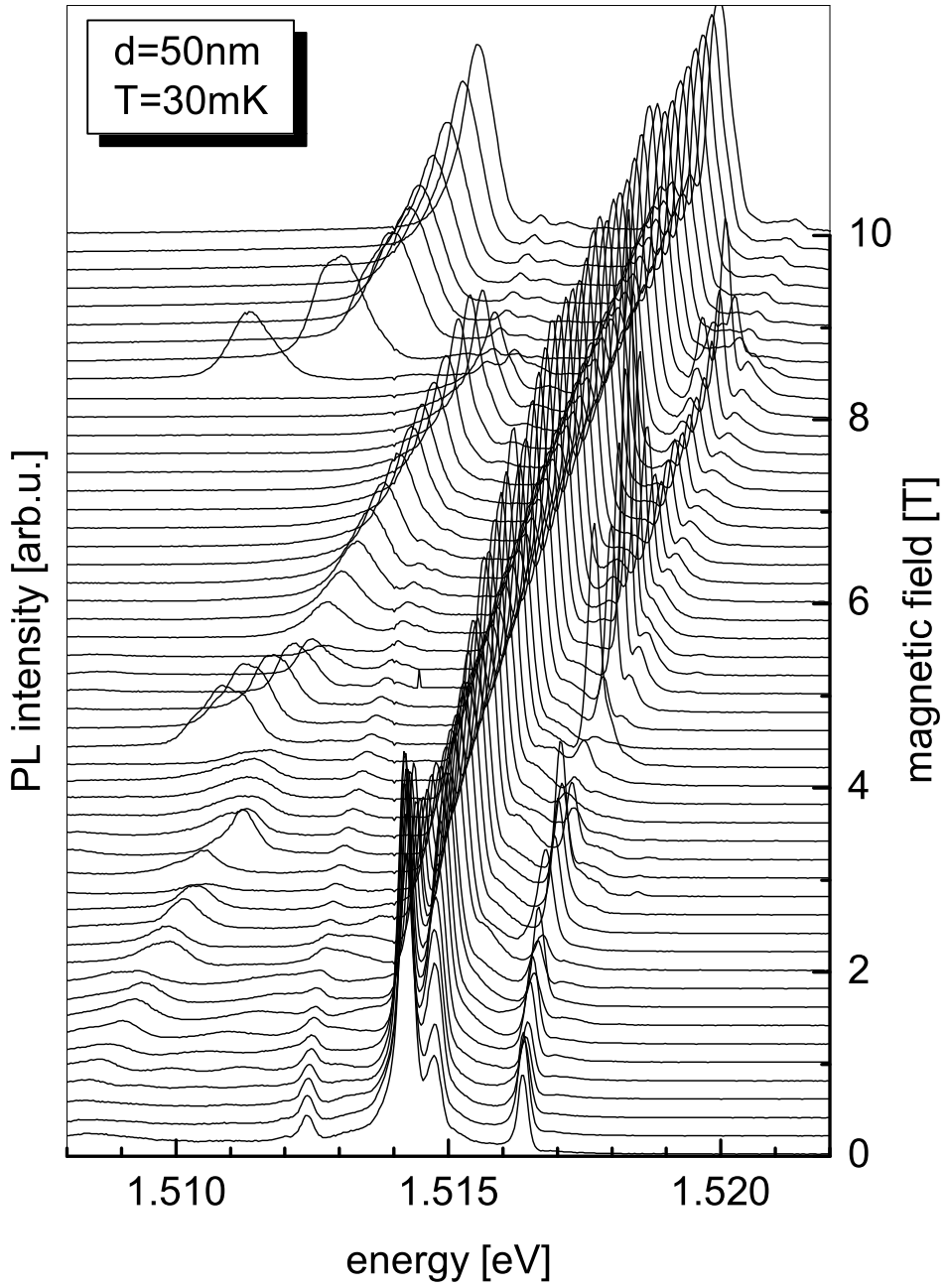

Figure 4.15: *Raw photoluminescence data every 0.2T between 0T and 10T. The sample is the 50nm NTT-C quantum well.*

nescence spectra of modulation doped quantum wells. As a matter of fact, the field evolution of the energy positions and intensities of the magneto – photoluminescence peaks is often far from a simple Landau level scheme of a single electron picture. The deviations are most pronounced in the vicinity of integer filling factors, when the Fermi energy changes its position between two adjacent Landau levels. The first works of a numerous literature were reported already around 1988.

Two possible causes of these deviations are the *electrostatics* (the redistribution of the electron concentration either between different electric subbands or even between the quantum well and the doped part of the sample) and *many–body interactions* (electron – electron as well as electron – valence band hole interactions). The deviation from the simple "Landau level geometry" is seen for our samples. The detailed discussion of these effects is beyond the scope of this work, however several selected data will be presented here. The most spectacular data were observed for the $50nm$ wide quantum well sample and they will be presented first. Then, the effects characteristic of filling factors $\nu = 1$ and $\nu = 2$ will be discussed.

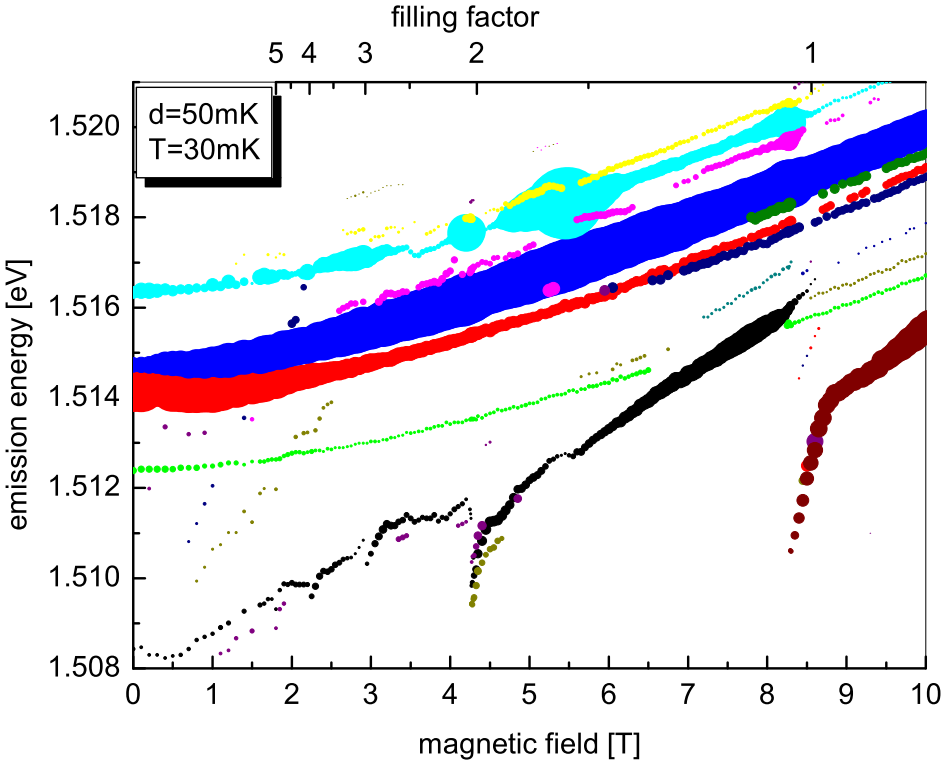

Figure 4.16: *Complex PL spectra with all 2DEG and bulk lines. Emission energy versus magnetic field. Circle diameter corresponds to line intensity.*

The $d = 50nm$ wide quantum well NTT-C sample has its 2DEG emission

energy below the emission energy of bulk GaAs excitons and its lines are nicely visible in the low field range in the area of interest of the integer filling factors. At higher magnetic fields the emission from bulk and quantum well overlaps and renders the sample useless for studying the fractional filling factors. Raw experimental magneto – photoluminescence data for the 50nm sample is presented in Figure 4.15. For clarity only spectra every 0.2T are shown. The emission energy of the observed emission lines is presented in Figure 4.16. The circle diameter corresponds to the emission intensity.

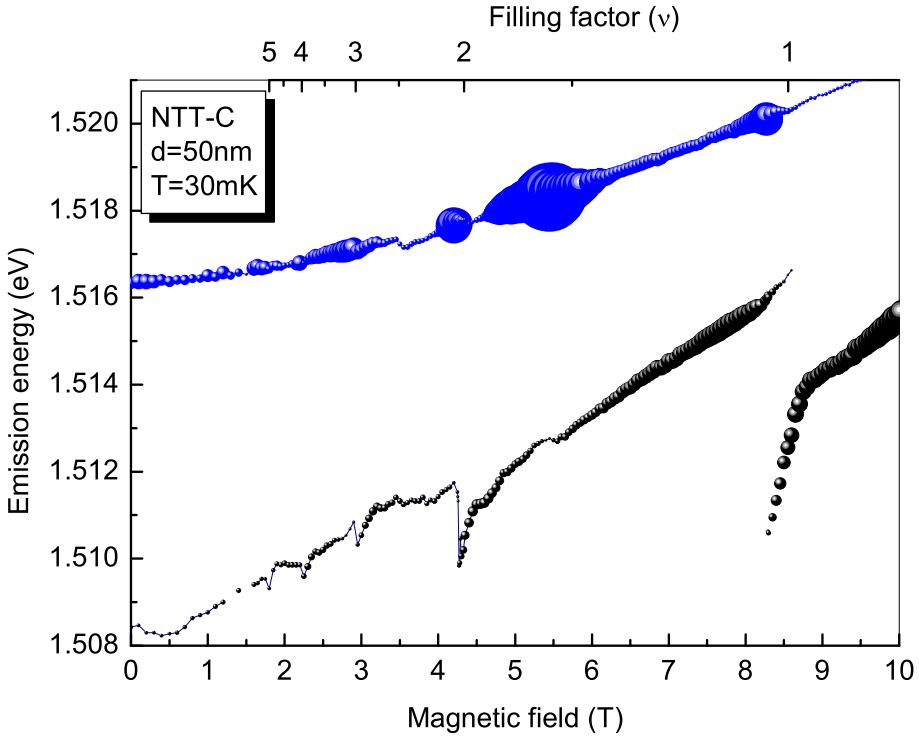

Figure 4.17: *Emission energy versus magnetic field. Circle diameter corresponds to line intensity. Only lines attributed to 2DEG emission from* 1^{st} *and* 2^{nd} *electron subband are shown.*

To make the picture clearer, only the two most pronounced and 2DEG–related lines are presented in Figure 4.17 These two lines correspond to emission associated with the lowest Landau level of the 1^{st} (ground) and 2^{nd} (first excited) electric subbands.

The low energy ($1.508eV$ at $0T$) emission from the 1^{st} subband shows characteristic energy discontinuities at integer filling factors. The 2^{nd} subband emission at higher energy ($1.516eV$ at $0T$) is continuous in energy position dependence, but its intensity variations are dramatic.

Different field dependences of the 1^{st} and the 2^{nd} subband emissions are visible at a first glance. The 1^{st} subband emission is linear in magnetic

field (when the abrupt changes at filling factors are ignored) while the 2^{nd} subband changes as $\sim B^2$.

The 2^{nd} subband emission is of an excitonic nature because of lower subband occupancy while the 1^{st} subband emission corresponds to the case of the high 2D electron concentration with the band to band emission.

The ground state emission has a complicated dependence in the vicinity of integer filling factors. The *redshift* of photoluminescence emission can be analysed in terms of two separate emission lines that can be distinguished around the discontinuities.

The evident transfer of emission intensity at integer filling factors starts a few tenths of a Tesla below integer filling factors, where the low energy line appears. The low energy, high magnetic field component gains rapidly in emission energy. The slope of the field dependence is constant and equal to $\Delta_{in} \equiv dE/dB = 7.7 \pm 0.3 meV/T$. Slightly above integer filling factors the slope of the high–field line changes again to match the slope of the low–field line but does not reach its emission energy and continues below the energy that that the low–field line would have if it continued above the filling factor. See Figure 4.20, right, for a closer view of the emission spectra around $\nu = 1$.

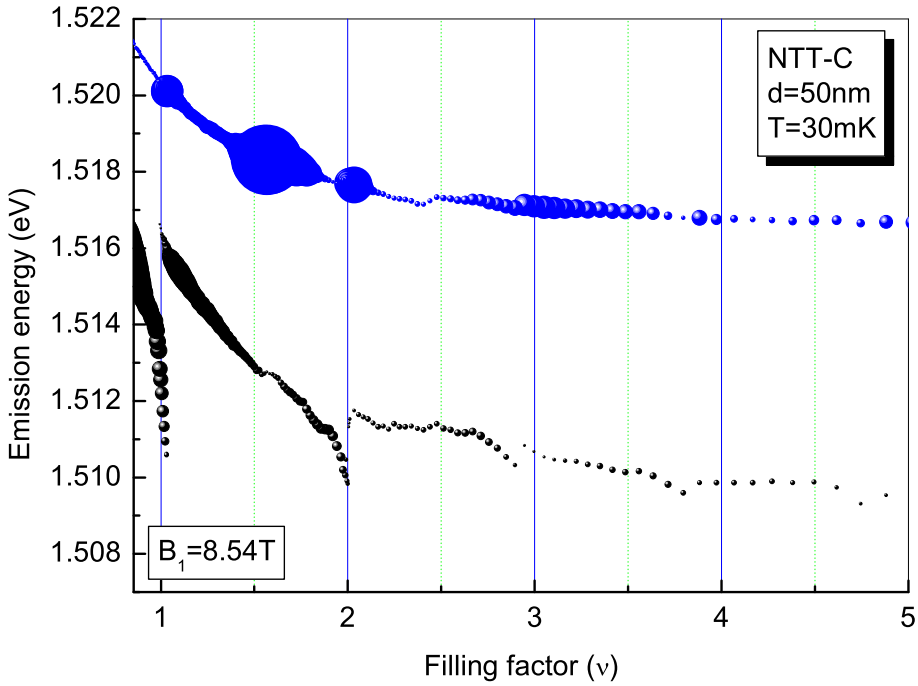

Figure 4.18: *Emission energy versus filling factor. Circle diameter corresponds to line intensity. Only lines attributed to 2DEG emission from 1^{st} and 2^{nd} electron subband are shown. Data from Figure 4.17.*

Figure 4.18 presents energy positions of PL lines at $T = 30mK$ bath

temperature plotted versus filling factor. The filling factor has been calculated from the magnetic field position of $\nu = 1$ which was determined to be $B = 8.54T$. While the features at $\nu = 1, 2$ fall nicely in place, higher filling factors features ($\nu = 3, 4, 5$) deviate slightly from expected positions on a filling factor scale.

To our knowledge, such dramatic changes in the magneto – photoluminescence spectra around integer filling factors have not been observed on any other similar structures and their actual origin remains unclear at the moment. Very likely the effects of the second subband population might be relevant in the explanation of the observed effect. Simple electrostatics do not however account for these effects. The data are interesting but their explanation remains open.

Second subband emission

To complete the presentation of the intriguing data obtained on this sample we focus now on the emission line related to the first excited subband. This emission shows a monotonic diamagnetic dependence in the energy position but strong variations of its intensity are observed.

As can be seen in Figure 4.18, there is an increase in intensity every time the filling factor approaches integer values with an exceptional increase at the filling factor $\nu = {}^3/_2$. The emission intensity drops nearly to zero below $\nu = 1$ and stays negligible for higher values of the magnetic field.

The origin of the intensity magneto – oscillations was proposed to be the change of screening of the Coulomb potential of the photo–induced hole. The screening properties are changed due to changes in the compressibility of the 2DEG.

Kukushkin and Timofeev [17] proposed that the origin of the intensity oscillation is in the kinetics of the carrier relaxation. This idea has been used to explain oscillations in intensity from the first excited subband in a single heterojunction [18, 19]. It has been observed that the rapid decrease of the intensity corresponds to the crossings of Landau levels of the 1^{st} subband and the lowest Landau level of the 2^{nd} subband. The increase in intensity is due to the slowing of the relaxation of carriers from the excited subband to the ground subband [20]. The shape of the intensity oscillations is determined by empty states in the ground subband and the relaxation matrix element. Oscillations in decay time are observed that are in phase with with intensity oscillations [21, 22].

Very dramatic changes in the 1^{st} subband emission are observed around filling factor $\nu = 1$. Figure 4.19 presents the magnetic field dependence of the emission energy and intensity from the 1^{st} and 2^{nd} subband of the widest quantum well NTT-C sample. The emission of the excited state behaves differently when crossing the $\nu = 1$ as there is no pronounced change in the emission energy while the intensity increases rapidly.

Time resolved experiments [23] allowed to measure the radiative recombination times in the vicinity of $\nu = 1$. It was found that the decrease of the emission intensity from the ground state, with a simultaneous increase from the 2^{nd} subband, is due to the ground state recombination time increase by a factor of ~ 7.

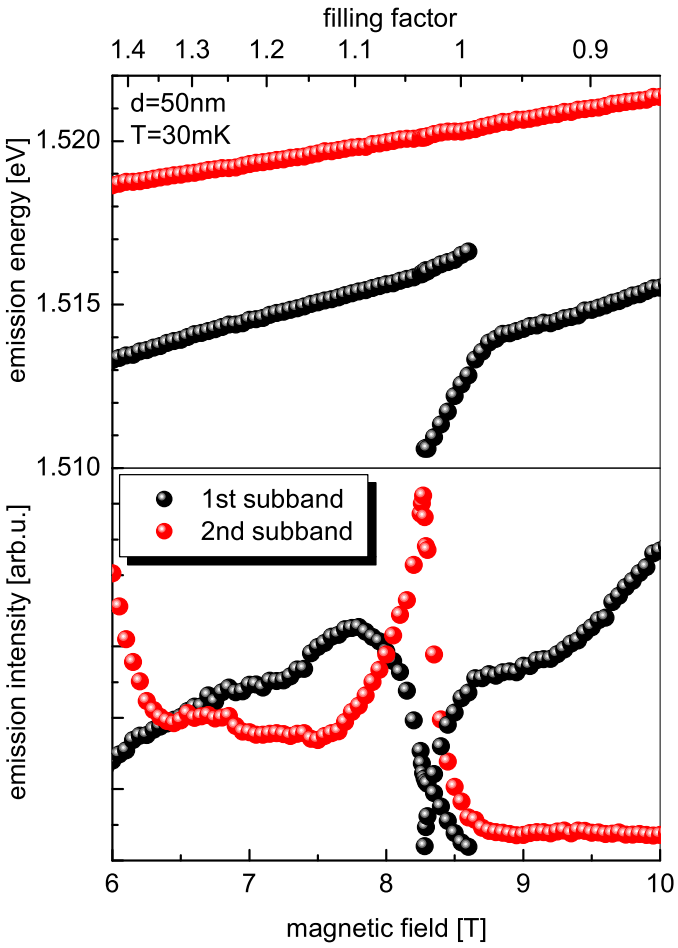

Figure 4.19: *Ground and excited states emission energy (top) and intensity (bottom) in the vicinity of $\nu = 1$ of the NTT-C sample ($d = 50nm$). The bath temperature is $T = 30mK$.*

4.3.5 Filling factor $\nu = 1$.

Figure 4.20 presents magneto – photoluminescence spectra in the energy–shift scale. The presented spectra lie in the vicinity of $\nu = 1$ for the three NTT samples. The differences in magnetic field dependence of the emission energies are obvious:

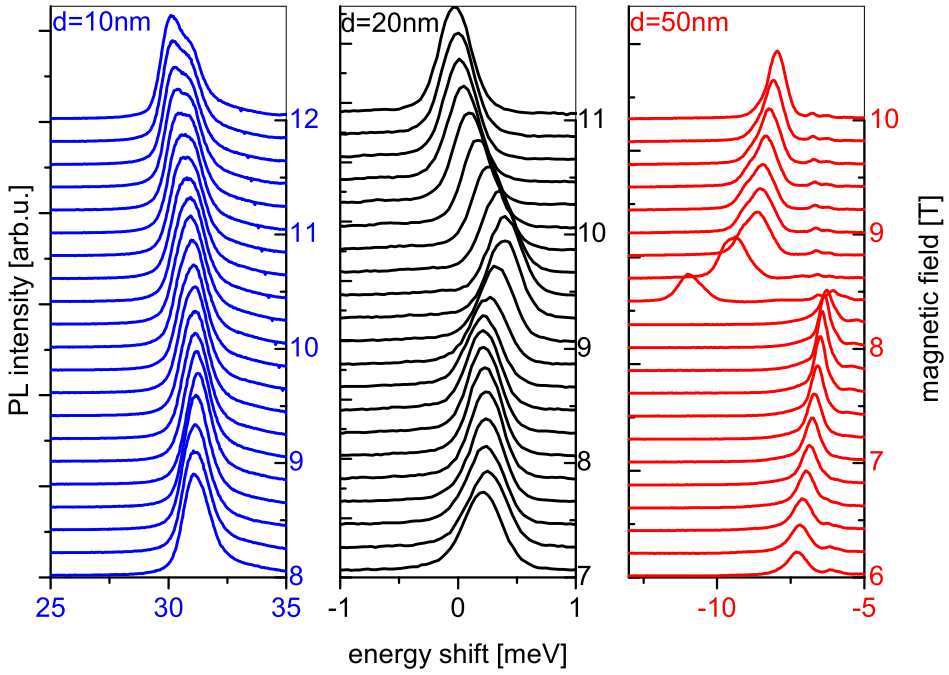

Figure 4.20: *Photoluminescence dependence on magnetic field in the vicinity of* $\nu = 1$ *for different 2DEG – valence band hole separation.*

- The emission from the narrowest quantum well ($10nm$, left) is roughly independent of the filling factor except for some narrowing of the photoluminescence line.
- The $20nm$ quantum well emission (middle) exhibits a $0.5meV$ *blueshift* at $\nu = 1$.
- The $50nm$ quantum well emission (right) has the most complicated behaviour. The existence of two lines is obvious and the emission energy displays a *redshift*.

All three NTT samples have different well widths but similar electron concentrations. The modulation doping on one side of the well leads to an asymmetric profile of the electrostatic potential along the crystal growth direction and therefore spatial separation between the 2DEG and valence band holes. This means that the characteristic electron–hole energy E_{e-h} is different in different samples but the characteristic electron–electron energy E_{e-e} is very similar for all three samples. The ratio of E_{e-h}/E_{e-e} is therefore different in each sample and is believed to be the reason for the characteristic, and different for each sample, magneto – photoluminescence behaviour in the vicinity of filling factor $\nu = 1$.

Each of the 2D electron systems of the NTT samples, whose emission is presented in Figure 4.20, falls into different regimes of interaction interplay.

The left–hand side graph of the emission from the d=10nm sample is the example where the the electron–hole interaction is much stronger than the electron–electron interaction. In this case, the photo–created valence band hole binds an electron from the 2DEG and creates an excitonic complex. The created electron–hole pair can be a neutral exciton or can correlate an additional negative charge and be a negatively charged exciton. In both cases the electron correlations in the 2DEG are destroyed.

The middle and the right–hand side graphs both correspond to similar regimes where interaction magnitudes are comparable $E_{e-e} \approx E_{e-h}$. A *blueshift* of the emission line (the d=20nm case) is observed when the electron–hole correlation is stronger: $E_{e-e} \leq E_{e-h}$. A *redshift* in the case of the d=50nm sample is observed when the 2D electron–electron interaction is stronger $E_{e-e} \geq E_{e-h}$.

These qualitative considerations can be compared with Figure 3.4 (p. 36) of the wavefunction overlap for the three samples.

Interaction interplay

The above analysis of the interaction interplay effects is based on the theory by Hawrylak and Potemski [24] and experimental work by Gravier et al. [25]. According to the authors the magneto – photoluminescence spectra reflect the interplay between the 2D electron – electron interactions and the 2DEG – valence band hole interactions. The analysis based on the theory will now be described in more detail.

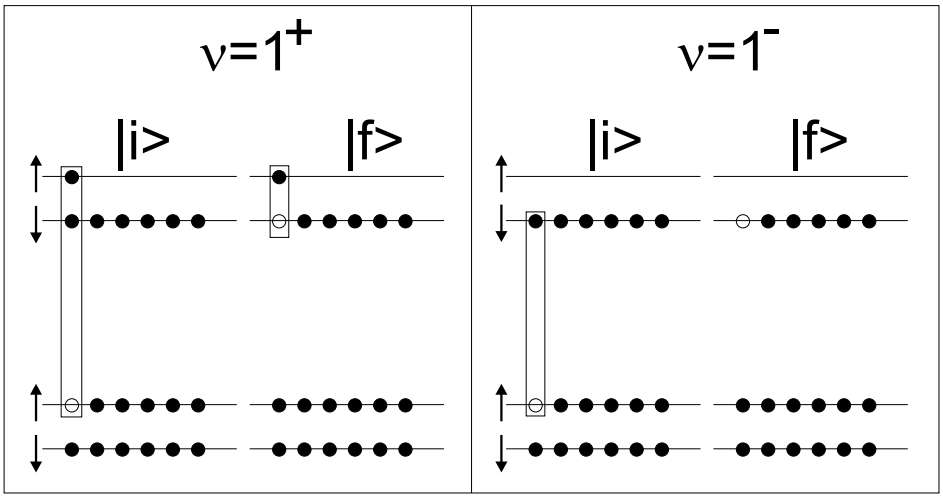

Figure 4.21: *A schematic picture of initial and final states of the optical recombination around* $\nu = 1$.

Figure 4.21 presents schematic initial $|i>$ and final $|f>$ states of the recombination process on both sides of the $\nu = 1$ and explains the origin of the energy change at filling factor 1.

On the right–hand side, at the filling factor $\nu = 1^{(-)}$, i.e. slightly less than 1, the state $|i>$ before the recombination consists of a hole in the valence band and a fully filled, spin split, lowest electron Landau level (LLL),

$$E_{|i>} = E_g + E_{|\nu=1>} \tag{4.11}$$

where E_g is the energy gap, and $E_{|\nu=1>}$ is the self energy of the $\nu = 1$ state.

After the recombination, in the final state $|f>$, the valence band hole has disappeared along with one electron from the lowest electron Landau level that took part in the recombination process,

$$E_{|f>} = E_{e-e} + E_{|\nu=1>} \tag{4.12}$$

where E_{e-e} is the electron electron interaction. The difference between the initial and final states is the recombination energy:

$$\hbar\omega^{(-)} = E_{|i>} - E_{|f>} = E_g - E_{e-e} \tag{4.13}$$

At filling $\nu = 1^{(+)}$ (left–hand side), slightly more than $\nu = 1$, the initial state has an additional electron in the spin–up Landau level. The initial state energy is given by:

$$E_{|i>} = E_g - E_{e-h} + E_{|\nu=1>} + E_z \tag{4.14}$$

where E_{e-h} is the conduction band electron - valence band hole interaction and E_z is the Zeeman energy. The recombination process removes the valence band hole and creates a hole in the LLL (spin–down), thus creating a "spin–exciton" which has the energy $E_{\uparrow\downarrow} = E_z$. The final state has energy:

$$E_{|f>} = E_{|\nu=1>} + E_{\uparrow\downarrow} \tag{4.15}$$

and the recombination energy is the difference between the initial and final states:

$$\hbar\omega^{(+)} = E_{|i>} - E_{|f>} = E_g - E_{e-h} \tag{4.16}$$

When crossing through $\nu = 1$ the difference $\Delta^{\pm}$ in the emission energy is given by:

$$\Delta^{\pm} = \hbar\omega^{(+)} - \hbar\omega^{(-)} = E_{e-e} - E_{e-h} \tag{4.17}$$

Thus, depending on the interaction magnitudes the shift of the emission lines will be either to higher energies if $E_{e-e} > E_{e-h}$ or to lower energies when $E_{e-e} < E_{e-h}$.

This qualitatively explains the different behaviour of the $20nm$– and $50nm$– wide quantum wells, shown in Figure 4.20.

4.3.6 Filling factor $\nu = 2$

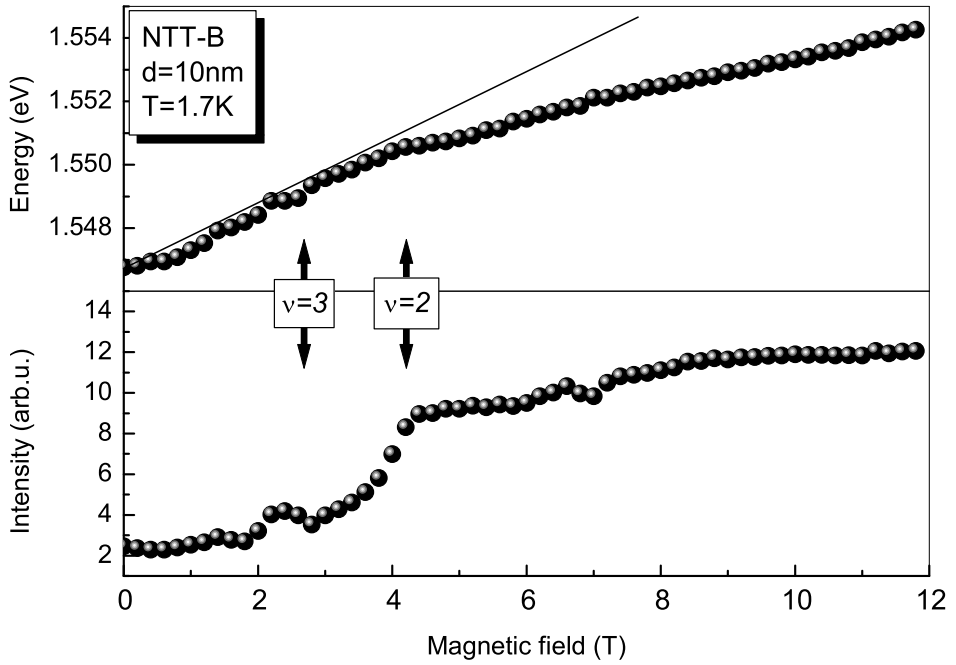

Figure 4.22: *The characteristic kink for excitonic–like emission at filling factor $\nu = 2$ is accompanied by a rapid increase of the emission intensity. Sample is the NTT-B, d=10nm quantum well. T=1.7K*

Figure 4.22 presents the energy and the intensity of the magneto – photoluminescence for the d=10nm NTT-B quantum well sample.

The emission energy is roughly *linear* with magnetic field until the filling factor $\nu = 2$ at B=4.2T, where it abruptly changes slope. Above the kink the dependence on magnetic field is *quadratic*.

While the change of the slope is characteristic only for the narrow sample, the accompanying increase of the emission intensity is observed independently of the well width (see Figures 4.11, p. 52 and 4.15, p. 59).

The linear dependence observed at low fields could be considered as a fingerprint of the band to band transitions. Above the kink (around $\nu = 2$) the emission displays a quadratic behaviour characteristic for an exciton.

The theoretical explanation by Rashba and Struge [26] in terms of *hidden symmetry* (due to the similarity of conduction band electron and valence band hole wavefunction) expects the effect to be observed only in symmetric quantum wells. On the other hand, the spatial separation of the electron and hole wavefunction was shown to be negligible so the $d = 10nm$ NTT-B sample could be treated as a nearly–symmetric system with a hidden symmetry.

A slightly different approach proposes the effect to be due to the shrinkage of the exciton wavefunction by the magnetic field. The localisation reduces the screening and filling of the bands and results in a *metal–insulator transition*. This effect does not depend on the shape of the potential in the quantum well and could be as well observed in asymmetric quantum wells.

The characteristic diamagnetic behaviour of the photoluminescence peak at filling factor $\nu \leq 2$ is an obvious indication of its excitonic nature. However, the exact identification of this exciton (whether neutral or negatively charged) is still a matter of discussion.

Valence band hole localisation in a heterojunction

Figure 4.23 shows that the magneto–photoluminescence of a 2DEG can be also observed in a simple heterojunction. The presented data have been obtained on the M1707 sample.

At first sight one might be surprised to observe the photoluminescence signal of a 2DEG from a simple heterojunction. The simple intuition is that the photo–created hole has a tendency to drift far away from the 2DEG due to the characteristic electrostatic potential profile of a heterojunction. Accordingly, the simple heterojunction does not usually show the 2DEG emission at zero magnetic field. But this emission often appears when a magnetic field is applied. The mechanism of blocking the drift of photo–created holes is not well understood although it is rather well established experimentally [27, 28].

As electrostatics certainly plays an essential role and the valence band hole states are vaguely defined, the magneto – photoluminescence spectra are rather poorly understood. The experiments on heterojunctions are however potentially very interesting as those structures show the highest quality.

The data obtained on the M1707 heterojunction sample are shown here for the sake of completeness but their detailed analysis in beyond the scope of this work.

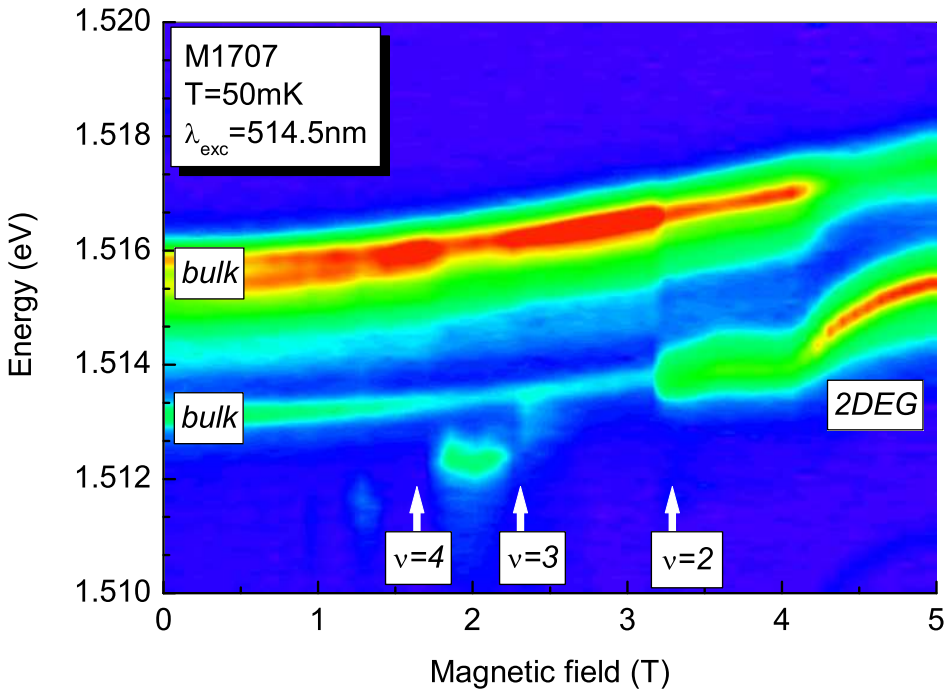

Figure 4.23: *Intensity map of the low field photoluminescence from the M1707 heterojunction.*

4.4 Conclusions

The measurements presented in this chapter allowed to thoroughly characterise our samples.

The sensitivity to illumination and its effect on transport properties in very low temperatures was discussed with a view to performing simultaneous transport and photoluminescence measurements in the fractional quantum Hall regime. Two relatively stable states, with a very low and a high electron concentration, were found to exist depending on the total illumination time. The state corresponding to 2DEG state under the conditions of the usual photoluminescence experiments was achieved after ~ 40 hours of low power illumination.

The characterisation of 2DEG properties by magneto – optical methods is done in the quantum Hall effect range of magnetic fields at very low temperatures. The analysis of the Landau level fan charts allows to determine reduced effective mass and electron concentration in the samples. The knowledge of the electron effective mass from the cyclotron experiments allowed to estimate the heavy hole electron mass.

Additionally, a concept of shifted energy scale which better reflects the changes of the emission energy is introduced and is used since.

The influence of the well width on the different behaviour at filling factor $\nu = 1$ due to different electron – hole interaction magnitude was discussed. This effect serves as an example of interaction interplay ranges, into which fall the three, specially chosen NTT samples. The two wider quantum wells were classified as having comparable magnitude of the 2D electron interactions and the magnitude of the electron – valence band hole interaction. The narrow quantum well has electron – hole interactions much bigger than 2DEG correlations and its photoluminescence has an excitonic character.

Also, a very different behaviour of a heterojunction photoluminescence in low magnetic fields due to the effects of valence band hole localisation was mentioned as a comparison with quantum well photoluminescence.

Bibliography

[1] L. J. van der Pauw, Philips Res. Repts. **13**, 1 (1958).

[2] G. Abstreiter, J. P. Kotthaus, J. F. Koch, and G. Dorda, Phys. Rev. B **14**, 2480 (1976).

[3] B. Chwalisz, *Photoluminescence of high-mobility electron gas in GaAs/AlGaAs quantum well*, Report, Grenoble High Magnetic Field Laboratory (2003).

[4] I. V. Kukushkin, K. von Klitzing, and K. Ploog, Phys. Rev. B **40**, 4179 (1989).

[5] B. Tanatar and D. M. Ceperley, Phys. Rev. B **39**, 5005 (1989).

[6] A. H. MacDonald and D. S. Ritchie, Phys. Rev. B **33**, 8336 (1986).

[7] M. Potemski, L. Viña, G. E. W. Bauer, J. C. Maan, K. Ploog, and G. Weimann, Phys. Rev. B **43**, 14707 (1991).

[8] S. Das Sarma and S. R. Eric Yang, Phys. Rev. B **41**, 8288 (1990).

[9] G. Finkelstein, H. Shtrikman, and I. Bar-Joseph, Phys. Rev. Lett. **74**, 976 (1995).

[10] H. Buhmann, L. Mansouri, J. Wang, P. H. Beton, N. Mori, L. Eaves, M. Henini, and M. Potemski, Phys. Rev. B **51**, 7969 (1995).

[11] K. Kheng, R. T. Cox, M. Y. d'Aubigné, F. Bassani, K. Saminadayar, and S. Tatarenko, Phys. Rev. Lett. **71**, 1752 (1993).

[12] D. Sanvitto, F. Pulizzi, A. J. Shields, P. C. M. Christianen, S. N. Holmes, M. Y. Simmons, D. A. Ritchie, J. C. Maan, and M. Pepper, Science **294**, 837 (2001).

[13] G. Eytan, Y. Yayon, M. Rappaport, H. Shtrikman, and I. Bar-Joseph, Phys. Rev. Lett. **81**, 1666 (1998).

[14] G. Yusa, H. Shtrikman, and I. Bar-Joseph, Phys. Rev. Lett. **87**, 216402 (2001).

[15] C. Schüller, K.-B. Broocks, P. Schröter, C. Heyn, D. Heitmann, M. Bichler, W. Wegscheider, T. Chakraborty, and V. Apalkov, Phys. Rev. Lett. **91**, 116403 (2003).

[16] C. Schüller, K.-B. Broocks, C. Heyn, and D. Heitmann, Phys. Rev. B **65**, 081301R (2002).

[17] I. V. Kukushkin and V. B. Timofeev, Adv. Phys. **45**, 147 (1996).

[18] V. E. Kirpichiev, I. V. Kukushkin, V. B. Timofeev, V. I. Fal'ko, K. von Klitzing, and K. Ploog, JETP Lett. **54**, 636 (1991).

[19] V. E. Zhitomirskii, I. E. Itskevich, K. von Klitzing, I. V. Kukushkin, and V. B. Timofeev, JETP Lett. **56**, 213 (1992).

[20] V. I. Fal'ko, Phys. Rev. B **47**, 3802 (1993).

[21] A. F. Dite, K. von Klitzing, I. V. Kukushkin, and A. I. Filin, JETP Lett. **54**, 642 (1991).

[22] A. F. Dite, I. V. Kukushkin, K. von Klitzing, V. B. Timofeev, and A. I. Filin, JETP Lett. **54**, 389 (1991).

[23] M. Dahl, D. Heiman, A. Pinczuk, B. B. Goldberg, L. N. Pfeiffer, and K. W. West, Phys. Rev. B **45**, 6957 (1992).

[24] P. Hawrylak and M. Potemski, Phys. Rev. B **56**, 97 (1997).

[25] L. Gravier, M. Potemski, P. Hawrylak, and B. Etienne, Phys. Rev. Lett. **80**, 3344 (1998).

[26] E. Rashba and M. D. Struge, Phys. Rev. B **63**, 045305 (2000).

[27] H. van der Meulen, J. Calleja, J. Sanchez, R. Hey, K. Frieland, and K. Ploog, Physica B **319**, 339 (2002).

[28] N. R. Cooper and D. B. Chklovskii, Phys. Rev. B **55**, 2436 (1997).

Chapter 5

Optical spectroscopy in the regime of the fractional quantum Hall effect

Les études optiques du gaz d'électrons bidimensionnel dans le régime de l'effet Hall quantique fractionnaire sont présentées dans ce chapitre. Une brève histoire de l'effet Hall quantique fractionnaire est d'abord ébauchée avec une discussion sur l'influence de la distance entre les électrons et le trou. Les résultats des puits quantiques de 10nm et 50nm sont ensuite présentés. Dans le premier cas, la photoluminescence ne montre pas de dépendance en fonction des états du 2DEG, car l'interaction électron - trou est trop forte. Dans l'autre cas, la luminescence du puit quantique plus large est superposée à la luminescence de l'autre partie de l'échantillon.

L'échantillon avec le puit quantique de 20nm est, donc représentatif pour des mesures optiques.

Dans les spectres une symétrie autour du facteur du remplissage $\nu = {}^1\!/_2$ est observée. Celle-ci ressemble à la symétrie des fermions composites de la famille $\nu = {}^1\!/_2$, bien connue des mesures de transport. Les fractions clairement visibles dans les spectres non traités correspondent aux facteurs de remplissage : $\nu = {}^1\!/_3,\ {}^2\!/_5,\ {}^3\!/_7,\ {}^3\!/_5,\ {}^2\!/_3,\ 1$.

En général, quand le 2DEG est dans un état incompressible l'énergie de la luminescence augmente. L'interprétation qualitative des mesures de la dépendance de luminescence en fonction de la température peut être faite dans le cadre de l'écrantage du trou par les électrons. L'incompressibilité à un facteur de remplissage fractionnaire résulte d'une incapacité du 2DEG de écranter le potentiel positif du trou optique dont l'énergie d'émission est élevée. Par contre, cette énergie est diminuée à l'extérieur d'un état incompressible du 2DEG, car les électrons ont la possibilité de répondre au potentiel du trou.

Les étendues du champ magnétique où l'énergie d'émission est élevée,

ont été interprétées comme analogues des plateaux de Hall observés dans les mesures de transport. Ça a été confirmé par des mesures de transport et de photoluminescence simultanés.

La dépendance de photoluminescence en fonction de la température montre également un autre effet connu des mesures de transport, à savoir le rétrécissement de la largeur des analogues des plateaux Hall avec la température. Cet effet est clairement visible à $\nu = 1/3$. Si la température est augmentée, le saut d'énergie d'émission de la fin de l'étendue d'énergie d'émission élevée, change sa position à champ magnétique vers le centre du plateau de Hall.

Des estimations théoriques ont été faite pour le cas du facteur de remplissage $\nu = 1/3$. L'émission de haute énergie a été attribuée à un quasi-exciton et l'émission de basse énergie observée en dehors d'un facteur de remplissage fractionnaire prévient d'un complexe formé d'un quasi-exciton et d'une quasi-particule.

5.1 Introduction

The effects of integer quantum Hall effect (IQHE) presented in the previous chapter to a great extent can be described in the single particle picture. The following chapter will be focused on the photoluminescence from the 2DEG in the regime of the fractional quantum Hall effect (FQHE). The existence of an energy gap at fractional fillings is solely due to the interaction between the 2D electrons.

The additional potential due to the existence of the valence band hole, inherent to a photoluminescence experiment, in the vicinity of the 2DEG perturbs the state of the 2DEG either by completely destroying the many body state of the 2DEG or only inducing a small perturbation. The interaction magnitude depends mainly on the hole separation from the 2DEG and is reflected as a change in the photoluminescence spectra.

5.1.1 FQHE in photoluminescence

The magneto–optics of the FQHE has already a nearly 20–year history. Magneto – photoluminescence and Raman scattering were used on all types of structures to explore the properties of the 2D electron (hole) gas.

Nevertheless, signatures of the fractional quantum Hall states have never been as clearly observed in optics as in transport measurements. In particular, a whole set of FQHE states has never been observed on one sample, but rather specific states such as $\nu = 1/3$ or $\nu = 2/3$ have been seen.

Magneto – photoluminescence is a relatively simple technique but becomes more difficult in the case of the FQHE studies. Such measurements imply low temperatures and therefore the use of very low excitation powers.

In the past, the use of geometrical optics was an obstacle in low temperature measurements with a dilution fridge. This major experimental constraint was overcome by the use of optical fibres allowing the optical access to the sample inside the dilution fridge. Optical fibres simplified the experimental setup of low temperature which become an accessible technique.

The PL signal from a good quality sample can be measured at very low excitation powers down to several nW/mm^2.

The main idea in a photoluminescence experiment in the fractional quantum Hall regime is to measure the energy required to remove one electron from the collective state of the 2D electron gas. This could be *a priori* done by measuring the recombination spectra of the valence band hole with the 2DEG. However, when the photocreated valence band hole perturbs the ground state of the 2DEG, the interpretation of the spectra becomes rather complex. The spectra depend very much on the details of the investigated structure and differ significantly between heterojunctions, acceptor doped heterojunctions or between quantum wells with different well widths.

5.2 Historical outline

5.2.1 Heterojunctions

The heterojunction samples nowadays have a high quality 2DEG with high electron mobilities in the range of $\sim 10^7 cm^2/Vs$. The drawback of such samples from the point of view studying interband transitions is the fact that valence band hole states are not localised, and therefore there is little overlap with electron states in the conduction band. Turberfield et al. [1] reported an intensity variation at the fractional states up to $\nu = {}^5\!/_9$ in a GaAs/AlGaAs modulation doped heterojunction. An intensity change at fractional filling factors was reported by Goldys et al. [2] in a low-density single heterojunction, and explained by screening effects.

5.2.2 Acceptor–doped heterojunctions.

Another type of structure intensively studied by Kukushkin and Timofeev [3, 4] is the acceptor doped heterojunction. The recombination process is a transition from the 2DEG to a hole bound to an acceptor state. Being neutral in the initial state and localised outside of the 2DEG plane, it does not perturb the 2DEG state.

In such structures, the luminescence reflects the *density of occupied states* in the conduction bands $I(E_i) \sim f(E_i - E_0)$ as the k–vector conservation rules allow transition regardless of initial k (the acceptor state is delocalised in the k–space).

By analysing the centre of mass of the spectra one can analyse the chemical potential discontinuities at fractional fillings. From a recombination to a localised hole spectra one can directly extract the mean energy $<E>$ of the 2DEG:

$$\frac{\sum I(E_i)E_i}{\sum I(E_i)} = E_0 + <E> \tag{5.1}$$

where E_0 is a reference level.

Given $\mu = \partial E_{tot}/\partial n$ where $E_{tot} = n < E >$ is the total 2DEG energy, the chemical potential is:

$$\mu = <E> + n\frac{\partial <E>}{\partial n} \tag{5.2}$$

From the above one can show that if $<E>= \hbar\omega_c \cdot f(\nu)$ and $\nu = n/n_0 B$ then

$$\mu = 2<E> - B\frac{\partial <E>}{\partial B} \tag{5.3}$$

An experimentally observed emission energy shift Δ_g can be related to the chemical potential discontinuity as:

$$\Delta_g = \mu^- - \mu^+ = B\Big[\frac{\partial <E>}{\partial B}\Big|_- + \frac{\partial <E>}{\partial B}\Big|_+\Big] \tag{5.4}$$

where $+, -$ denotes the high and low field side of the emission energy discontinuity.

Summarising, a discontinuity in the centre of mass of the spectra is interpreted as the energy gap of the fractional state.

On the other hand, there exist several difficulties in the measurements of the acceptor doped heterojunction photoluminescence. The spectra show large broadening of spectral lines and subtle FQHE features are not visible in the raw data. To overcome this a data treatment such as centre of mass calculation is used. Additionally, time resolved experiments [4] are preferred for those structures because of different possible channels of recombination.

5.2.3 Quantum wells

Much work has been done on the photoluminescence studies of the quantum well structures in the fractional quantum Hall regime.

The first report by Heiman et al. [5] of the inter–band recombination in GaAs/AlGaAs quantum wells showed a splitting of a recombination line into a doublet at $\nu = {}^2\!/_3$. Subsequent articles by the same group reported the intensity variations at $\nu = {}^2\!/_3,\ {}^2\!/_5,\ {}^1\!/_3$ along with nonlinear magnetic field

dependence of the recombination energy [6, 7]. The recombination process of the 2DEG in an external magnetic field has been a topic of experimental research for many years [8, 9, 10, 11, 12].

In quantum well structures the optically induced valence band hole is a big perturbation of the 2DEG state. The spatial separation of the 2DEG and the hole due to the electric potential in an asymmetric quantum well is determined by the well width. The width is an important parameter in the studies of a 2DEG by optical recombination. Depending on the ratio of the spatial separation (h) of the valence band hole from the 2DEG and the magnetic length (l_B), the ground state can be a neutral exciton, negatively charged exciton or a fractionally charged exciton.

Strict 2D limit. In the case of a strict 2D limit $h/l_B \ll 1$ (in other words, the 2DEG and the hole states are localised in the same plane) the photoluminescence of a structure with a 2DEG may be identical with the photoluminescence of an undoped quantum well. The lowest, k=0 initial state of a 2DEG and a valence band hole form a so-called *multiplicative state* which is undistinguishable from the *neutral exciton* [13, 14]. The neutral exciton is expected to be insensitive to the electron – electron interaction in the 2DEG. Such an interpretation discourages from using photoluminescence as a probe of the 2DEG state.

Finite width. Fortunately, such an assumption is not valid in the case when the h/l_B is finite, e.g. in quantum wells that are not very narrow. A *negatively charged exciton (trion)* X^- complex is expected to be formed in such cases [15, 16, 17]. The X^- has an overall negative charge ($-e$) as it consists of a hole ($+e$) with two bound electrons ($-2e$) and, as a charged entity, is expected to have some interaction with the 2DEG. This X^- state may be affected by the actual state of the surrounding 2DEG.

The negatively charged exciton depending on its spin and angular momentum can have several states: X_S^-, X_{TB}^-, X_{TD}^-, X_{SD}^- – singlet, bright triplet, dark triplet and dark singlet respectively [17, and ref. therein].

Recent experimental work by Yusa et al. [18], Ashkinadze et al. [19] on charged excitons in the fractional regime reported the observation of a singlet and two triplet states of the X^- in agreement with Wójs et al. Figure 5.1 shows peak energies of observed exciton complexes. Schüller et al. [20] reported a broad X_S^- emission redshift at $\nu = {}^1\!/_3$ in a 25nm wide, low mobility ($\sim 10^5 cm^2/Vs$) quantum well.

Fractionally charged excitons. Challenging theoretical predictions of excitonic complexes of a valence band hole and fractionally charged quasi–particles have been also proposed [15, 21, 22, 23]. Such complexes, called

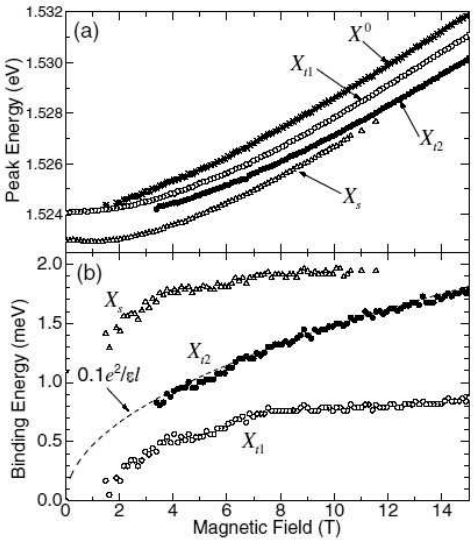

Figure 5.1: *Emission energies and binding energies of observed exciton complexes by Yusa et al. [18].*

fractionally charged excitons, can have fractional overall charge e.g. $\pm\,{}^1\!/_3 e$ of the $X^{\pm 1/3}$ complex around $\nu = {}^1\!/_3$.

When h/l_B is sufficiently large, the 2D e–e correlation is stronger than the e–h interaction and no additional quasi–particles are formed due to the valence band hole injection. Depending on the existence of the quasi–particles different possible complexes can be created [17], such as a hole bound with one, two or three quasi–electrons: hQE, hQE_2 hQE_3 in the case of $\nu > {}^1\!/_3$ where quasi–particles exist.

The screening efficiency of excitons by the 2D electrons — i.e. the 2D electron and valence band hole correlation — is expected to be the decisive factor in the determination of the emission energy. The screening depends on the 2DEG state (i.e. whether it is in an incompressible state or not) but also on the h/l_B ratio.

Current results The experimental results on the optics of FQHE presented in this work (see Section 5.3) can be divided into two distinct parts. One part concerning the narrow quantum well ($d = 10nm$) which falls in the regime of $h/l_B \ll 1$ with only excitonic effects, and a second part concerning wider quantum wells ($d = 20nm$ and $50nm$) that fall in the regimes of h/l_B where effects due to the incompressible states are observed (Table 5.1).

For magnetic field $B = 27.6T$ at filling factor $\nu = {}^1\!/_3$ the magnetic length is $l_0 \approx 47\mathring{A}$. The calculated 2DEG – valence band hole separation is firstly taken as the peak to peak distance and then corrected to be the separation

at half–height (HH) of the calculated probability functions. From Fig. 3.4 (p. 36) it is clear that in case of $10nm$ wide, NTT-B, quantum well the wavefunctions in fact fully overlap and the value of separation h should be zero. Thus, if we redefine the separation as the distance between the peaks outside the width at half–height we obtain $h = 0\mathring{A}$, $h = 10\mathring{A}$, $h = 170\mathring{A}$ for the $10nm$, $20nm$, $50nm$ wide quantum wells , respectively.

		e–h separation ($\mathring{A}$)		
sample	width (nm)	peak-peak	HH	h/l_0 region
NTT-A	20	~ 80	~ 10	$h \approx 2l_0$
NTT-B	10	~ 20	0	$h \approx 0$
NTT-C	50	~ 300	~ 170	$h \gg l_0$

Table 5.1: *Different h/l_0 regimes in the NTT samples for $l_0 \approx 47\mathring{A}$. See text and Fig. 3.4 on p. 36*

5.2.4 Raman scattering

Another way to explore the properties of the 2DEG in the fractional quantum Hall regime is by means of inelastic light scattering. Raman scattering experiments can measure the dispersion relations of the 2DEG states. Many such experiments have been performed by Pinczuk and collaborators [24] and most of the work has concentrated on the most pronounced fractional quantum Hall state $\nu = {}^1\!/_3$ [25, 26, 27].

According to Figure 5.2, the dispersion curve of the $\nu = {}^1\!/_3$ state has a nonzero energy (Δ_2) at $k = 0$ and a magnetoroton minimum at $k = 1/l_B$ which is the lowest energy (Δ_1) state.

The excitation with $k \to \infty$ corresponds to the creation of a separated free charge that can contribute to electrical transport, thus Δ_3 is the energy gap measured in transport experiments. It is a forbidden transition in inelastic light scattering experiments in the *backscattering* geometry.

The $k \approx 0$ excitations are allowed by the selection rules and correspond to spin–wave excitations.

On the other hand, scattering to the the lower energy, below the transport – determined gap has been observed and interpreted as scattering to the magnetoroton state at $k = {}^1\!/_{l_B}$. Such a process is also, a priori, forbidden by the wavevector conservation law.

Thus the essential problem in the interpretation of the inelastic light scattering results is the momentum transfer. The scattering to the magnetoroton minimum requires a large wavevector transfer which is not provided by the incident light (wavelength in the range of $\lambda \sim 800nm$). A mechanism

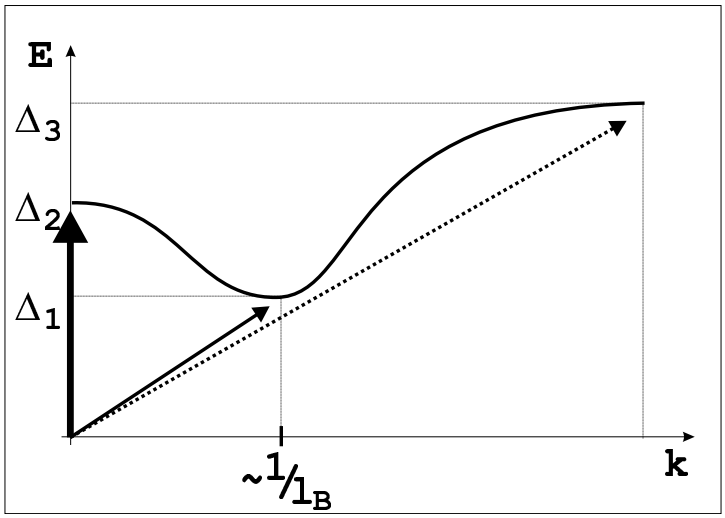

Figure 5.2: *Schematic magnetoroton–like dispersion. Possible types of excitations (allowed and forbidden) are marked as arrows.*

of disorder induced breakdown of wavevector conservation has to be invoked to explain the observation of the scattering at energies Δ_2.

5.3 Photoluminescence of the FQHE

This section presents experimental results on the fractional quantum Hall effect (FQHE) measured by magneto – photoluminescence spectroscopy. The data presented here is mostly gathered simultaneously with data presented in Section 4.3.4 on the integer quantum Hall effect. However, the presentation will be focused on features that are assumed to come from the fractional effect. Data will be presented in the magnetic field range $B = 8-28T$ which corresponds to the filling factor range $\nu = 1 - {}^1\!/_3$.

The samples were chosen specially for these experiments. Specifically, the 2D electron concentration is such that the $\nu = {}^1\!/_3$ is at $B = 27.6T$, just below the highest available magnetic field in the Laboratory. While other low concentration samples could have been measured in much lower magnetic fields the drive to use as high fields as possible was dictated by the magnetic field dependence of the energy gaps. In higher fields the energy gaps are larger and the effects are expected to be clearer.

5.3.1 Representative spectra

Figure 5.3 shows side–by–side the magneto – photoluminescence spectra of the three NTT quantum well samples.

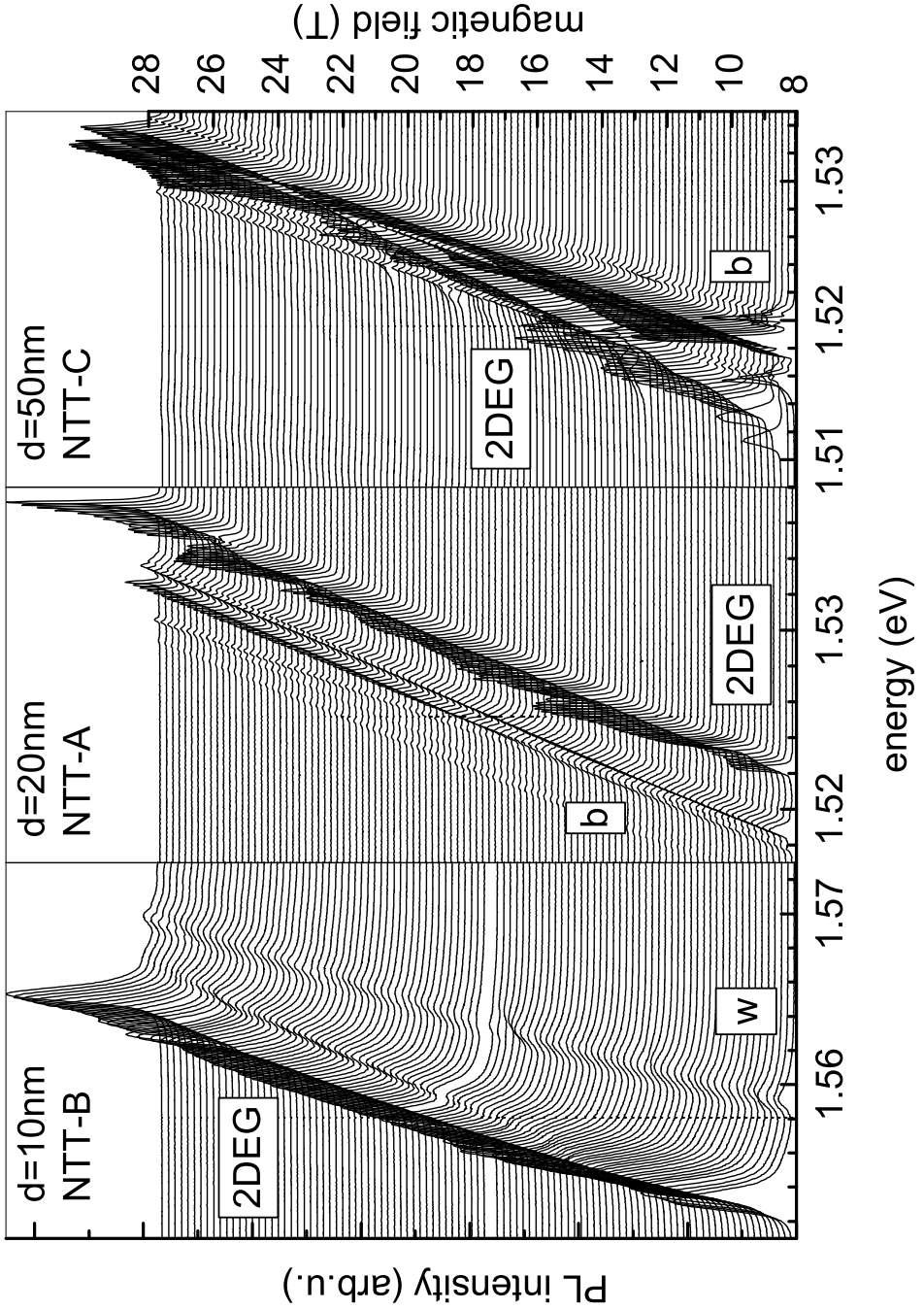

Figure 5.3: Raw magneto-PL spectra of the three NTT quantum well samples. The bath temperature is $30mK$.

The magnetic field range $B = 8 - 28T$ covers the filling factor range from $\nu = 1$ to $\nu = {}^1/_3$ in all samples. The photoluminescence line due to the 2DEG is marked ($2DEG$); other recombination lines visible on the spectra are due to bulk GaAs (b) and an empty quantum well (w). The 2DEG recombination lines are quantitatively different for different well widths. The spectra show intensity variations and in the case of the two broader samples there is a nontrivial energy dependence on magnetic field.

As the FQHE is a low temperature phenomena the features should be sensitive to an increase of temperature. Figure 5.4 shows the photoluminescence spectra for different temperatures at a constant magnetic field $B = 25.8T$.

The rise of the temperature is accompanied by a gradual intensity transfer from the higher energy doublet to the lower energy line. The low–energy line starts to appear around $100mK$ and overcomes the doublet intensity at $T_{tr} = 200mK$. The high–energy line of the doublet disappears completely above $215mK$ while the low–energy line of the doublet persists at a temperature as high as $300mK$.

From the temperature dependence it is clear that the base temperature of the 2DEG under illumination must be lower than $T \leq 150mK$. The phenomena observed in the photoluminescence are indeed low temperature effects and their sensitivity to temperature shows that their origin is indeed in the fractional quantum Hall states of the 2DEG.

Well width dependence

The change of the nature of the spectra for different well widths is due to the change of magnitude of the interaction between the valence band hole and the 2D electrons. The ratio of the hole— 2D electrons interaction to the mutual 2D electron interaction governs the different optical response (for discussion of the interaction interplay at $\nu = 1$ see Sec. 4.3.5, p. 64).

The samples fall into completely different regimes of the interactions and will be now discussed separately.

5.3.2 Narrow, $10nm$ quantum well. NTT-B.

Sample NTT-B has the narrowest quantum well. In this case the 2DEG electrons and the valence band hole are not spatially separated (Figure 3.4, p.36) and their interaction is the strongest. Such a strong interaction binds one or more 2D electrons with the valence band hole and creates excitonic complexes. The correlation interactions between the 2D electrons and the bound electrons are negligible and do not influence the binding energy of the exciton complex. One can say that the electron that forms the exciton is “removed” from the 2DEG.

Based on low magnetic field behaviour (around $\nu = 2$) the main PL line

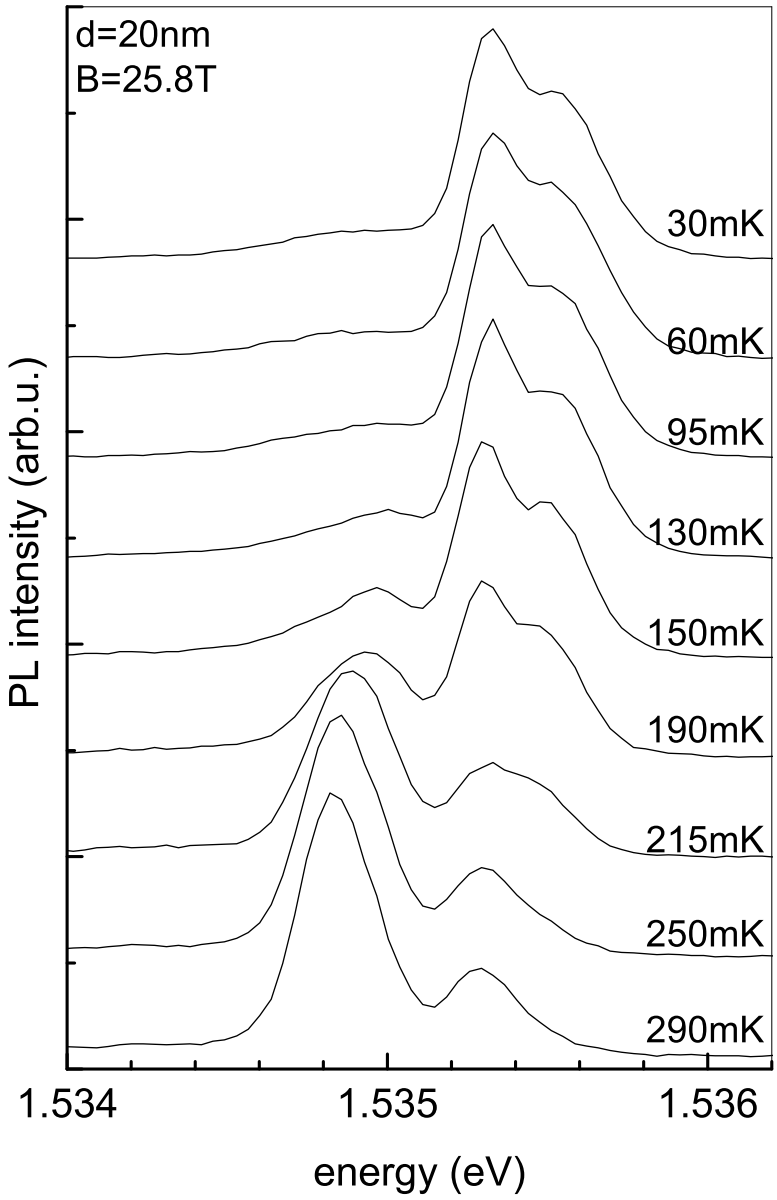

Figure 5.4: The temperature dependence of PL spectra of sample NTT-A at B=25.8T. Indicated bath temperature was set for each measurement while the low excitation power was kept constant.

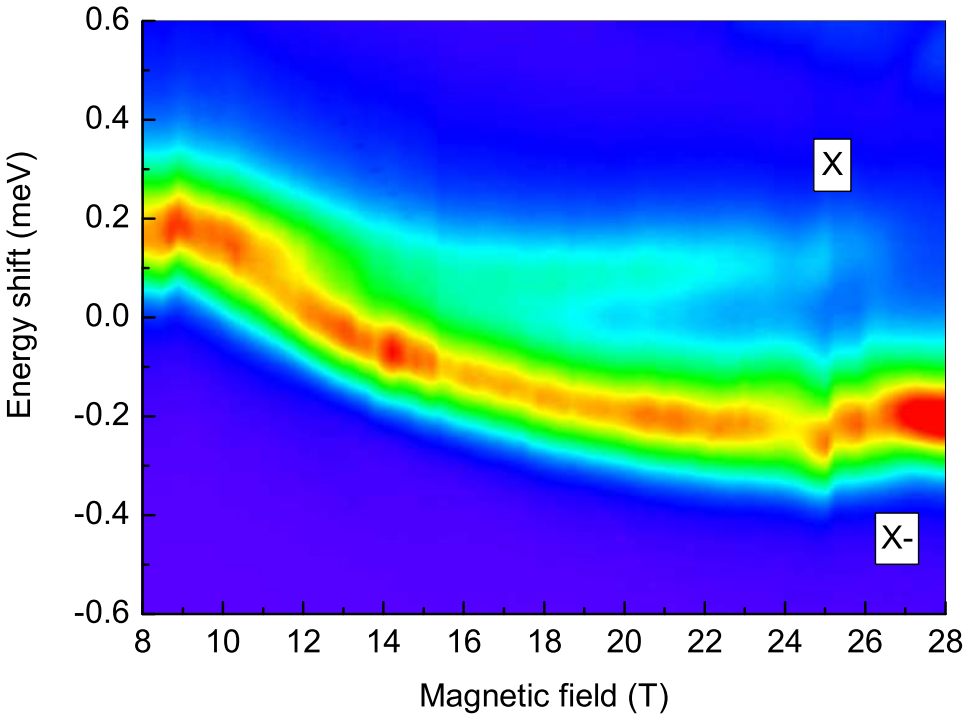

Figure 5.5: Intensity map of of the neutral (X) and negatively charged (X^-) exciton photoluminescence of the narrow NTT-B (10nm) sample.

has been attributed to a negatively charged exciton X^- [19] (see Fig. 4.22 in Sec. 4.3.6, p. 68).

The weak line above the negatively charged exciton in the Figure 5.5 is due to the neutral exciton (X) recombination. The line is nearly featureless in the region corresponding to the fractional quantum Hall regime and only a weak oscillation around $\nu = {}^1\!/_3$ ($B \sim 25T$) can be distinguished in the intensity map.

As the spectra consist of only one intense line, the magnetic field dependence can be analysed, with only little loss of information, by calculation of the centre of mass of the spectra:

$$CM = \frac{\int I(E)EdE}{\int I(E)dE} \tag{5.5}$$

where I(E) is the spectral intensity.

The position of the centre of spectral weight as a function of magnetic field is presented in Figure 5.6 and shows nearly no variations. The small changes of the integrated intensity of the spectra, presented as open symbols,

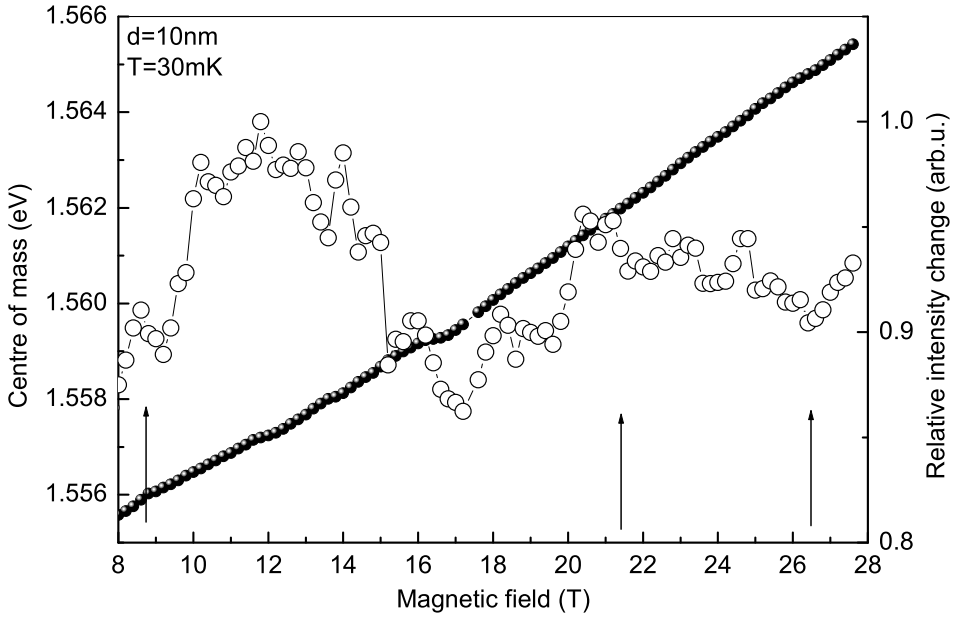

Figure 5.6: Centre of spectral weight and total integrated intensity of the NTT-B sample. Arrows mark intensity variations possibly due to $\nu = 1$, $\nu = {}^2\!/_5$, $\nu = {}^1\!/_3$ quantum Hall states of the 2DEG.

at the positions of fractional fillings are the only visible feature in the spectra that can be attributed to the changes of the 2DEG state.

5.3.3 Wide, $50nm$ quantum well. NTT-C.

Figure 5.7 presents the intensity map of photoluminescence of NTT-C, 50nm wide quantum well. Above the $\nu = 1$ only two fractions are visible that correspond to $\nu = {}^2\!/_3$ and $\nu = {}^3\!/_5$. All other fraction are overlapped by the bulk emission and are impossible to analyse.

The behaviour at the observed fractions is analogous to the previously found at the integer fillings (see Fig. 4.17, p.61). $\nu = 1$ is visible in Figure 5.7 at $B \approx 8.5T$. When approaching from lower magnetic fields in the vicinity of the filling factor a second line appears. The first line rapidly disappears while the second gains in intensity. The second line has lower emission energy which rapidly rises to the value approximately equal to that of the first line. The same qualitative behaviour is observed at $\nu = {}^2\!/_3$ but the slope ($\Delta_{fr}E$) is smaller: $\Delta_{fr}E = 3.5 \pm 0.5 meV/T$ compared to the slope at integer fillings $\Delta_{in}E = 7.7 \pm 0.3 meV/T$.

The interpretation can be based on the previous analysis of photoluminescence from acceptor doped heterojunctions. According to [3], the emission energy jumps at filling factors correspond to the energy gaps. Table 5.2

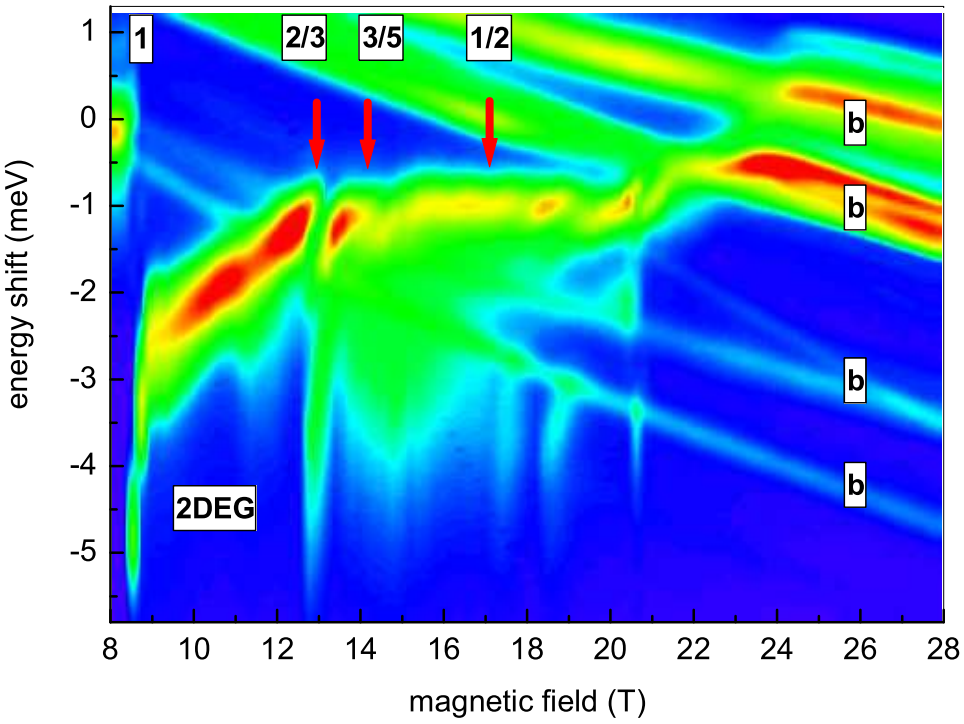

Figure 5.7: *Intensity map of the photoluminescence of the NTT-C sample at T=30mK.*

presents the determined values of the fractional filling factors energy gaps from such reasoning.

The magnitude of the obtained gaps are in agreement with what is usually determined by other methods.

5.3.4 Intermediate, $20nm$ quantum well. NTT-A.

Figure 5.8 presents the magneto – photoluminescence spectra of the $d = 20nm$ quantum well sample taken at base temperature $T = 30mK$. Raw spectra from Figure 5.3 were shifted in energy scale according to Sec. 4.3.3 (p. 55). The spectra drawn with thick lines mark indicated filling factors. The procedure of defining the field position of the filling factors was discussed in Section 4.3.3(p. 50).

In the case of the NTT-A sample the interplay between the two interactions is the most interesting. The valence band hole is far enough not to destroy the 2D electron–electron interactions and the electron correlation significantly affects the emission spectra.

Figure 5.9 presents data from Figure 5.8 as an intensity map. The striking feature is the *composite fermion symmetry*, observed for the first time

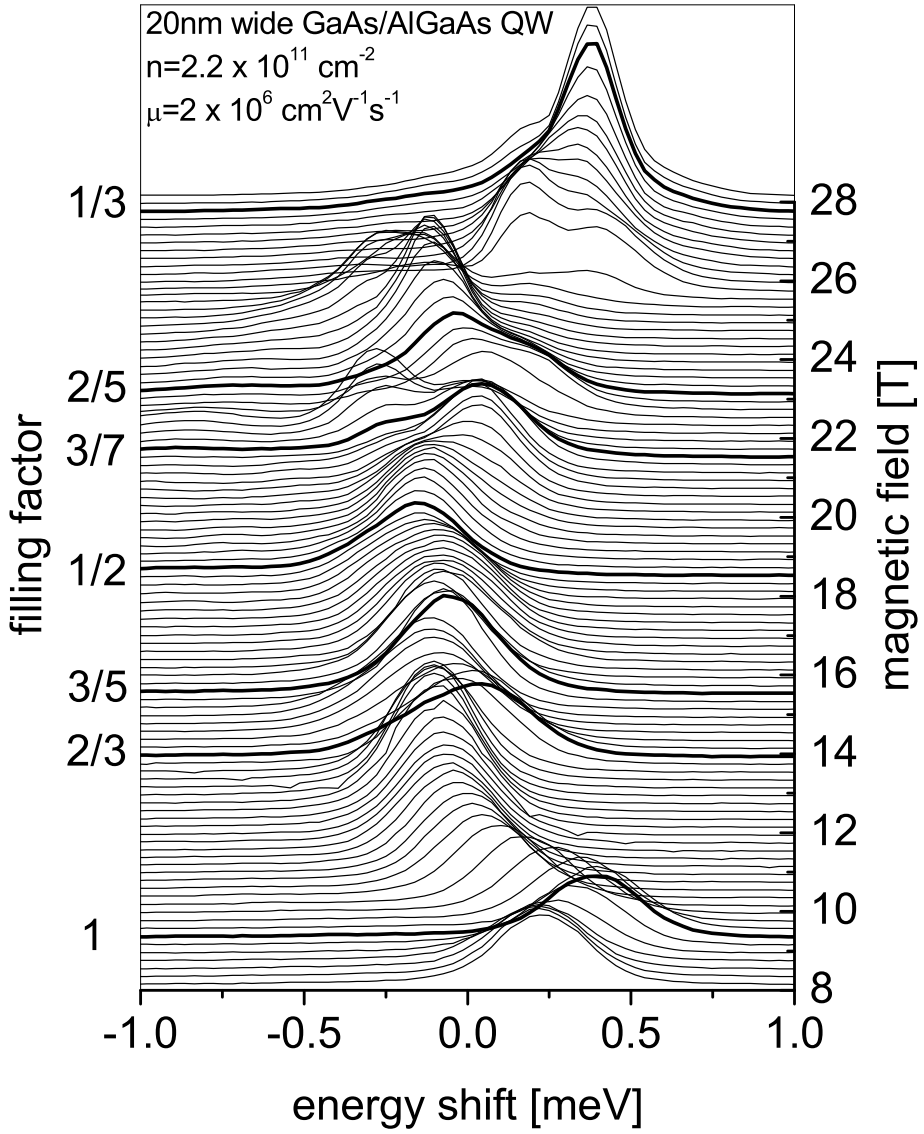

Figure 5.8: *Magneto – photoluminescence spectra from 8T to 28T at $T = 30mK$. Marked spectra correspond to indicated filling factors. Data for the $d = 20nm$ NTT-A quantum well sample.*

filling factor	energy gap (meV)
$\nu = 1$	2.5
$\nu = {}^{2}/_{3}$	0.7 - 0.4
$\nu = {}^{3}/_{5}$	0.1 - 0.2

Table 5.2: *Energy gaps at fractional filling factors determined from the energy jumps of the emission from NTT-C (d=50nm) sample presented in Figure 5.7. See also Sec. 5.2.2.*

in an optical experiment. On both sides of the filling factor $\nu = {}^{1}/_{2}$ there is a general trend of the spectral weight to shift slowly to higher emission energy creating a minimum at exactly $\nu = {}^{1}/_{2}$. On top of the slow shift there are more rapid changes in emission energy, symmetrically placed around $\nu = {}^{1}/_{2}$. Those changes in energy are attributed to fractional filling factors. The filling factor position of the most pronounced features are marked with arrows.

Such symmetry around $\nu = {}^{1}/_{2}$ is routinely observed in transport experiments and corresponds in Jain's theory to the composite fermions integer quantum Hall effect observed on both sides of the effective magnetic field $B^* = 0$ at the $\nu = {}^{1}/_{2}$.

For every odd-denominator fraction the photoluminescence shows a common behaviour. Every time a fractional filling is reached there is a rapid increase in the emission energy. At $\nu = {}^{1}/_{3}$, where the effect is the most pronounced, the region of the increased emission energy spreads over $\sim 1T$. Other fractional filling factors of higher orders are less pronounced and their regions of higher emission energy are much narrower ($\sim 0.5T$ for $\nu = {}^{2}/_{5}$). Generally, the apparent trend of weaker features at higher order filling is consistent with the usual transport results.

Temperature dependence

The magneto-photoluminescence spectra of the NTT-A sample were measured for different bath temperatures. The temperature dependence at an arbitrary fixed magnetic field (Fig. 5.4) showed that the effect is indeed a low temperature phenomenon. The spectra in Figure 5.10 allow to analyse the effect of temperature increase at other fillings. The base bath temperature ($30mK$) yields the most pronounced energy shifts; simultaneously the multi–peak nature is the most visible. At higher temperatures the jumps become smooth or disappear completely.

A first look at the temperature dependence can be effected by means of the centre of spectral weight (Eq. 5.5). From its analysis a general trend due to the temperature change can be deduced. The spectral centres of weight are plotted in Figure 5.11.

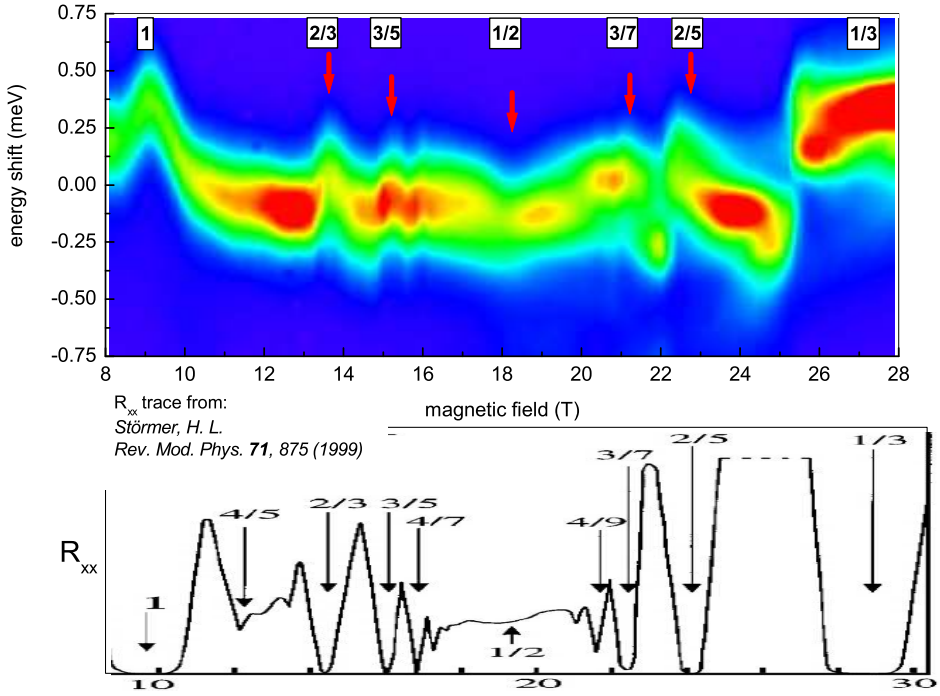

Figure 5.9: *Intensity map of the photoluminescence from a 2DEG in the fractional quantum Hall regime. The family of FQHE features resembling the composite fermion symmetry is visible. Model transport data from [28] are attached for comparison.*

Qualitative interpretation

A qualitative interpretation of the magnetic field dependence of the photoluminescence spectra and the effects of the temperature can be done in terms of the effect of screening of the valence band hole by the 2D electrons.

Depending on the 2DEG state, whether the 2DEG is in an incompressible state or not, the effective screening efficiency is different. In the case of an incompressible liquid of 2D electrons the charge accumulation on the positively charged valence band hole is hindered, and the emission is characteristic of a neutral exciton.

On the other hand, when the 2DEG is in a *compressible* state, the spectral weight of the emission spectrum shifts down in energy, as if there were an additional increase of the exciton binding energy. The 2D elections are free to respond to the appearance in their vicinity of the positively charged hole. The electrons can adjust their position so as to minimise the total energy and create an excitonic complex. Emission from such a complex has lower energy than neutral exciton emission.

At low temperatures, the emission energy is higher due to the inability

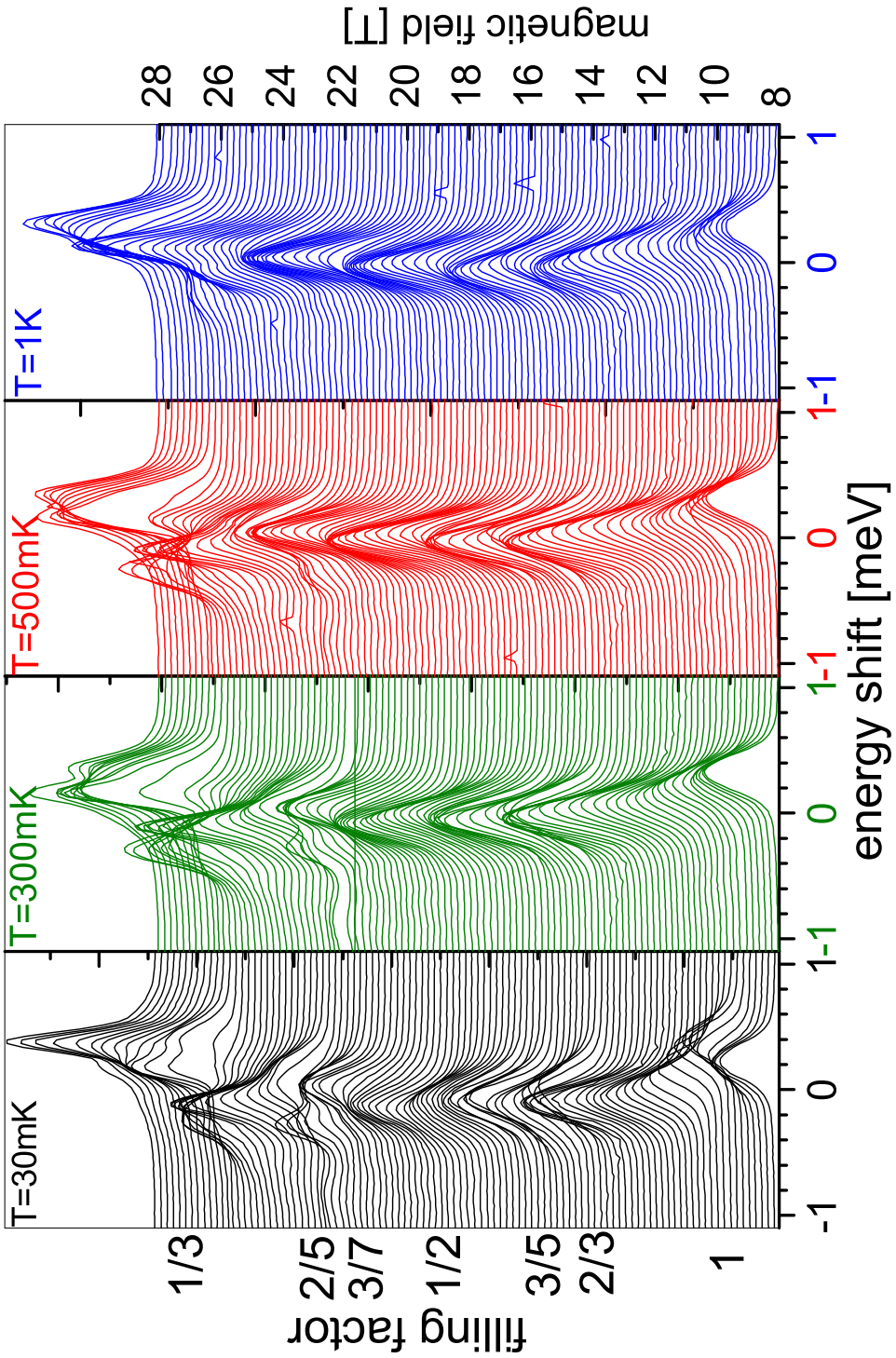

Figure 5.10: *Raw, represented in shifted energy scale, photoluminescence data for different bath temperatures. Sample is NTT-A (d=20nm).*

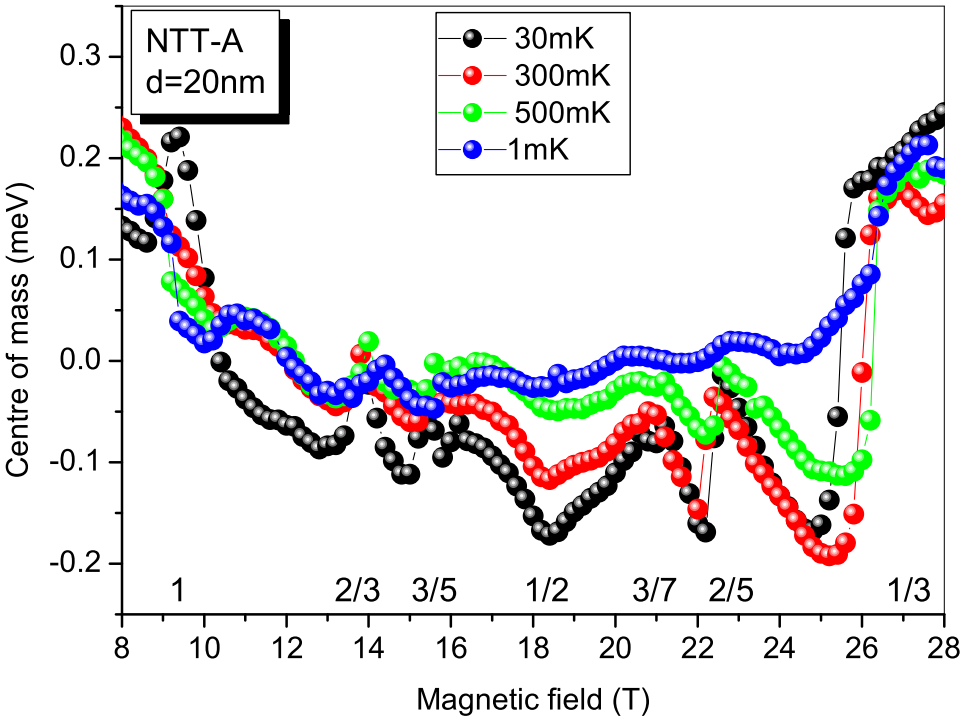

Figure 5.11: *Centre of mass of the PL spectra presented in Fig. 5.10*

of the 2DEG being in the incompressible quantum liquid phase to respond to the hole.

An increase of temperature can destroy the incompressible state. Thus, transitions of the spectra due to magnetic field change or due to temperature increase can be treated in complete analogy.

For a system in a given fractional filling the change in magnetic field changes the level degeneracy, thus changing the relative occupancy of the highest occupied Landau levels by e.g. promoting a particle to higher level. In other words, the change of the magnetic field changes the distribution function. The increase of temperature also changes the distribution function and destroys the incompressibility.

The first effect is observed, at temperatures low enough to allow the creation of the incompressible states, as the rise of emission energy at fractional fillings. The temperature affects the magnitude of energy discontinuities. At high temperatures the incompressible states do not exist, thus the emission energy is not increased.

Detailed data analysis

Although an analysis by the means of the centre of spectral weight is sufficient for a rough overview, it has several weak points because of its integration over the energy range. First of all it fails to distinguish spectra with more than one emission line from spectra with one broad line. This can result in energy shifts when two lines change relative intensities.

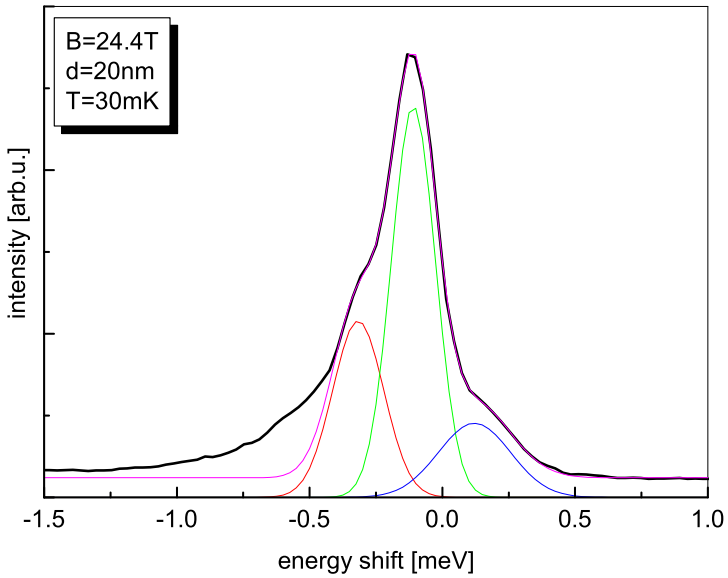

Figure 5.12: *Example PL spectrum (thick line) at $B = 24.4T$ and three fitted Gauss peaks and their sum (thin line).*

When an emission spectra contains more than one spectral line (for an example see Figure 5.12) a different approach is needed. The spectra need to be deconvoluted. A fitting example shows a PL spectrum at $B = 24.4T$ marked by a thick line. Three fitted Gauss peaks and their sum are also plotted.

The three Gaussian peaks fit very well the given spectrum with the exception of a low energy tail where at least one additional weak peak is needed. Adding the missing peak at $-0.5meV$ to the fitting procedure does not yield unequivocal results. The energy position of the missing peak is too close to the next peak for a good fit. Since the use of too many fitting parameters should always be avoided as it can distort the fitting, the tail was not fitted at all.

A fitting procedure was used to separate the emission lines that lie so close to each other that an exact determination of their energies is not possible by other methods.

Points in Figures 5.13 and 5.14 represent fitted peaks to the spectra

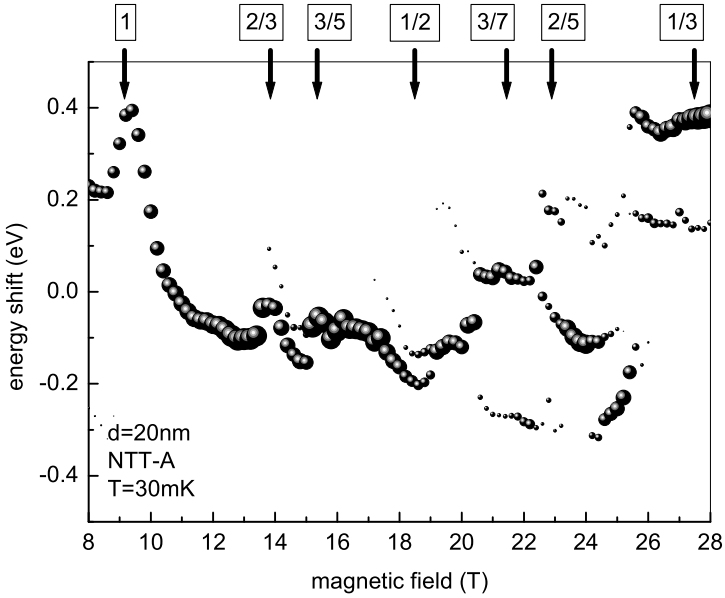

Figure 5.13: *Energy positions of fitted Gauss peaks. Peak intensity is represented by a dot size.*

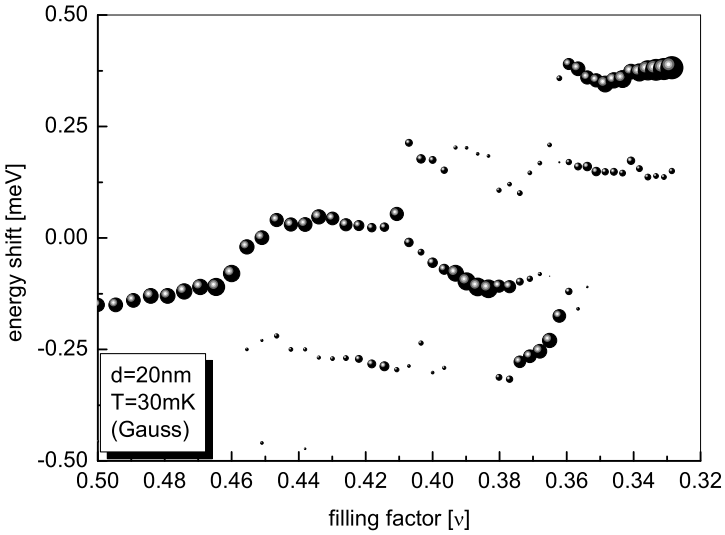

Figure 5.14: *Same data as in Fig. 5.13 plotted versus filling factor below* $\nu = {}^1\!/_2$ *(above* $B = 18.4T$*). Energy positions of fitted Gauss peaks. Peak intensity is represented by a dot size.*

from Figure 5.8. The circle diameter corresponds to the amplitude of a fitted peak. The data is plotted versus magnetic field between $8T$ and $28T$ and in the filling factor scale, respectively. The filling factor scale starts below $\nu = 1/2$ what corresponds to a field $B = 18.4T$. For some magnetic field values (e.g. $25.2T$) up to three different emission lines were found.

Also, spectra taken at other temperatures were fitted and are plotted in Fig. 5.15 on top of the intensity maps for comparison. With the fitted peak intensities and positions, more subtle temperature effects can be analysed.

When the temperature is raised, the energy shift at $\nu = 1$ disappears at $T = 300mK$when it is visible as a weak intensity change. In other fractional filling factors the main line consists of several overlapping lines only at the base temperature. In higher temperatures (300mK) they are visible as energy jumps.

The energy jumps magnitude diminish with increasing temperature. Above the field corresponding to $\nu = 1/2$, the multi peak structure persists at 300mK at filling factor $3/7$ and even up to 1K around $\nu = 2/5$. The line components change their relative intensities as a function of temperature. The *high–energy* lines are more intense at low temperatures while with the temperature increase the *low–energy* lines gain in intensity.

For the $\nu = 1/3$ we observe one intense and one barely visible peak at energies Es=0.5meV, Es=0.2meV respectively. At 300mK the Es=0.5meV line is of comparable intensity to the second one. At 1K only one line can be distinguished; it might include some trace of the original Es=0.5meV as it is shifted to Es=0.3meV.

The presented temperature dependences are very complicated. Next section will concentrate on the most prominent case of $\nu = 1/3$.

5.3.5 Filling factor $\nu = 1/3$

Simultaneous transport

The apparent symmetry of the $\nu = 1/2$ family of composite fermions that is reflected in the photoluminescence experiment provoked the need for a simultaneous transport measurements to prove that the features are really due to the fractional states of the 2DEG. Additionally, the transport experiments shed light on the correspondence between the transport Hall plateaus and the high energy emission region in the photoluminescence.

Because of the dependence of transport properties on illumination described earlier (Sec. 4.1.3, p. 42), simultaneous transport and data measurements were performed under extremely low powers of below bandgap illumination.

The result of the measurement is presented in 5.16. The photoluminescence spectra were smoothed to eliminate some noise and ease the presentation. On top of the PL spectra transport data are plotted in the same

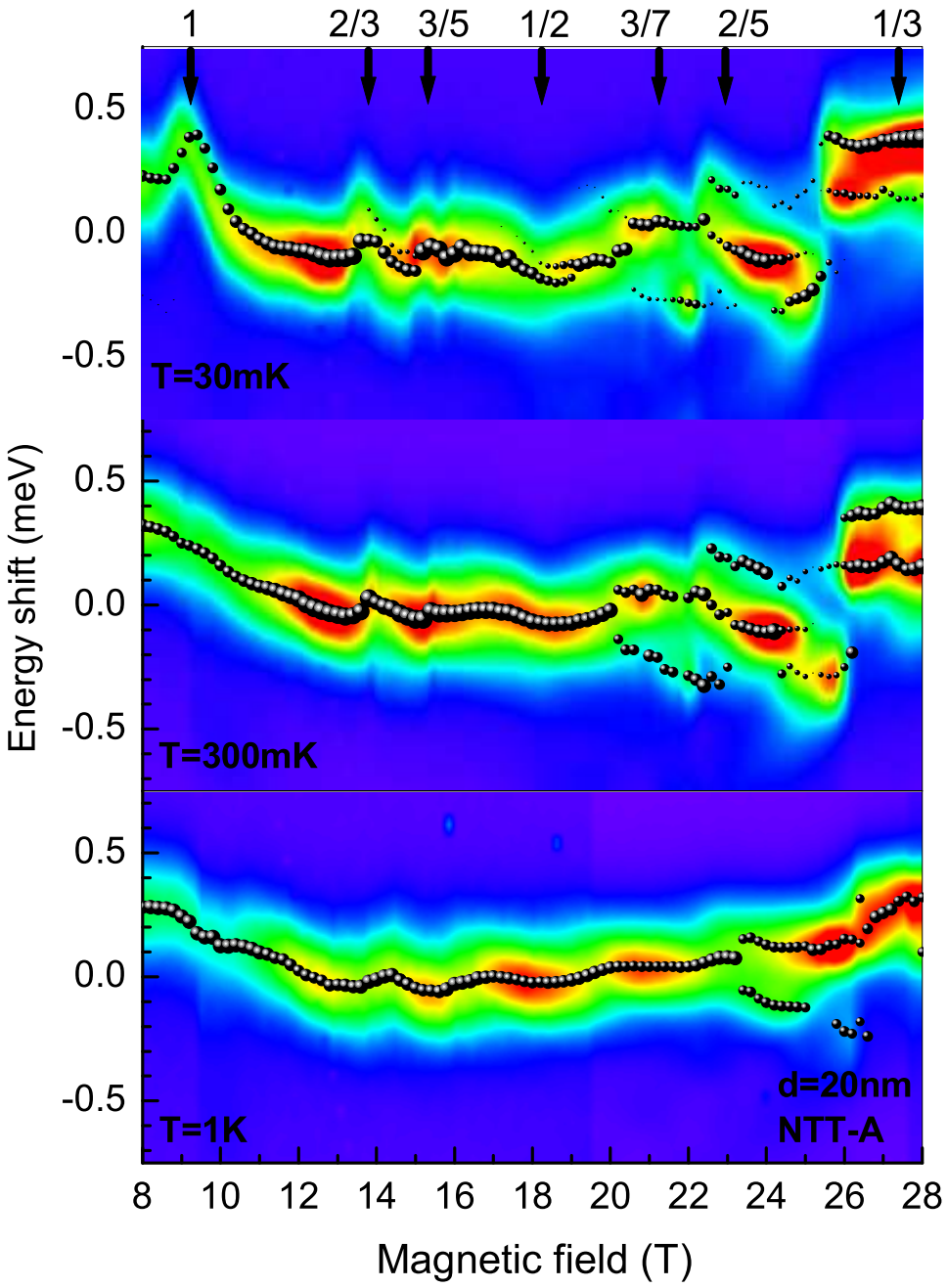

Figure 5.15: *Temperature dependence of NTT-A photoluminescence. Intensity map of the magneto–PL of the NTT-A sample.*

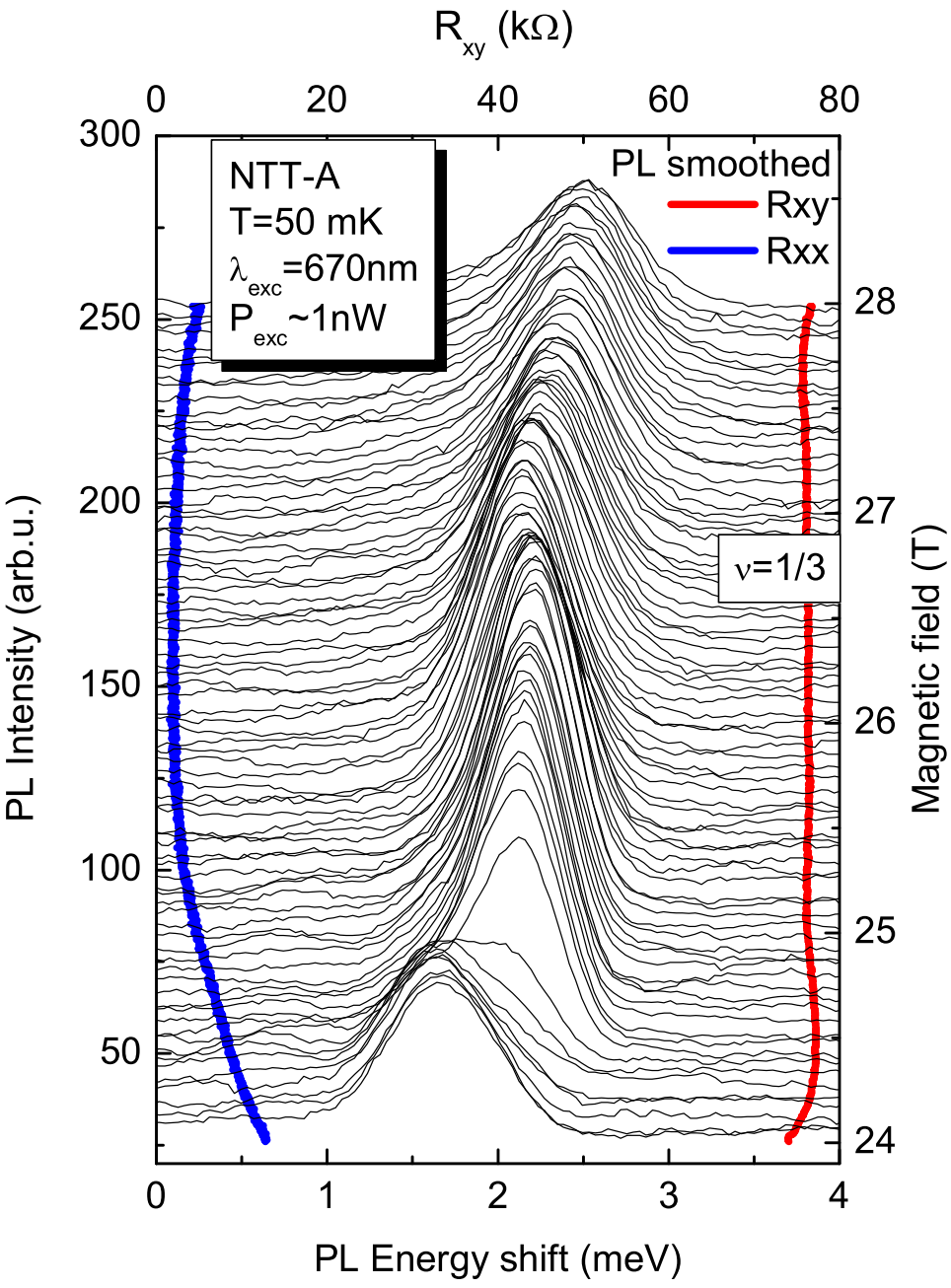

Figure 5.16: *Simultaneous transport and photoluminescence measurements in the vicinity of $\nu = 1/3$. Plateau in R_{xy} corresponds to the region of high emission energy. T=30mK. Excitation: 670nm, P=1nW*

magnetic field scale. A R_{xx} (blue) minimum with a corresponding Hall plateau (red) is visible. The change in the emission energy corresponds to the edge of the Hall plateau and, similarly, the emission energy is constant during the whole Hall plateau between 24.5T and 28T .

The emission is constant because when the system is in an incompressible state (Hall plateau) no quasi–particles exist that can screen the hole and create an excitonic complex. The ground state is a multiplicative state and its emission energy is higher than that of an excitonic complex.

5.3.6 Theoretical interpretation at $\nu = 1/3$

A qualitative interpretation of experimental results requires a profound theoretical modelling which takes into account the actual sample parameters. So far, such calculations are not available for all fractional quantum Hall states observed in the experiments. Nevertheless, they have been carried out by P. Hawrylak [29] for the case of the most pronounced $\nu = 1/3$ state. These calculations are sketched below and compared to the experimental observations.

Temperature dependence

The recombination processes expected in the case when the 2DEG is exactly at filling factor $\nu = 1/3$ are shown in Figure 5.17. The top panel represents the energy spectrum of the initial state and the bottom panel the energy spectrum of the final state.

The *initial state* spectrum reflects the spectrum of a 2DEG at filling factor $\nu = 1/3$ with an additional electron–hole pair (exciton). The final state spectrum is a pure spectrum of the $\nu = 1/3$ fractional quantum Hall state (note a characteristic lowering of the excited states around $L \sim 3-4$), known in literature as the *magnetoroton* minimum.

In the first approximation, optical transitions occur between states with the same angular momentum. Possible transitions with the most pronounced oscillator strength are marked by vertical arrows. In the initial state the lowest energy level has $L = 0$ angular momentum, and it can recombine to the $L = 0$ ground level of the final state. This transition is marked by a red arrow and should be the only optical transition observed at low temperatures, assuming full thermalisation, i.e. only the lowest energy level is occupied in the initial state.

Following a deeper theoretical analysis, this $L = 0$ initial state should be recognised as a so–called *multiplicative* excitonic state, which resembles the neutral exciton. Such a state is insensitive to the surrounding electron gas.

The low temperature photoluminescence spectrum of a 2DEG at $\nu = 1/3$ is therefore expected to be unaffected by the electron – electron interactions.

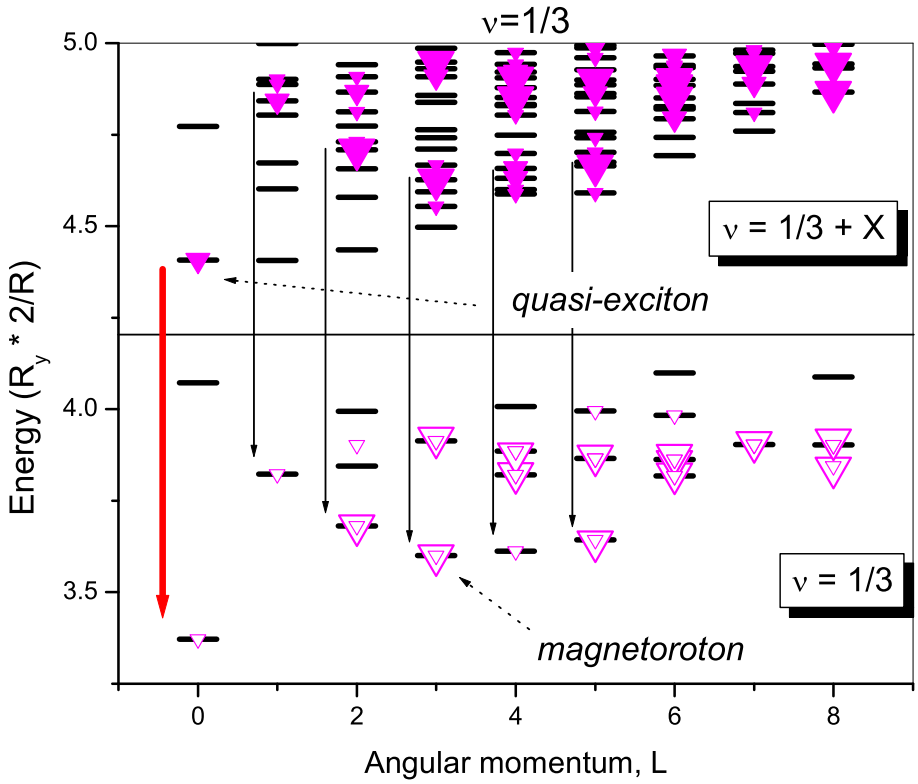

Figure 5.17: *Calculated energy spectrum of initial and final states at* $\nu = 1/3$. *Allowed transitions marked by vertical arrows. Oscillator strengths are represented by magenta triangles. Arrows represent the* $\Delta L = 0$ *transitions. Red arrow represents the transition favoured at low temperatures.* R_y *is the effective Rydberg constant,* R *is the radius of the Haldane sphere.*

The electron – electron interactions might be however visible at higher temperatures when the initial states with higher angular momentum become populated and possibly recombine with characteristic collective modes (around the magnetoroton minimum) of the $\nu = 1/3$ fractional quantum Hall state. Due to the characteristic difference in the initial and final state energy spectrum, the emission related to higher angular momentum states should occur on the low energy side of the $L = 0 \rightarrow L = 0$ transition. These theoretical expectations are illustrated in Figure 5.18.

Experiment seems to confirm these considerations. As shown in Figure 5.19 the emission spectrum in the close vicinity of $\nu = 1/3$ is seen to be composed of two lines. The higher energy line dominates the spectrum at $30mK$ whereas the low energy component activates at $300mK$. Further increase of temperature leads to more complex spectra evolution but this is to be expected as the energy spectra of the initial and final states are also very

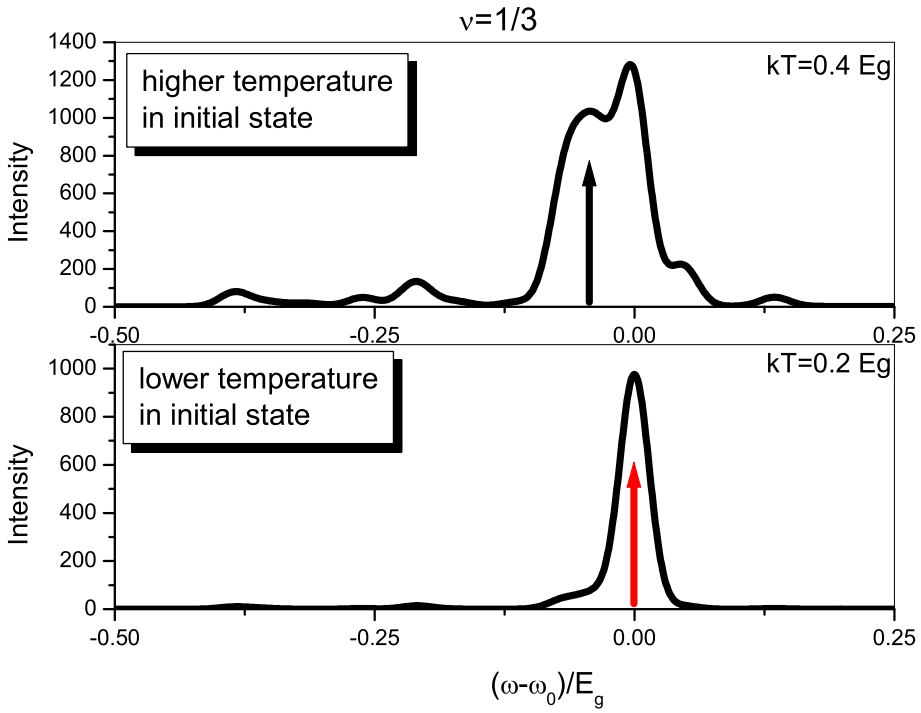

Figure 5.18: *Calculated emission spectra at $\nu = {}^1/_3$ for two different temperatures. The red and black arrows represent the favoured transition in low temperatures and transition from higher angular momentum states, respectively.*

probably temperature dependent. Thus, a comparison of the experiment and the theory can be made only at relatively low temperatures.

Hall plateau equivalent

The effects discussed above are believed to be characteristic for the photoluminescence spectra measured in the range of magnetic fields which corresponds to the region of the plateau in the Hall voltage. This can be deduced from previously shown data (Fig. 5.16, p. 98) of simultaneous optical and transport measurements.

As can be seen in Figure 5.19, more dramatic changes in the photoluminescence spectra than those described above, are observed at lower magnetic fields, once one expects to cross the edge of the quantum Hall plateau. Characteristically, this abrupt change in the luminescence spectra is pushed towards higher fields when the sample temperature is higher. This effect is likely associated with the temperature narrowing of the quantum Hall plateau.

It is therefore logical to think that this abrupt change in the photoluminescence is associated with the appearance of quasi–particles, naturally

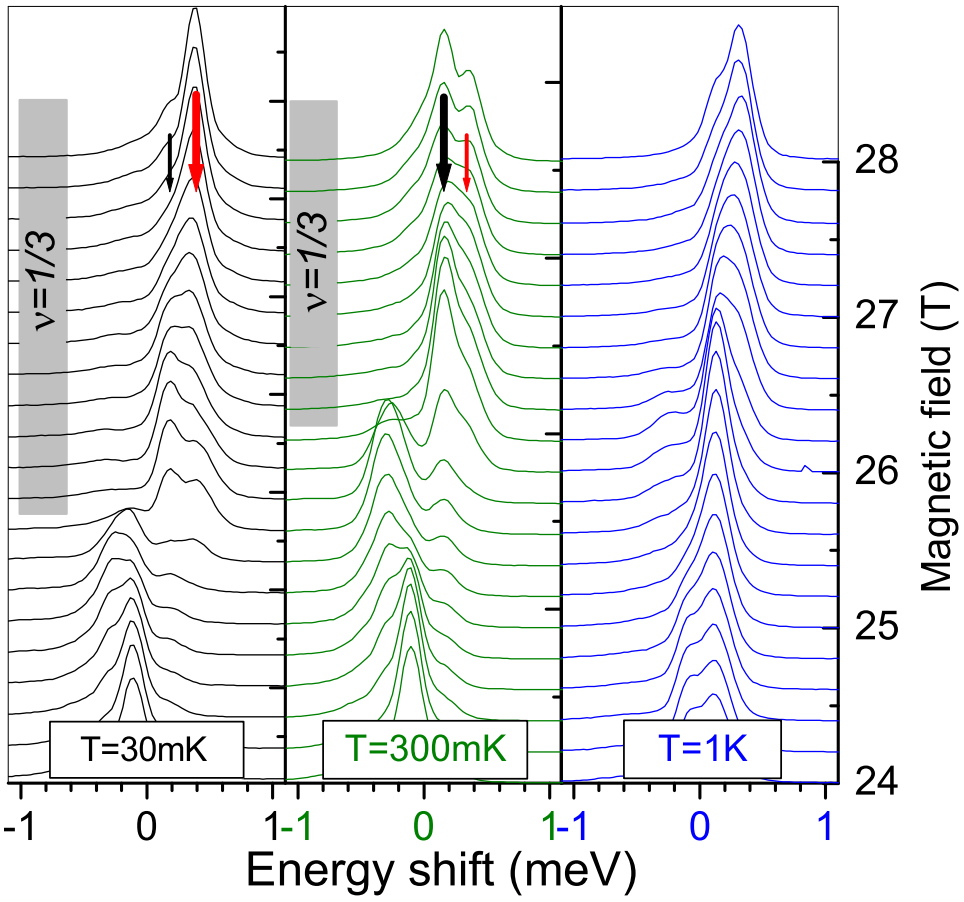

Figure 5.19: *Temperature dependence of 2DEG emission around $\nu = 1/3$ from the NTT-A sample. Grey rectangles mark the positions of a $\nu = 1/3$ Hall plateau. At 300mK, the width of the plateau decreased. Additionally the ratio of intensity of the PL lines at the plateau was inverted.*

expected upon crossing the edge of the $\nu = 1/3$ quantum Hall plateau. These are the quasi electrons with $1/3$e fractional charge that appear on the low field side of the $\nu = 1/3$ state.

To account for the experimental observation, the theoretical calculations have been also performed for the case of $\nu > 1/3$. Again the energy spectrum of the initial and final states has been calculated (Figure 5.20). However, this time the initial state reflects the collective state which could be viewed as being composed of the 2DEG in the $\nu = 1/3$ state with an additional electron-hole pair (exciton) and one quasi–electron.

The final state, after recombination, reflects the 2DEG in the $\nu = 1/3$ state with an additional quasi–electron. Again, the lowest energy level of the initial state is at $L = 0$ but now it has a relatively smaller oscillator

strength, and its character is completely different.

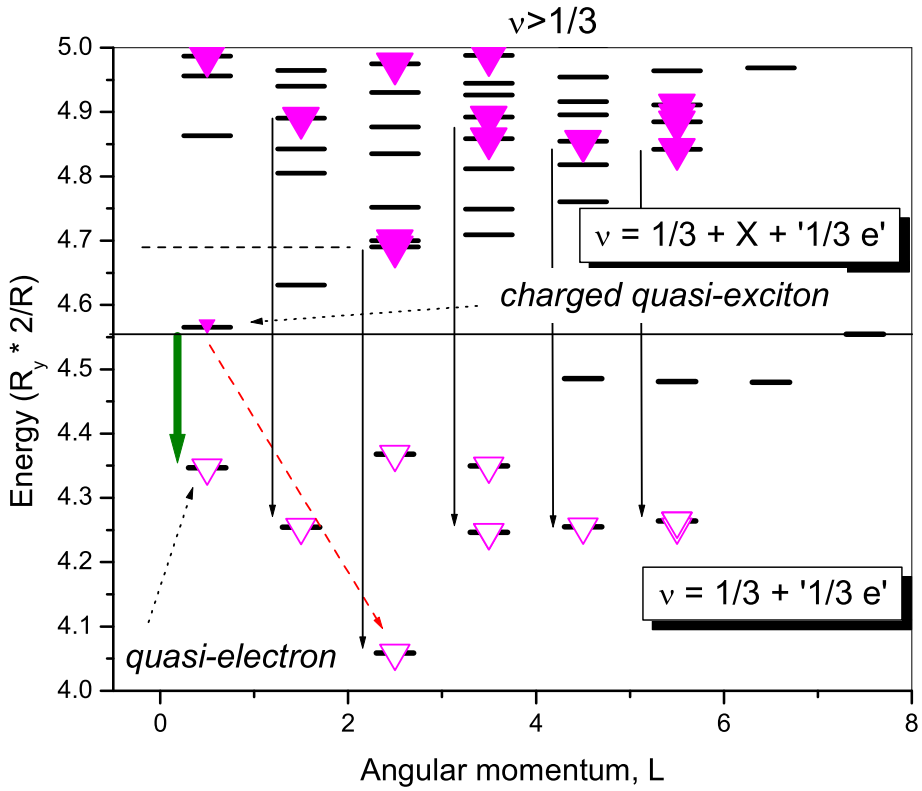

Figure 5.20: *Calculated energy spectrum of the initial and final states at* $\nu > {}^1\!/_3$. *Allowed transitions are marked by vertical arrows. Oscillator strengths are represented by magenta triangles. The green arrow represent the recombination of a* quasi–exciton.

Theoretical analysis shows that ,in a naïve picture, this state can be viewed as a complex that represents a valence band hole which binds ${}^4\!/_3$ of an electron charge. In some sense it is intuitively clear that the existence of quasi–electrons with ${}^1\!/_3$ charge should imply that the neutral exciton could accumulate additional charge and form an object that resembles a negatively charged exciton but with a surplus charge of ${}^1\!/_3$e.

Theoretical calculations show that such a state has lower energy and its binding energy with respect to the neutral *quasi–exciton* is of the order of $0.5meV$ in our sample. The transition marked by a green arrow in Figure 5.20 should be identified with the *quasi–exciton* recombination. This transition is clearly of lower energy and may dominate the spectra at high temperatures, which is in general agreement with the experimental observations.

The abrupt *redshift* of the photoluminescence spectra on the low field

side of the $\nu = 1/3$ state could be explained by the transition of the photoluminescence spectrum from the neutral *quasi–exciton*–like (characteristic for the $\nu = 1/3$ state in the absence of quasi–particles) to the *fractionally charged exciton* – like (in the presence of quasi–particles). The comparison of theoretical calculations with experiment is presented in Figure 5.21.

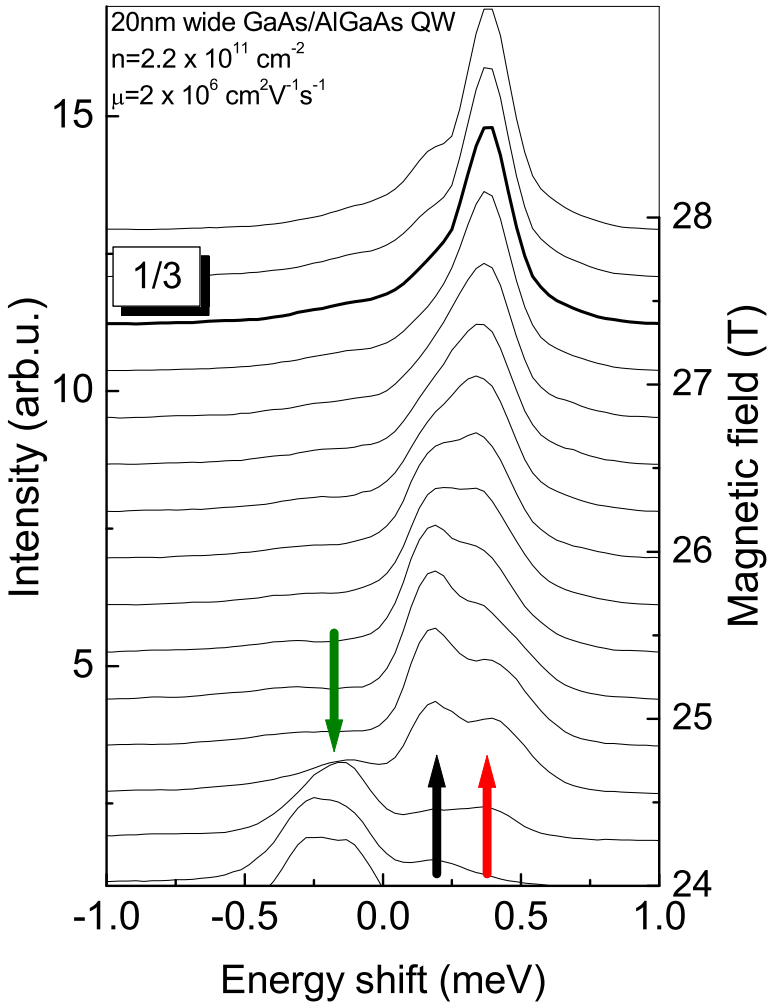

Figure 5.21: *Photoluminescence spectra around $\nu = 1/3$. Theoretical interpretation is marked by arrows. Red and black arrows: Emission at $\nu = 1/3$ between ground states and excited states, respectively (Fig. 5.17). Green arrow: lower energy emission at $\nu \geq 1/3$ from ground state to higher state at low k (Fig. 5.20).*

5.4 Resonant excitation and Raman scattering

The optical studies presented in this work so far have implied the use of excitation far above the characteristic emission energies. Additional information can be obtained from experiments in which the energy of the exciting light is tuned in the close vicinity of the emission band. This technique is in general referred to as *resonant excitation* spectroscopy and includes techniques such as photoluminescence excitation or resonant inelastic light scattering. The latter method is of particular interest with respect to studies of fractional quantum Hall effect as it allows to probe the excitation spectrum of the 2DEG. Such an excitation spectrum has a characteristic features for each fractional quantum Hall state and is a fingerprint of the specific character of electron–electron interactions.

The most representative results of the inelastic light scattering studies of a 2DEG in fractional quantum Hall regime are those allowing to measure the characteristic points (e.g. at the magnetoroton minimum) of the excitation spectrum of the $\nu = {}^1\!/_3$ state [24].

In this chapter, an approach to the application of resonant excitation spectroscopy to study the 2DEG in the fractional quantum Hall regime in magnetic fields up to 28T is presented.

Although the final results are not fully conclusive, the feasibility of such experiments is clearly demonstrated. In particular, inelastic light scattering signals possibly reflecting the composite fermion image of the fractional quantum Hall effect have been identified.

A resonant excitation technique implies much more experimental effort than non–resonant photoluminescence measurements. Special precautions have to be taken to efficiently reduce the laser light entering the spectrometer. This was achieved by using a specially arranged two–fibre system. With this set–up we could continuously detect the signal with the CCD camera, simultaneously sweeping the laser energy through the detection window. Thus, it was possible to measure the laser line, the emission and the scattered signal at the same time.

The most serious problem related to resonant excitation techniques is the need to use generally high excitation powers (because of low collection efficiency), which results in rather poor control of the sample parameters (electron concentration). This inconvenience is particularly difficult to overcome as the investigated samples are very sensitive to the number of injected valence–band holes and the absorption spectrum of the 2DEG may change dramatically.

5.4.1 Preliminary studies

The studies reported in this chapter have been performed on the NTT-A sample which seems to be robust even under resonant excitation conditions.

Nevertheless, this sample behaves quite differently under resonant excitation as compared to its characteristics under non–resonant excitation.

Photoluminescence. Figure 5.22 presents the results of the characterisation of the NTT-A sample under resonant excitation. Full circles represent the familiar Landau level fan chart of the photoluminescence transitions under resonant excitation of $E_{exc} = 1.545eV$, only tenths of a meV above the ground state emission.

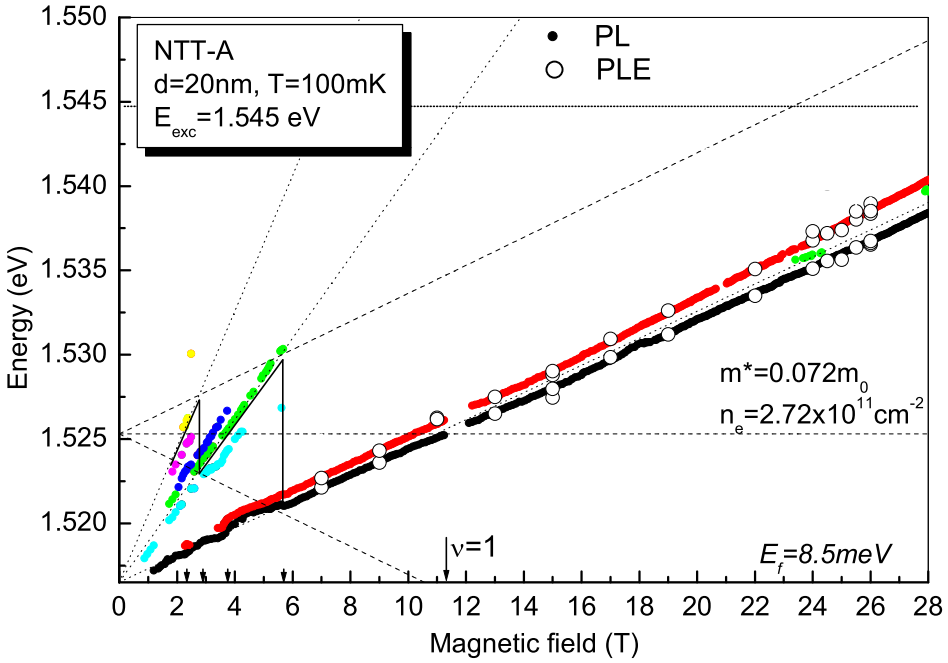

Figure 5.22: *Photoluminescence and photoluminescence – excitation transition energies in the NTT-A sample under resonant excitation. Determined parameters of the 2DEG are indicated.*

The estimated 2DEG concentration is

$$n_e \quad = \quad 2.72\,10^{11} cm^{-2} \tag{5.6}$$

and clearly has increased considerably as compared to the previous illumination conditions (see Table 4.1, p. 53) . The slope of the transitions is also different, leading to a higher estimated value of the reduced effective mass of:

$$m_r^* \quad = \quad 0.072\,m_0 \tag{5.7}$$

The signatures of the fractional quantum Hall effect are much less pronounced, though still visible if the data are inspected more closely. The

washing out of the fractional quantum Hall effect signatures is likely due to the appreciably higher laser power used in the resonant excitation experiments. A very detailed analysis of the present photoluminescence data is difficult and probably meaningless as the absorption strength at the energy corresponding to the used laser excitation varies with magnetic field.

Photoluminescence excitation. Open circles in Figure 5.22 represent the two spin–split main absorption peaks that have been extracted from a PLE–type analysis. It is worth noting that both spin components of the ground state are well visible in the photoluminescence excitation experiments in the entire range when $\nu \leq 2$, except a small region around filling factor $\nu = 1$.

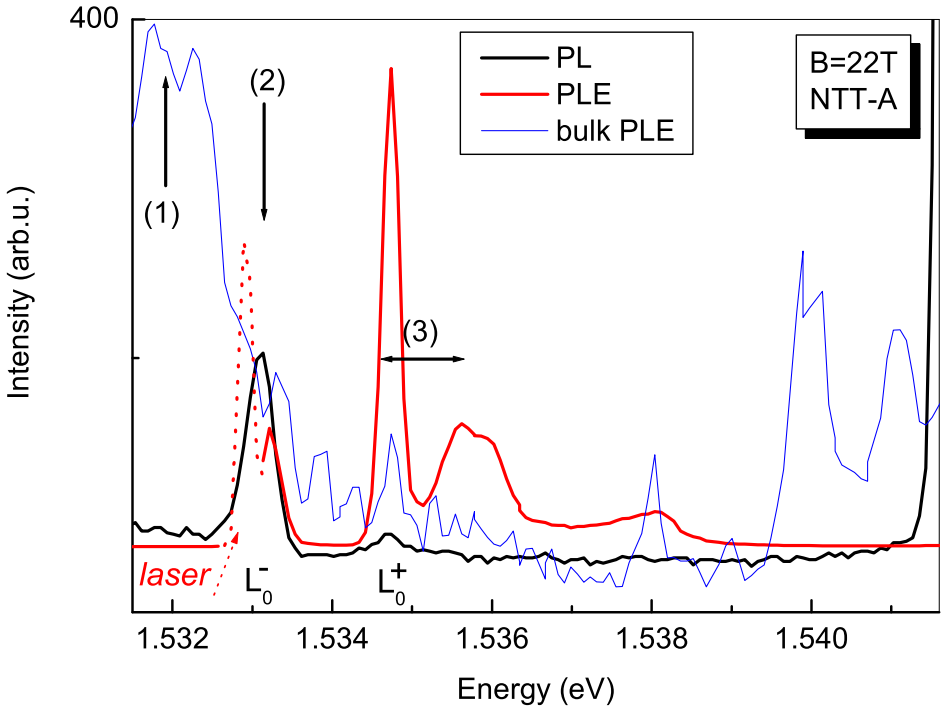

Figure 5.23: *PL (black) and PLE (red) spectra of the 2DEG at B=22T. The bulk PLE spectrum at 22T is marked in blue. Excitation energies where resonant Raman scattering signals are observed are marked with arrows. T=100mK. The sample is NTT-A.*

This seems to be a surprising feature but has also been observed by others [30, 31, 32] and indicates that the electron spin polarisation can not be correctly described by a simple one-electron model but likely requires the introduction of a *skyrmionic* ground state.

Neglecting this subtle effect one can appreciate the high quality of the

sample since the main photoluminescence and photoluminescence excitation peaks almost coincide with each other and no "Stokes" shift is observed.

Representative PLE spectra measured at B=22T are compared with a corresponding photoluminescence spectrum in Figure 5.23.

The black trace represents the 2DEG emission under resonant excitation. The lowest Landau level emission is clearly visible with a trace of the emission from the higher spin state of the lowest Landau level (marked as L_0^- and L_0^+, respectively). The blue trace represents a PLE spectrum of the bulk GaAs emission. The red trace represents a PLE spectrum of the 2DEG. The absorption to the partially empty lowest Landau level (L_0^-) is visible close to the detected laser line (marked by dashed red line). The absorption to the completely empty high energy spin state is visible as the most pronounced peak in the spectrum. An additional absorption probably connected with light hole states is visible at higher energies.

5.4.2 Inelastic light scattering

Once we have done the preliminary characterisation of the samples we now focus on the inelastic light scattering experiments. The difficulty in identification of the signal lies in its resonant nature. The resonant Raman signal is overlapped with the luminescence signal. Additionally, an observed Raman signal may originate not only from the 2DEG but also from other parts of the sample.

The inelastic light scattering measurements were performed in magnetic fields between 15 and 26T what covers the filling factor range $0.4 \leq \nu \leq 0.7$ in the sample ($n_e = 2.72 \cdot 10^{11} cm^{-2}$).

Several Raman scattering signals have been found in the experiments. Three different types of transitions named (1), (2) and (3) will be discussed further.

Those transitions clearly resonate with well defined peaks observed in the PLE experiment (Figure 5.23). The signal (1) is attributed to the bulk material whereas signals (2) and (3) are likely due to the 2DEG. This attribution is based on an inspection of the conditions under which these signals are observed.

Bulk electron spin–flip. The signal (1) is clearly observed only when the excitation energy is tuned in the vicinity of the bulk GaAs exciton transition. The arrow–(1) in Figure 5.23 indicates the energy of the laser excitation which is preferential for clear observation of the type–(1) transition.

The excitation energy corresponding to type–(1) signals varies with magnetic field. The field dependence reflects well the electron Zeeman energy ($0.44\mu_B B$, see Figure 5.27) and this transition is therefore attributed to the electron spin–flip process in bulk GaAs. Examples of Raman scattering

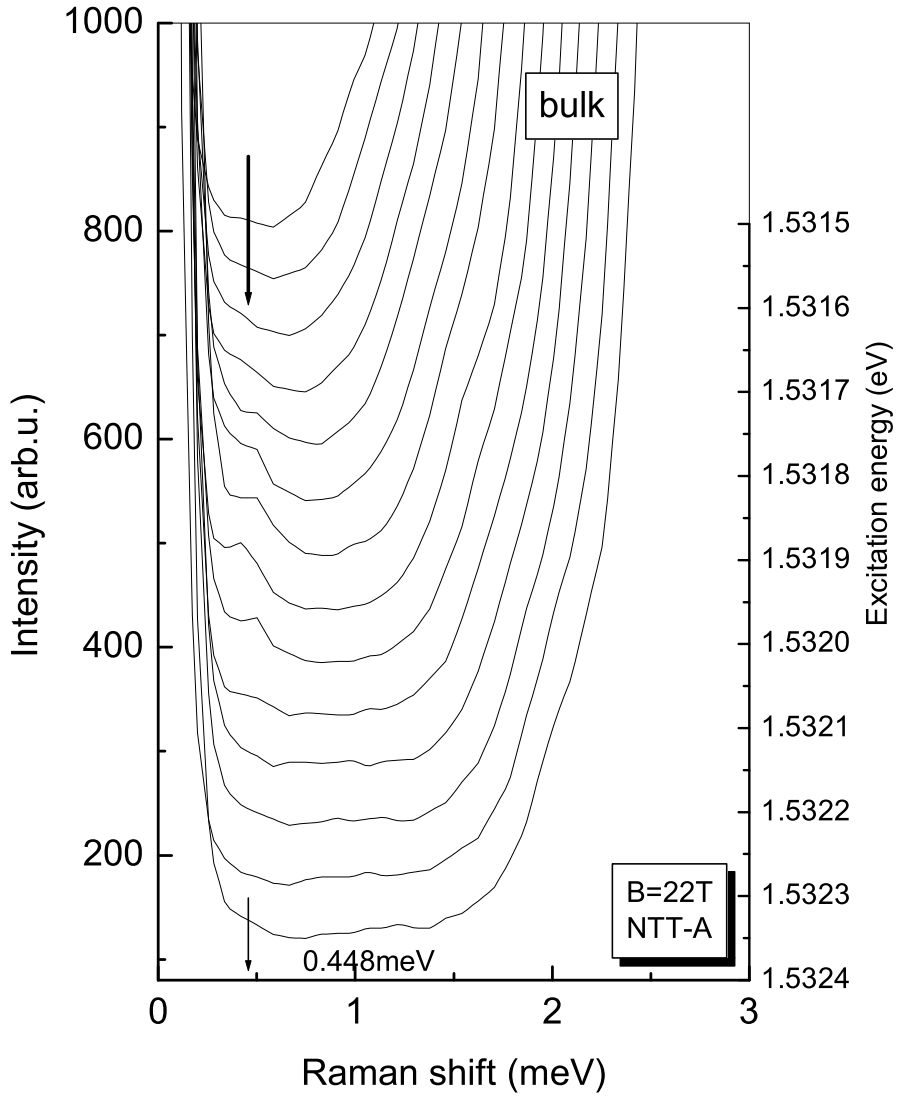

Figure 5.24: *Resonant inelastic light scattering spectra of the spin–flip process in bulk GaAs at B=22T. Bath temperature is* $T \sim 100mK$. *The sample is NTT-A, d=20nm.*

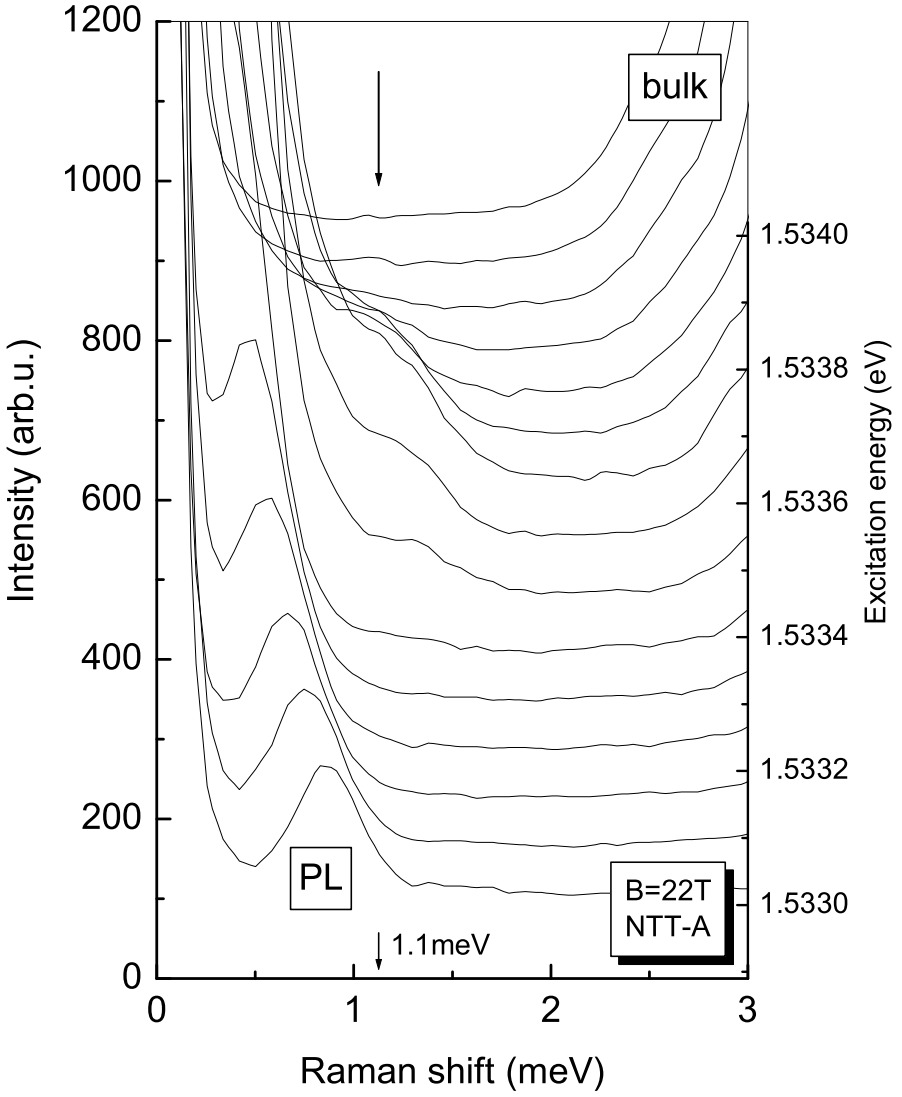

Figure 5.25: *Raman scattering to the CF "Fermi energy". Bath temperature is* $T \sim 100mK$. *The sample is NTT-A, d=20nm.*

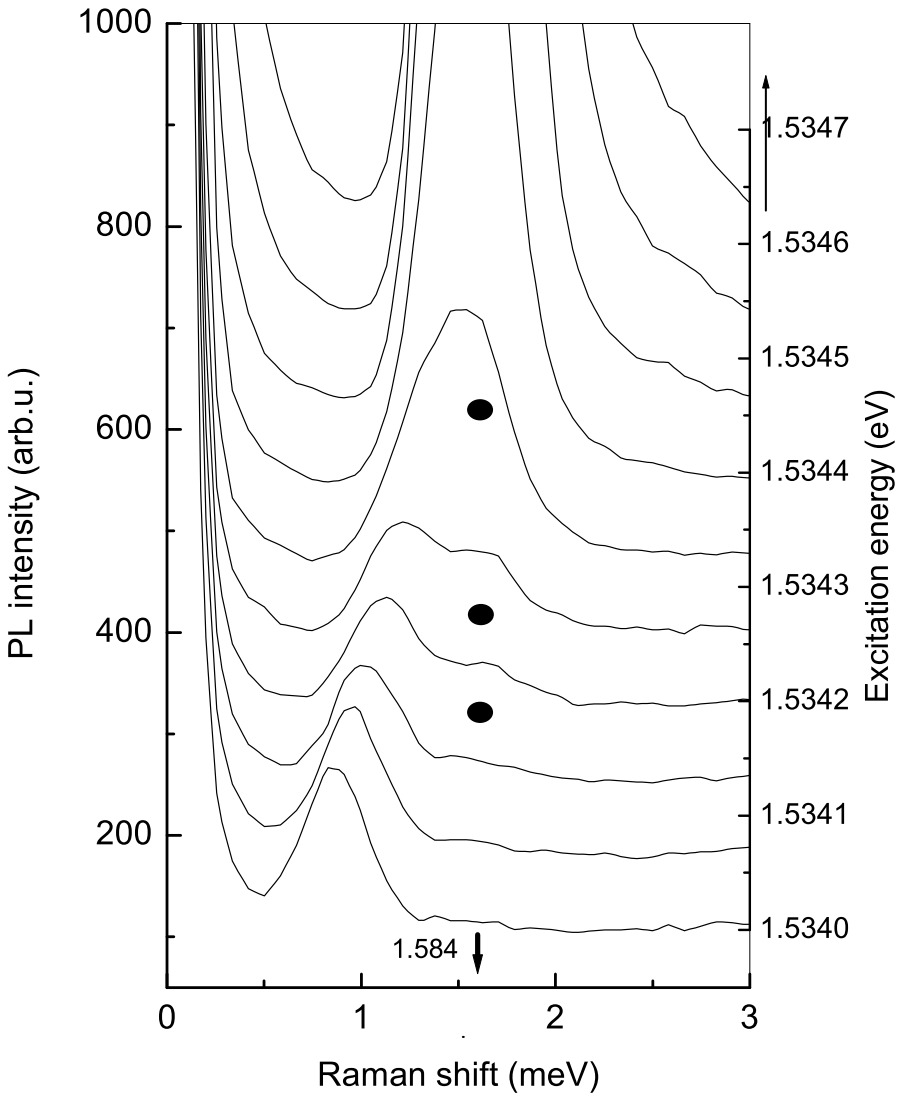

Figure 5.26: *Resonant inelastic light scattering spectra of the spin–flip process in the 2DEG at B=22T. Bath temperature is* $T \sim 100mK$. *The sample is NTT-A, d=20nm.*

spectra in field $B = 22T$ corresponding to type–(1) transition are presented in Figure 5.24.

Excitation to the Fermi level. The second type of Raman signal is most clearly observed when the laser energy coincides with the lowest energy of the 2DEG transition.

The excitation energy favourable to the observation of the type–(2) Raman signal is marked by arrow–(2) in Figure 5.23. The excitation energy of this type–(2) Raman signal does not depend on the magnetic field and is plotted in Figure 5.27 as light blue circles.

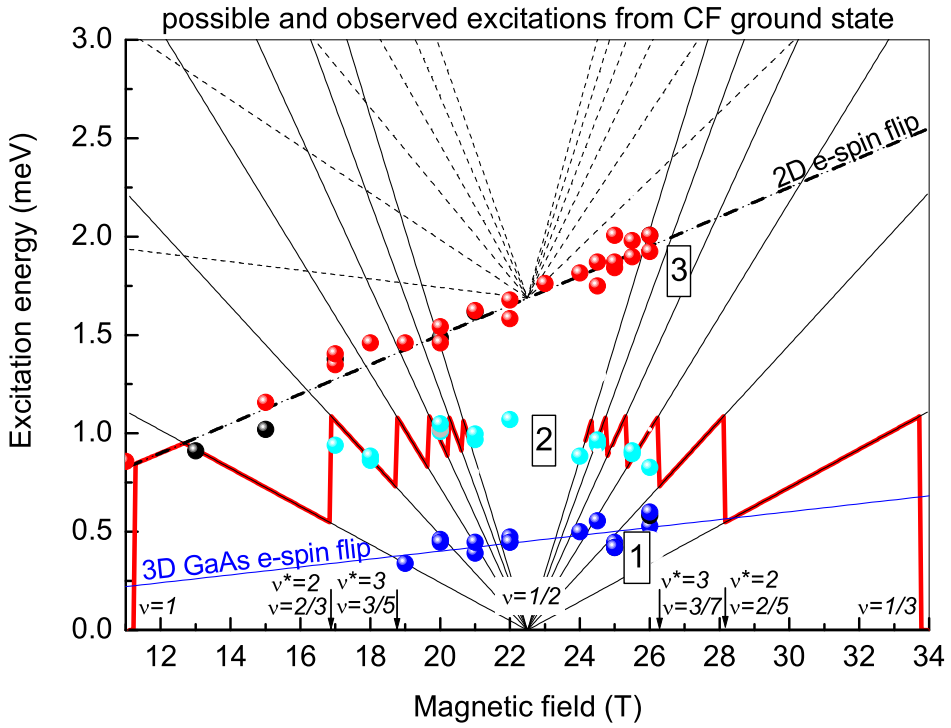

Figure 5.27: *Magnetic field dependence of the observed Raman scattering signals (circles) plotted on top of possible excitations from the ground state in the composite fermions picture. The sample is NTT-A quantum well* ($n_e = 2.72 \cdot 10^{11} cm^{-2}$). *The effective mass of composite fermions is* $m_{CF} = 4 \cdot 0.079 \cdot \sqrt{B_{\nu=1/2}} \cdot m_0$; *The energy of the 2D electron – spin flip is* $1.5 g \mu_B B$, $|g| = 0.44$.

The interpretation of its origin can be based on Figure 5.27 where the fan chart of Landau levels of composite fermions is sketched. The zero energy in this representation corresponds to the energy of the ground state of the low spin state. Thus, the levels which originate from the $\nu = {}^1\!/_2$ state, where the effective magnetic field is $B^* = 0$, represent possible excitation energies from the ground state. The figure presents two Zeeman–split families of the

CF -Landau levels. A value of $\pm 1.5 g\mu_B B$ of the Zeeman splitting has been assumed in this figure.

Additionally, oscillations of a "CF–Fermi level" have been plotted in the picture, based on the analogy of fractional filling factors (ν) with the integer filling factors (ν^*) of composite fermions.

The fan chart has been drawn based on the composite fermion effective mass determined by previous [33, 34] measurements:

$$m_{CF} = 4 \cdot 0.079 \cdot \sqrt{B_{\nu=1/2}} \cdot m_0 \tag{5.8}$$

When the energy of the type–(2) scattering is compared with such a picture it seems probable that it reflects the scattering process to the Fermi level. Such an interpretation is in accordance with the conditions under which the signal is observed.

Examples of Raman scattering spectra in field $B = 22T$ corresponding to type–(2) transitions are presented in Figure 5.25.

2DEG spin–flip The third type of the light scattering signal is observed when the laser energy is in the range of absorption to the higher energy spin state (L_0^+) of the 2DEG. This laser energy is marked as arrow–(3) on top of the 2DEG PLE signal in Figure 5.23. The horizontal orientation of the arrow reflects the wide range of excitation energies where the signal can be observed.

Examples of the type–(3) Raman scattering spectra are presented in Figure 5.26.

The magnetic field dependence of the type–(3) Raman signal is presented in Figure 5.27. The linear dependence and the excitation energy in the range of the upper spin level of the lowest Landau level implies that the observed process is a spin flip scattering of a 2D electron.

It is speculated that this signal could be attributed to the electron spin flip in a 2DEG despite the fact that the linear field dependence $1.5 g\mu_B B$ is much higher than the bare electron Zeeman splitting for $g = 0.44$. Nevertheless, a much larger electron spin splitting is required to explain the spin polarisation of the $\nu = 1/2$ family of the fractional quantum Hall states. The spin splitting value of $1.5 g\mu_B B$ seems to account reasonably well for the results of the tilted magnetic field studies of the $\nu = 1/2$ family of the fractional quantum states found in the literature.

5.5 Conclusions

Until recently, the multiplicity of the fractional quantum Hall effect states was visible only in transport experiments. The novel experimental results

presented in this chapter showed that the FQHE states of a 2DEG can also be probed by photoluminescence measurements.

The simultaneous transport and photoluminescence measurements confirmed the observed photoluminescence features to be due to the changing state of the 2DEG.

A characteristic symmetry around $\nu = {}^1\!/_2$ is easily visible in the representative spectra of a $20nm$ quantum well emission. The symmetry can be interpreted in a picture of composite fermion model and has been regularly observed in transport measurements of high quality samples. Features attributed to at least five fractional quantum Hall states have been observed. The observed fractional filling factors include: $\nu = {}^1\!/_3,\ {}^2\!/_5,\ {}^3\!/_7,\ {}^3\!/_5,\ {}^2\!/_3$. In the vicinity of these points, the emission energy has been observed to increase by $\sim 0.5meV$, a shift bigger than the line width.

Temperature dependence measurements showed that measured phenomena are indeed low temperature effects. Secondly, along with theoretical calculations they allowed to assign the doublet observed at $\nu = {}^1\!/_3$ to the ground and excited state emission for the high and low energy component, respectively.

The high energy emission plateau around $\nu = {}^1\!/_3$ has been interpreted as the equivalent of the Hall plateau observed in Hall resistance measurements. The temperature dependence of the photoluminescence shows the emission plateau narrowing with increasing temperature. The emission energy jump at the plateau boundary is attributed to the occurrence of quasi–particles that form charged quasi–excitonic complexes of higher binding energy than the neutral quasi-excitons at $\nu = {}^1\!/_3$.

The photoluminescence from the narrow ($d = 10nm$) sample is classified as being not sensitive to the 2DEG changing states due to much bigger electron – hole interaction than the 2D electron correlation. On the other hand the $d = 50nm$ sample was expected to have an electron – hole interaction even smaller than the representative ($d = 20nm$) NTT-A sample, thus being a more delicate probe of the 2DEG states. The overlap of bulk and 2DEG emission lines hindered the measurements above $\nu = {}^1\!/_2$.

Inelastic light scattering identified two excitations of the 2DEG based on the comparison with the photoluminescence excitation measurements. A spin – flip process and an excitation to the Fermi energy of composite fermions have been identified. Additionally, a bulk GaAs spin–flip process has been observed.

Bibliography

[1] A. J. Turberfield, S. R. Haynes, P. A. Wright, R. A. Ford, R. G. Clark, J. F. Ryan, J. J. Harris, and C. T. Foxon, Phys. Rev. Lett. **65**, 637 (1990).

[2] E. M. Goldys, S. A. Brown, R. B. Dunford, A. G. Davies, R. Newbury, R. G. Clark, P. E. Simmonds, J. J. Harris, and C. T. Foxon, Phys. Rev. B **46**, R7957 (1992).

[3] I. V. Kukushkin and V. B. Timofeev, JETP Lett. **44**, 228 (1986).

[4] I. V. Kukushkin and V. B. Timofeev, Adv. Phys. **45**, 147 (1996).

[5] D. Heiman, B. B. Goldberg, A. Pinczuk, C. W. Tu, A. C. Gossard, and J. H. English, Phys. Rev. Lett. **61**, 605 (1988).

[6] B. B. Goldberg, D. Heiman, A. Pinczuk, L. Pfeiffer, and K. West, Phys. Rev. Lett. **65**, 641 (1990).

[7] B. B. Goldberg, D. Heiman, M. Dahl, A. Pinczuk, L. Pfeiffer, and K. West, Phys. Rev. B **44**, 4006 (1991).

[8] A. J. Shields, M. Pepper, M. Y. Simmons, and D. A. Ritchie, Phys. Rev. B **52**, 7841 (1995).

[9] G. Finkelstein, H. Shtrikman, and I. Bar-Joseph, Phys. Rev. Lett. **74**, 976 (1995).

[10] G. Finkelstein, H. Shtrikman, and I. Bar-Joseph, Phys. Rev. B **53** (1996).

[11] D. Gekhtman, E. Cohen, A. Ron, and L. N. Pfeiffer, Phys. Rev. B **54**, 10320 (1996).

[12] Y. Kim, F. M. Munteanu, C. H. Perry, D. G. Rickel, J. A. Simmons, and J. L. Reno, Phys. Rev. B **61**, 4492 (2000).

[13] E. Rashba and M. D. Struge, Phys. Rev. B **63**, 045305 (2000).

[14] A. H. MacDonald, E. H. Rezayi, and D. Keller, Phys. Rev. Lett. **68**, 1939 (1992).

[15] E. I. Rashba and M. E. Portnoi, Phys. Rev. Lett. **70**, 3315 (1993).

[16] A. Wójs and J. J. Quinn, Phys. Rev. B **63**, 045303 (2000).

[17] A. Wójs and J. J. Quinn, Phys. Rev. B **63**, 045304 (2000).

[18] G. Yusa, H. Shtrikman, and I. Bar-Joseph, Phys. Rev. Lett. **87**, 216402 (2001).

[19] B. M. Ashkinadze, E. Linder, E. Cohen, A. B. Dzyubenko, and L. N. Pfeiffer, Phys. Rev. B **69**, 115303 (2004).

[20] C. Schüller, K.-B. Broocks, P. Schröter, C. Heyn, D. Heitmann, M. Bichler, W. Wegscheider, T. Chakraborty, and V. Apalkov, Phys. Rev. Lett. **91**, 116403 (2003).

[21] M. E. Portnoi and E. I. Rashba, Phys. Rev. B **54**, 13791 (1996).

[22] D. G. W. Parfitt and M. E. Portnoi, cond-mat **0306414** (2003).

[23] D. G. W. Parfitt and M. E. Portnoi, cond-mat **0306441** (2003).

[24] A. Pinczuk, B. S. Dennis, L. N. Pfeiffer, and K. West, Phys. Rev. Lett. **70**, 3983 (1993).

[25] H. D. M. Davies, J. C. Harris, J. F. Ryan, and A. J. Turberfield, Phys. Rev. Lett. **78**, 4095 (1997).

[26] M. Kang, A. Pinczuk, B. S. Dennis, M. A. Eriksson, L. N. Pfeiffer, and K. W. West, Phys. Rev. Lett **84**, 546 (2000).

[27] M. Kang, A. Pinczuk, B. S. Dennis, L. N. Pfeiffer, and K. W. West, Phys. Rev. Lett **86**, 2637 (2001).

[28] H. Stormer, Rev. Mod. Phys. **71**, 875 (1999).

[29] P. Hawrylak (2005), proceedings of Electron-Exciton Interactions in Semiconductor Nanostructures, Bad Honnef.

[30] E. H. Aifer, B. B. Goldberg, and D. A. Broido, Phys. Rev. Lett. **76**, 680 (1996).

[31] T. Portengen, J. R. Chapman, V. Nikos Nicopoulos, and N. F. Johnson, Phys. Rev. B **55**, R7367 (1997).

[32] T. Portengen, J. R. Chapman, V. Nikos Nicopoulos, and N. F. Johnson, Phys. Rev. B **56**, R10052 (1997).

[33] K. Park and J. K. Jain, Phys. Rev. Lett. **80**, 4237 (1998).

[34] I. V. Kukushkin, J. H. Smet, K. von Klitzing, and W. Wegscheider, Nature **415**, 409 (2002).

[35] S. Das Sarma and A. Pinczuk, eds., *Perspectives in quantum Hall effects* (John Wiley & Sons, Inc., New York, 1997).

[36] O. Heinonen, ed., *Composite Fermions* (World Scientific Publishing, Singapore, 1998).

Chapter 6

Properties of a 2DEG under microwave irradiation in magnetic fields

Dans ce chapitre, les études d'un nouvel effet oscillatoire de la résistance induit par l'irradiation des micro-ondes sont présentées. A bas champs magnétiques, sous l'irradiation micro-onde les propriétés de transport s'écartent nettement des oscillations bien connues de Shubnikov - de Haas pour évoluer vers une série d'états de résistance zéro.

La dépendance en transport à la fréquence et à la puissance de micro-ondes est présentée. Un changement de traces en transport des MIROs vers une forme que ressemble à la résonance cyclotron est présenté. La périodicité des oscillations avec la période défini par la fréquence des micro-ondes est aussi présentée.

Les résultats des mesures d'absorption des micro-ondes sont présentés pour deux échantillons avec des mobilités d'électrons différentes. Les échantillons ont les traces en transport différentes, car l'échantillon à haute mobilité montre les MIROs beaucoup plus prononcées. Dans les spectres d'absorption, l'échantillon de la mobilité basse montre qu'une absorption autour de la résonance cyclotron. Par contre, le deuxième échantillon à haute mobilité montre aussi les signaux de l'absorption aux harmoniques de la résonance cyclotron.

L'existence de deux processus d'absorption différents et sépares est inféré depuis les intensités des signaux d'absorption mesurés par absorption directe des micro-ondes. L'absorption non résonante est mieux visible en transport et observée comme les MIROs, qui vraisemblablement ne respectent pas les règles de polarisation. Par contre, l'absorption résonante, mieux observée dans les mesures d'absorption des micro-ondes, probablement suit les règles de polarisation de la résonance cyclotron.

A 2DEG subjected to an external magnetic field exhibits a wide range of fascinating physical effects. The previous chapter presented optical experiments of 2D electron correlations, induced by high magnetic fields, that manifest themselves in the form of an incompressible quantum liquid. The experimental fingerprints of these high field effects are well known in transport experiments as integer and fractional quantum Hall effects.

Very recently a new effect has been discovered in the low magnetic field range. When irradiated with microwaves (MW), the behaviour of 2DEG transport properties deviates strongly from the familiar Shubnikov – de Haas oscillations. The magneto–resistance traces exhibit a series of vanishing resistance states.

6.1 Introduction

6.1.1 Discovery

The first observation of the microwave induced oscillations (MIROs) of the longitudinal resistance (R_{xx}) was reported by Zudov et al. [1] and observed in samples with high mobility 2DEG and at moderately low temperatures $T \sim 1K$. The authors reported a discovery of a novel behaviour of 2DEG, which irradiated by MWs in the range 5 - 100 GHz displays oscillations of the R_{xx} in the low magnetic field regime determined by the MW energy: $\hbar\omega \sim \hbar\omega_c$. The period of the oscillations in $1/B$ scale is determined by the ratio ω/ω_c of the MW frequency ω to the cyclotron frequency $\omega_c = eB/m^*$, where m^* is the effective mass of conduction band electrons in GaAs. The period of the oscillations differs from the Shubnikov–de Haas oscillations (SdH) whose period is determined by the ratio $E_f/\hbar\omega_c$.

As reported by Mani et al. [2], under strong MW irradiation the R_{xx} minima correspond to *zero resistance states* in samples with sufficiently high mobility 2DEG.

The changes in the longitudinal resistance reported in Refs. [1, 2] were not accompanied by the observation of analogous oscillations in the Hall resistance. Recently, Studenikin et al. [3] confirmed the existence of the MIROs and reported simultaneous changes in the Hall resistance. Relative changes $\Delta R_{xy}/R_{xy}$ were reported to have opposite sign than the sign of ΔR_{xx} i.e. a decrease (increase) in the longitudinal resistance is accompanied by an increase (decrease) in the transversal resistance. The measured amplitude of the ΔR_{xy} changes is only two times weaker than the amplitude of ΔR_{xx}. Subsequent reports [4] confirmed changes in the Hall resistance with no changes of R_{xy} observed in regions of zero resistance states.

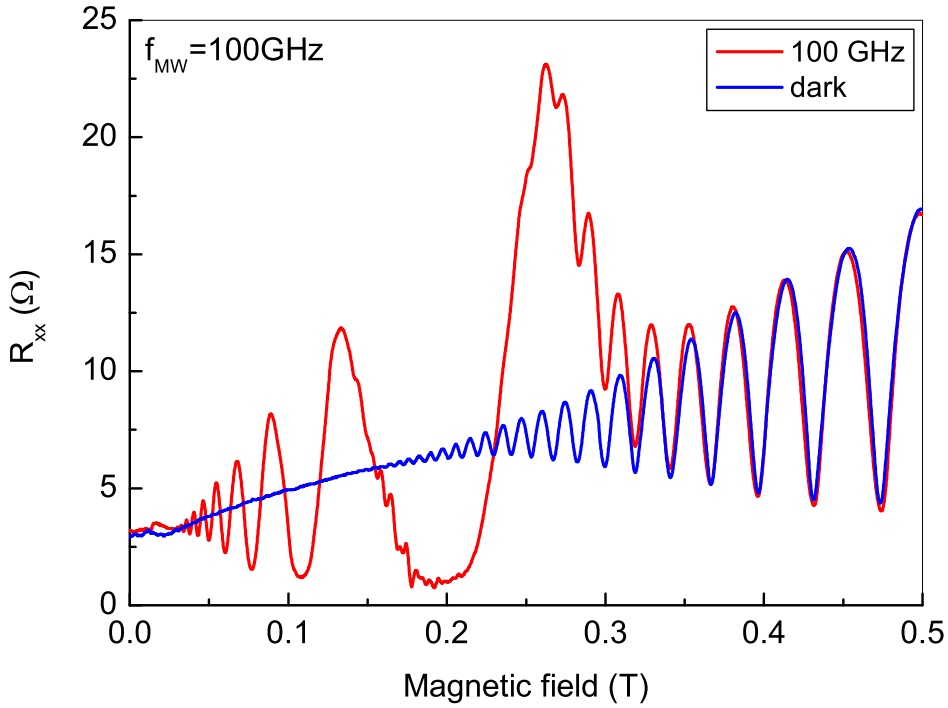

Figure 6.1: *Typical longitudinal resistance trace with (red) and without (blue) microwave irradiation. The microwaves frequency is* $100GHz$*. The MIROs are visible on the lower field part of the red plot apart from the SdH oscillations visible also on the "dark" curve. Bath temperature is 2K. Sample is "Bell" heterojunction.*

6.1.2 Typical data

Figure 6.1 presents typical R_{xx} traces of a high mobility 2DEG in a GaAs/AlGaAs heterojunction ("Bell" sample). The electron concentration and the mobility are presented in Table 6.1. The blue curve ("dark") corresponds to the measurement without MW irradiation. In that case, the only oscillations visible are the SdH oscillations which appear around $B \approx 0.2T$.

name	μ (cm^2/Vs)	n_e (cm^{-2})
Bell	$10 \cdot 10^6$	$2 \cdot 10^{11}$

Table 6.1: *Parameters (mobility and concentration) of the 2DEG in the heterojunction "Bell" sample. Parameters after brief illumination by a red LED at 2K.*

Under a continuous microwave irradiation the magneto–resistance changes. The most pronounced MIRO starts to appear around the cyclotron resonance and lower intensity oscillations are visible on the low magnetic field

side. Above resonance the trace returns to the non–irradiated curve displaying the SdH oscillations. The resistance does not reach zero in the plot presented in Fig. 6.1 because the MW power was not high enough for the mobility of this particular 2DEG (see below).

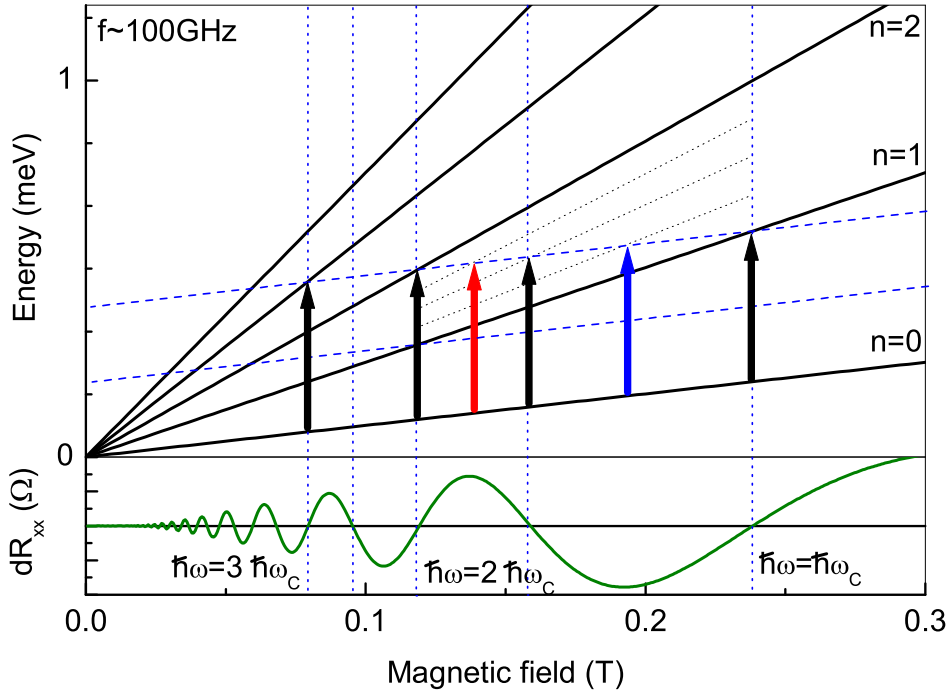

Figure 6.2: *Top. Schematic picture of the microwave cyclotron resonance absorption with several harmonics (represented by black arrows). Bottom. Simulated changes in the R_{xx}. No change is observed when $\hbar\omega = n\hbar\omega_c$. $\Delta R_{xx} > 0$ when $\omega/\omega_c \in (n, n-1/2)$ (red arrow). $\Delta R_{xx} < 0$ when $\omega/\omega_c \in (n+1/2, n)$ (blue arrow). Additionally, no change is observed in R_{xx} when $\omega/\omega_c \approx n \pm 1/2$.*

The resistance oscillations due to the MW irradiation are governed by the ω/ω_c ratio. Figure 6.2 schematically presents the ranges of magnetic field where the observed changes of R_{xx} are positive or negative. The upper part of the figure presents the Landau quantisation of the density of states in a GaAs heterostructure ($m^* = 0.067m_0$). Arrows represent a 100GHz MW irradiation energy. Black arrows correspond to the cyclotron resonance at $B = 0.24T$ and its harmonics. At those values of the magnetic field, when $\omega/\omega_c = n$, where $n = 1, 2 \ldots$, no change in R_{xx} is observed (i.e. $\Delta R_{xx} = 0$). When $\omega/\omega_c \in (n+1/2, n)$, an example marked by a blue arrow, the change in R_{xx} is negative. The opposite case, when $\omega/\omega_c \in (n, n-1/2)$ the change is positive and an example is marked by a red arrow. Apparently, in the case of $\omega/\omega_c = n \pm 1/2$, outside the resonance and in between the two intervals the resistance is also unchanged.

The experimentally determined changes in the magneto–resistance can be simulated (Fig. 6.2, bottom) by the formula:

$$\Delta R_{xx} \quad = \quad -Aexp(-D_M/\hbar\omega_c)sin(2\pi\omega/\omega_c) \tag{6.1}$$

where D_M is an experimentally determined damping parameter (see also Eq. 6.13).

Experimental parameters

Figure 6.1, above, shows the changes in the resistance traces due to the MW irradiation for an arbitrarily chosen set of parameters. It has been established that the magnitude of the effect depends on parameters such as microwave power, frequency, temperature and 2DEG mobility. The influence of power and frequency on the phenomenon will now be discussed.

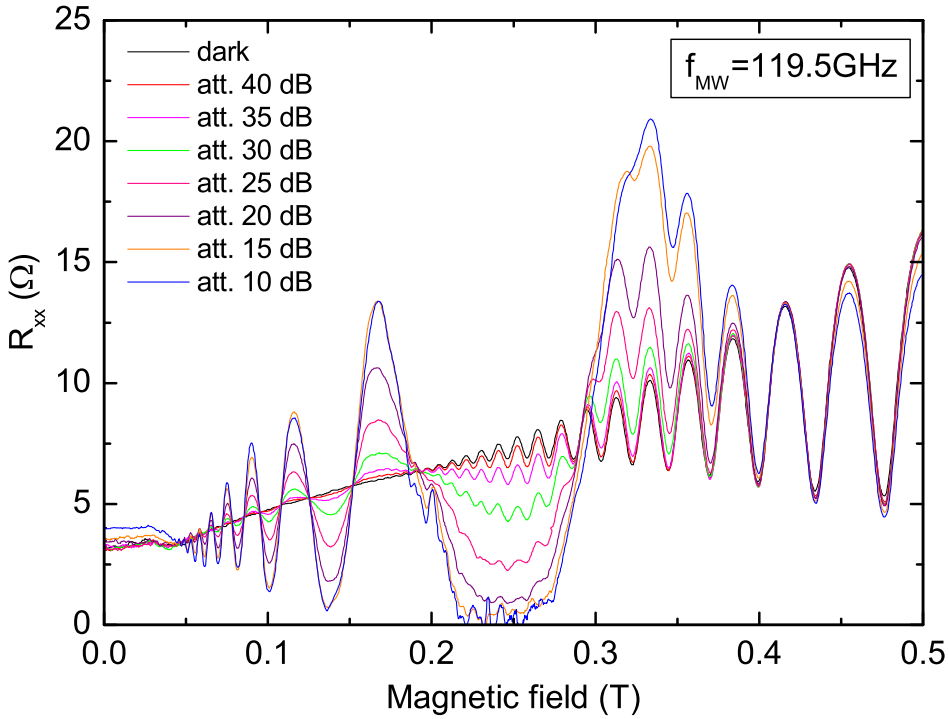

Figure 6.3: *Power dependence of the MIROs. The low power region. Maximum power at 0dB attenuation is 50mW. Microwaves frequency is f=119.5GHz. Sample is "Bell". See also Fig. 6.4.*

Microwave power

The dependence on the MW irradiation power is presented in Figures 6.3–6.4. The MW frequency is $119.5GHz$ from a backward wave oscillator source and the maximum output power is 50mW in the case of $0dB$ attenuation. The dark curve present the SdH oscillations in the case of no MW illumination. When the microwaves are switched on, in the case of the $40dB$ attenuation, the traces starts to show a slight decrease in the resistivity below the cyclotron resonance ($B_{res} = 0.29T$). When the power is gradually increased, oscillations start to be visible around harmonics of the cyclotron resonance. For $10dB$ attenuation the strongest minimum below resonance reaches zero resistance. For even higher microwave powers (Figure 6.4), the first minimum stays at zero, while features around other harmonics become more pronounced and would eventually reach zero. The traces at the highest powers show the heating of the 2DEG by the microwaves visible as the thermal blurring of the SdH oscillations.

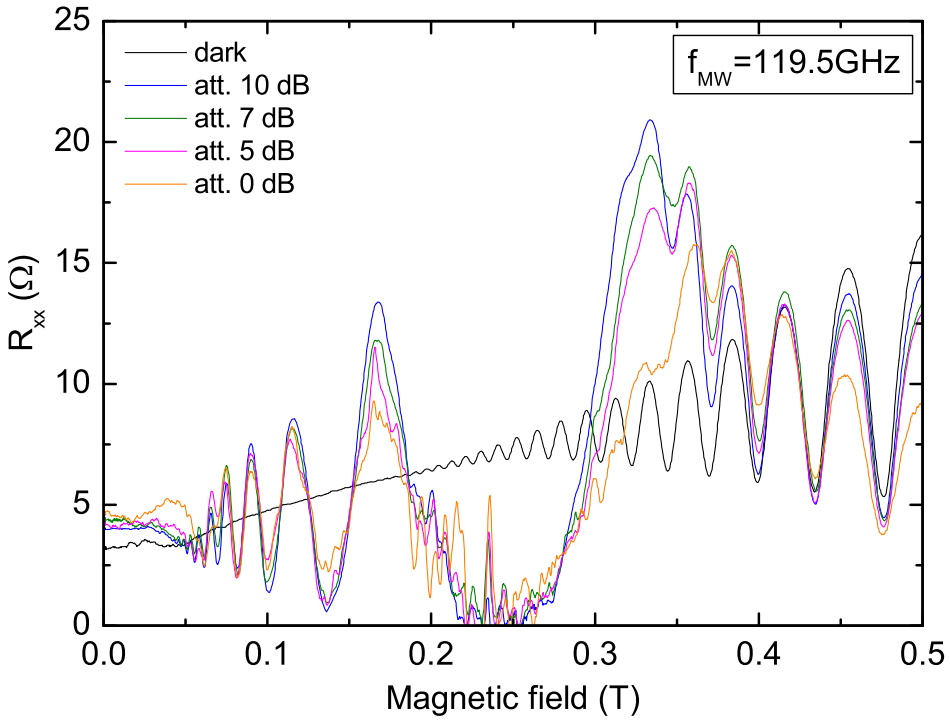

Figure 6.4: *Power dependence of the MIROs. The high power region. Maximum power at $0dB$ attenuation is 50mW. Microwaves frequency is f=119.5GHz. Sample is "Bell". See also Fig. 6.3.*

Microwave frequency

The periodicity of MIROs with ω/ω_c can be shown in the $\omega/\omega_c \sim 1/B$ scale. Such a representation is used in Figures 6.5–6.6 presenting the frequency dependence. This representation eliminates the obvious effect of scaling the period of the oscillations due to the frequency change.

The traces of R_{xx} measured under MW irradiation in the frequency range 80-110 GHz are presented in Figure 6.5. A "dark" trace of R_{xx} of a non irradiated sample is plotted for comparison. It can be seen that the MIROs are indeed periodic in the inverse magnetic field and when scaled as ω/ω_c there is no change in in the traces due to different MW frequency.

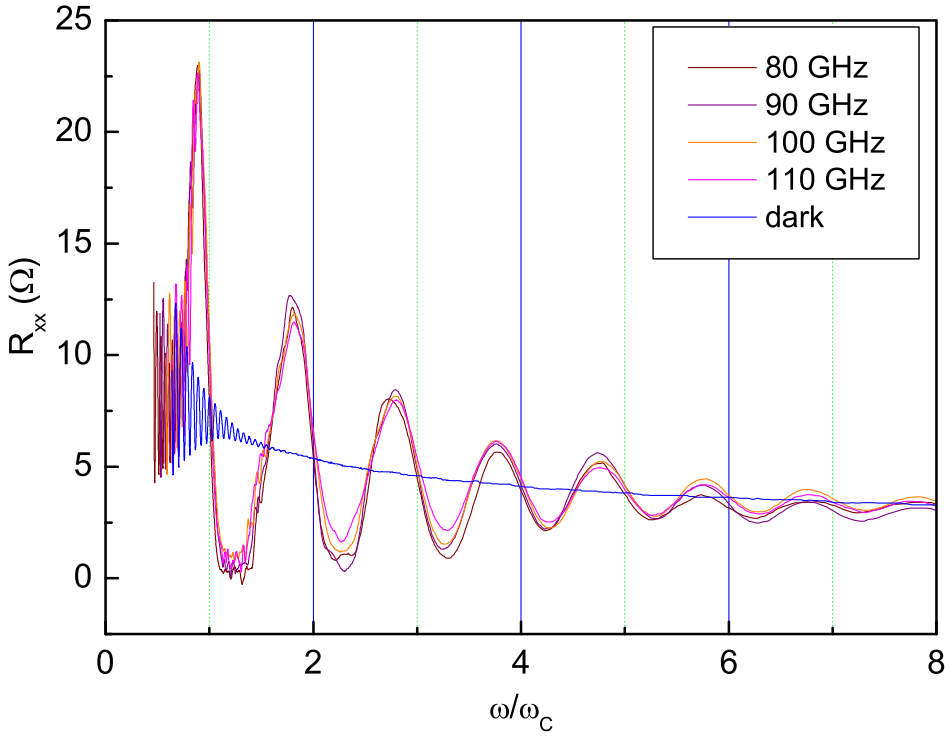

Figure 6.5: *Frequency dependence of the MIROs. The R_{xx} traces are plotted as a function of $\omega/\omega_c \sim 1/B$ with $m^* = 0.068$. T=1.5K. Constant power (attenuation 16dB-20dB) monitored by a bolometer. Sample is "Bell".*

However, when higher frequencies are used the MIROs show some change depending on the MW frequency. Figure 6.6, an analogous figure to Fig. 6.5, contains ΔR_{xx} traces of *higher frequency* microwave irradiation. The energy of microwaves changes from $160GHz$ to $226GHz$.

The decrease of the amplitude of the oscillations with the increase of the MW frequency is attributed to a lower attainable maximum MW power. The low–frequency MW power was kept constant by monitoring the response of a

bolometer placed in the vicinity of the sample. In the case of high frequencies the power that reach the sample and was detected on the bolometer was much lower even at the lowest attenuation.

Another more subtle effect is best visible in R_{xx} taken under $f = 226GHz$ irradiation. The oscillations are no longer sinusoidal and differ the most at $\omega/\omega_c = n + 1/2$. At these points the oscillations start to show plateaus due to Landau level separation (see below).

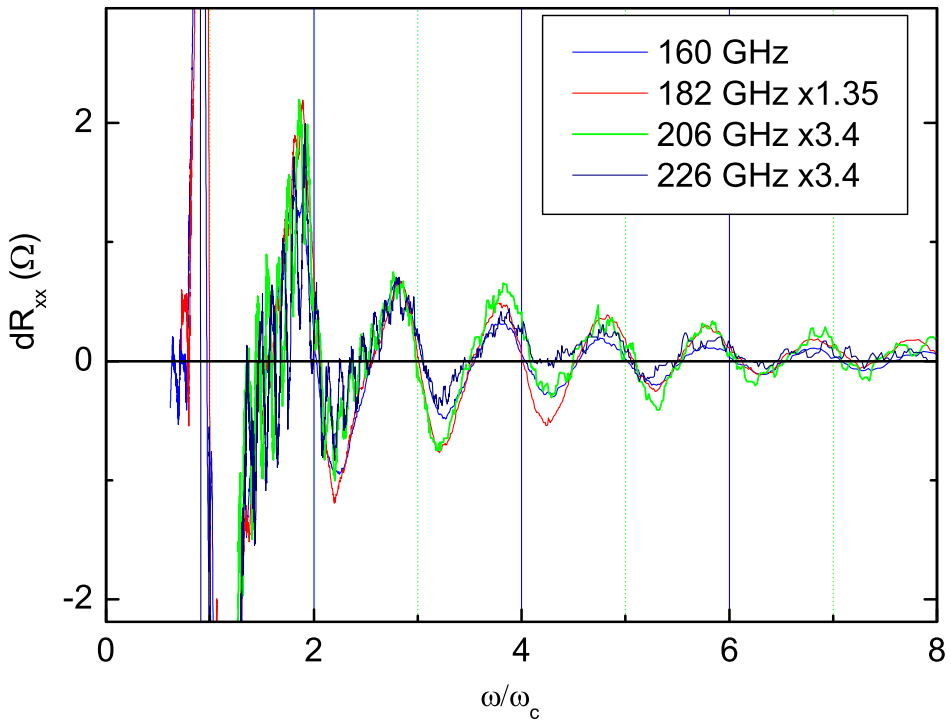

Figure 6.6: *Frequency dependence of the MIROs in the high frequency range. The R_{xx} traces are plotted as a function of $\omega/\omega_c \sim 1/B$ with $m^* = 0.068$. T=1.5K. Power is not constant. Sample is "Bell".*

6.2 Existing theories

The origin of the MIROs have not yet been established while several theoretical modes have been proposed. Most promising theories propose to explain the resistance oscillations as a result of an additional current due to the MW irradiation (*scattering model*) or as a result of the MW induced changes in the electron distribution function (*modified distribution function model*).

Following section will discuss briefly the main ideas behind the two models.

6.2.1 Scattering model

The model proposed by Durst et al. [5] suggest the appearance of an additional disorder-mediated current due to the MW irradiation. Depending on the ratio of the MW energy to the cyclotron energy the additional current flows either parallel or antiparallel to the applied electric field.

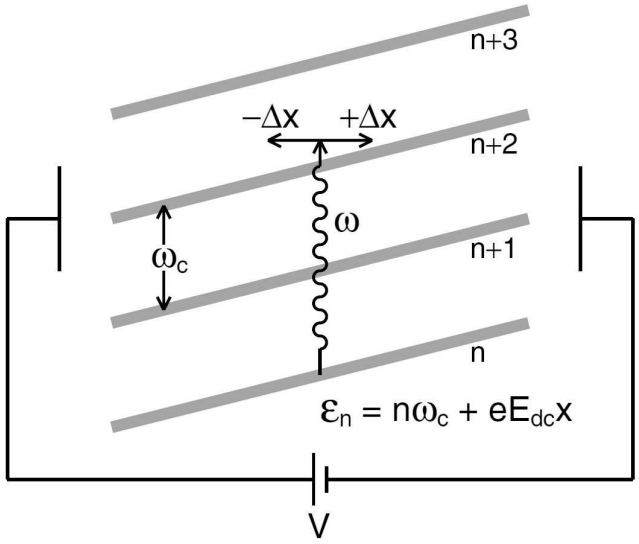

Figure 6.7: *The absorption of MW energy ω with a scattering parallel or antiparallel to the applied electric field that tilts the Landau levels (gray lines). Pictured at an arbitrary magnetic field. Figure from [5].*

Figure 6.7 presents a simplified picture of the proposed mechanism. During a transport measurement a small external electric field is applied to the 2DEG that tilts the Landau levels (gray lines) in the real space. The electron excitation provoked by the absorption process of MW radiation is accompanied by a scattering process.

The scattering process changes the position of the centre of the orbital motion of the excited electron. The change can be either with or against the direction of the applied electric field. It is argued that as the scattering probability is equal in both directions, the total current density due to the radiation will depend on the available empty final states.

The availability of the states will be determined by the energy of the radiation. As scattering over finite distances ($\pm\Delta x$) is preferred the resultant scattering direction will be determined by the position of the closest tilted Landau level in respect to the absorbed MW energy. If the absorbed MW energy ($\hbar\omega$) is a little less then the Landau level distance ($n \cdot \hbar\omega_c$) then the favoured direction is along the electric field and the conductivity increases.

In the other case, when $\hbar\omega \gtrsim n \cdot \hbar\omega_c$, the scattering in the direction opposite to the electric field is dominant and the conductivity decreases.

In the picture of the *radiation induced current* ΔJ, the total current measured during the transport experiment is the sum of J_0 due to the applied external field and ΔJ:

$$J = J_0 + \Delta J \tag{6.2}$$

In the presence of a scattering mechanism, the rate ($w_{\alpha'}$) at which the electron is scattered from an initial (without radiation) state α' to a final position $\mathbf{r}$ is:

$$w_{\alpha'}(\mathbf{r}) = 2\pi \sum_{\alpha} \left|\psi_\alpha(\mathbf{r})\right|^2 \delta(\epsilon_\alpha - \epsilon_{\alpha'} - \omega) \left| <\alpha|eE\hat{x}|\alpha'> \right|^2 \tag{6.3}$$

where $<\alpha|eE\hat{x}|\alpha'>$ is the matrix element of the electric dipole operator of the radiation field. As the occupancy of states must be included in the ΔJ, the factor $[n_F(\epsilon_{\alpha'}) - n_F(\epsilon_\alpha)]$ is introduced, where $n_F(\epsilon)$ is the initial Fermi distribution function.

Including the average over the disorder into $N(r,\epsilon)$, the additional current density can be written as:

$$\begin{aligned} \Delta J_x(\mathbf{R}) = -2\pi e \int d\epsilon d^2\Delta r [n_F(\epsilon) - n_F(\epsilon+\omega)] \times \\ N(r,\epsilon+\omega)N(r',\epsilon)M(r,r')\Delta x \end{aligned} \tag{6.4}$$

where $N(r,\epsilon) = \overline{\sum_\alpha |\psi_\alpha(r)|^2 \delta(\epsilon - \epsilon_\alpha)}$ is the average local density of states. $M(r,r') > 0$ is a function of Δr and is independent of the energies $\epsilon, \epsilon+\omega$.

The conductivity $\Delta\sigma_{xx}$ can be written as:

$$\Delta\sigma_{xx} \sim \frac{\partial\big(N(r,\epsilon+\omega)N(r',\epsilon)\big)}{\partial\Delta x} \tag{6.5}$$

if the electric field effect is limited to $N(r,\epsilon) = N(\epsilon - eEx)$, that is to tilting of Landau levels. Writing the density of states:

$$N(\epsilon) = N_0 + N_1 sin(2\pi\epsilon/\omega_c) \tag{6.6}$$

$\Delta\sigma_{xx}$ can be simplified to:

$$\Delta\sigma_{xx} \sim \left.\frac{\partial N}{\partial\epsilon}\right|_{\epsilon=\omega} \sim -sin(2\pi\omega/\omega_c) \tag{6.7}$$

The above simple model yields a correct phase and period of the microwave induced resistance oscillation with the assumption that $\rho_{xx} \approx \rho_{xy}^2 \sigma_{xx}$ where ρ_{xy} is independent of microwaves.

The critics (e.g. [6]) argue that impurity scattering is not a dominant mechanism as the amplitude of resistivity changes is much smaller than other effects (see next section). Other arguments against the *scattering* theory cite temperature independence of the scattering process.

6.2.2 Modified electron distribution function model

The theory by Dmitriev et al. [6] suggests an oscillatory part of the electron Fermi distribution due to microwave irradiation as the main reason for the observed resistance oscillations.

The measured longitudinal resistivity is connected to the photoconductivity by a relation: $\rho_{xx} \sim \rho_{xy}^2 \sigma_{xx}^{ph}$ (see Sec. 1.2, p. 6).

The conductivity, σ_{xx}^{ph} in the electric field applied for transport measurements is equal:

$$\rho_{xx} \sim \quad \sigma_{xx}^{ph} \quad = \quad \int d\varepsilon \; \sigma_{dc}(\varepsilon) \left[-\frac{\partial f(\varepsilon)}{\partial \varepsilon} \right] \tag{6.8}$$

where $f(\varepsilon)$ is the electron distribution function, and

$$\sigma_{dc}(\varepsilon) \quad = \quad \sigma_{dc}^{D} \cdot \widetilde{\nu}^2(\varepsilon) \quad = \quad \frac{e^2 \nu_0 v_F^2}{2\omega_c^2 \tau_{tr}} \cdot \frac{\nu(\varepsilon)}{\nu_0} \tag{6.9}$$

is the contribution of electrons with energy ε to the transport in the strong magnetic field approximation. σ_{dc}^{D} is the dc Drude conductivity, $\nu_0 = m/2\pi\hbar^2$ is the density of states at $B = 0T$, $\nu(\varepsilon)$ represents the oscillations in the density of states due to the Landau quantisation, and $\widetilde{\nu(\varepsilon)}$ is a dimensionless density of states parameter.

In case of *overlapping* Landau levels the latter can be described as:

$$\widetilde{\nu} \quad = \quad 1 - 2\,\delta \,\cos\left(\frac{2\pi\varepsilon}{\omega_c}\right) \tag{6.10}$$

$$\delta \quad = \quad exp\left(-\frac{\pi}{\omega_c \tau_q}\right) \ll 1 \tag{6.11}$$

where $\tau_q \ll \tau_{tr}$ is the single particle relaxation time in zero magnetic field. The resultant addition to the electron distribution function (f) is given by:

$$f_{osc}(\varepsilon) \quad = \quad \delta \frac{\omega_c}{2\pi} \cdot \frac{\partial f_T}{\partial \varepsilon} \cdot \sin\frac{2\pi\varepsilon}{\omega_c} \frac{\mathcal{P}_\omega \frac{2\pi\omega}{\omega_c} \sin\frac{2\pi\omega}{\omega_c} + 4\mathcal{Q}_{dc}}{1 + \mathcal{P}_\omega \sin^2\frac{\pi\omega}{\omega_c} + \mathcal{Q}_{dc}} \tag{6.12}$$

were $\mathcal{P}_\omega$, $\mathcal{Q}_{dc}$ are dimensionless units of the strengths of the oscillatory and static electric field, respectively. The reason for the oscillatory behaviour lies in the modulation of the density of states.

The schematic behaviour of the modulated distribution function is presented on the left–hand side of Figure 6.8. Even a small variation of the distribution function can affect the conductivity due to the derivative in Eq. 6.8.

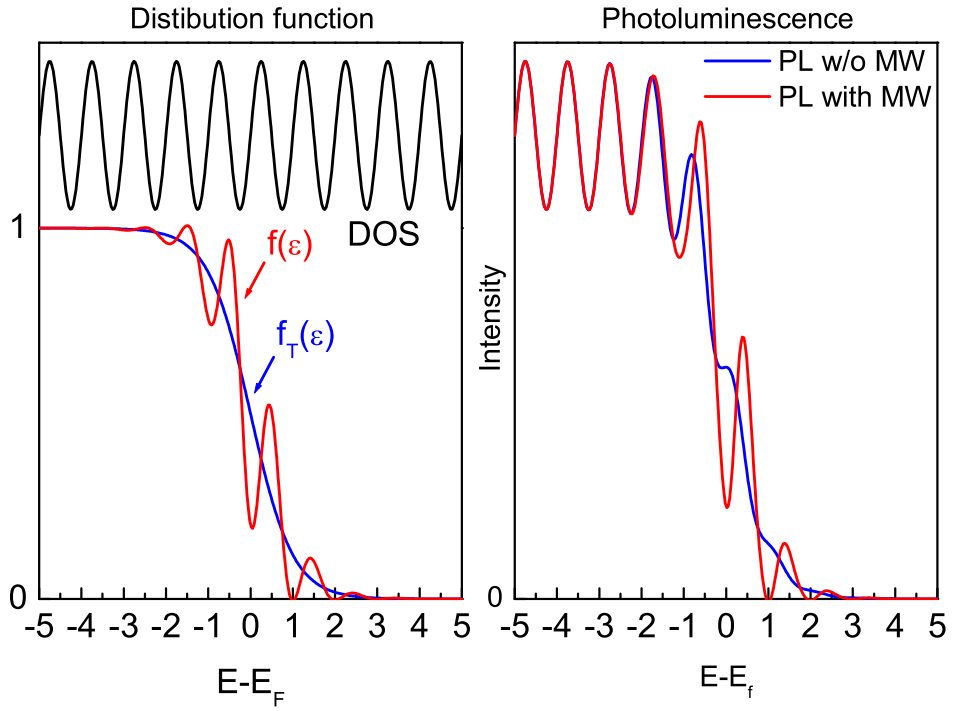

Figure 6.8: *Left. Modulation of electron distribution function due to microwave irradiation. Right. Schematic presentation of the expected effect of microwave irradiation on the photoluminescence from the Fermi edge due to the modulation of the electron distribution function*

Substituting the above equation into Eq. 6.8 the microwave induced correction to the conductivity due to the modulation of the electron distribution function can be obtained:

$$\frac{\sigma_{xx}^{ph} - \sigma_{dc}}{\sigma_{dc}} = -4\delta^2 \mathcal{P}_\omega \frac{\pi\omega}{\omega_c} \sin\frac{2\pi\omega}{\omega_c} \tag{6.13}$$

The result describes well the intensity, period and phase of the experimental results.

The result is also temperature dependent due to the proportionality of

$\mathcal{P}_\omega$ (and $\mathcal{Q}_{dc}$) to the inelastic relaxation time (τ_{in}) which is temperature dependent, in contrast to *scattering model*.

6.3 Experimental verification

The above theoretical models both correctly predict the period and phase of the oscillations. On the other hand, the two theories do not predict several issues, and disagree on others. Thus, the theoretical models need experimental clarification.

6.3.1 Transport

Separated Landau levels – MIROs plateaus

A sinusoidal waveform of the oscillations is predicted in the case of overlapping Landau levels. Both theories depend on a modulated density of states which in the low field regime is well described by the sine function. On the other hand, when the Landau levels are separated the density of states should be described by the sum of Lorentz functions and there exist regions of almost constant density of states in between Landau levels. The theories predict no change of the resistance due to microwaves in those regions.

Specifically, high frequency – high magnetic field experiments were performed. In contrast to the predictions, no clearly visible regions of constant dR_{xx} have been found . The only exception was the weak deviation from sine–like oscillations observed at MW frequency 226 GHz and presented in Figure 6.6 (p. 124) where a constant value of dR_{xx} *might* be present at $\omega/\omega_c = n + 1/2$, $n = 1, 3, 5 \ldots$.

Level width. The analysis of the thermal damping of SdH oscillations at different temperatures yields the damping parameter (D_T). Based on the assumption that the level width (Γ) is *constant* one can extract its value. (see Sec. 1.2.2, p. 8).

The lack of plateaus can be explained if one includes a magnetic field dependence of the Landau level width, namely the $\Gamma \sim \sqrt{B}$ broadening of the Landau levels. Introducing the field broadening one can state that the Landau levels are not yet fully separated in the range of applied magnetic fields.

DOS quantisation – Field damping

The existing theories imply that the Landau quantisation of the density of states is necessary for the MIROs phenomenon to occur. On the other hand, the MIROs are observed in very low fields where the SdH oscillations are no longer visible. This may put into question the role of the DOS quantisation.

It has been argued is Section 1.2.2, p. 8 that the quantisation of the DOS does not necessary imply the observation of the SdH oscillations as the amplitude depends on the thermal distribution of electrons. A very low temperature measurement (Fig. 1.8, p.11) of the SdH oscillations show that a well defined Landau level quantisation of the density of states persists to very low magnetic fields even if the SdH oscillations are no longer visible.

Additionally, one can compare the MIROs damping parameter with the thermal damping factor ($D_{th} = X_T/sinh(X_T)$, $X_T = 2\pi^2 kT/\hbar\omega_c$) in the standard expression for the amplitude of the SdH oscillations [7]:

$$\Delta\rho_{xx} \quad = \quad 4\rho_0 D_{th}(X_T) exp(-\pi/\omega_c\tau_q) \tag{6.14}$$

where τ_q is the quantum lifetime.

The determined order of magnitude of the $\tau_q \sim 10ps$ that corresponds to the value of the damping factor $\pi\hbar/\tau_q = 0.27meV$ is identical to the damping factor of the MIROs which was found to be $D_M = 0.3meV$ at T=1.6K. The damping factor is not sensitive to microwave power or frequency.

From the above consideration, the DOS quantisation is necessary for MIROs to occur, in accordance with both theoretical models.

Temperature damping

The dependence on temperature enters the equations in the form of τ_q/τ_{tr} in the *scattering* model and τ_{in}/τ_{tr} in the *modified distribution function* model.

The R_{xx} measurements yield a temperature damping parameter

$$A_M(T) \quad \sim \quad exp\Big(-0.7k_B T/\hbar\omega_c\Big) \tag{6.15}$$

which can be compared with the SdH temperature damping parameter:

$$D_{th} \quad = \quad \frac{X_T}{sinh(X_T)} \sim exp\Big(-X_T\Big) = exp\Big(-\frac{2\pi^2 k_B T}{\hbar\omega_c}\Big) \tag{6.16}$$

where $X_T = 2\pi^2 k_B T/\hbar\omega_c$. As the SdH damping parameter is much greater ($2\pi^2 \approx 20 \gg 0.7$) the thermal damping of SdH oscillations is much more effective than the thermal damping of MIROs [8].

Hall resistance

Neither model predict R_{xy} oscillations with observable amplitude due to microwave irradiation. Durst et al. [5] in the *scattering model* actually obtained the Hall resistivity oscillations of the same order of magnitude as magneto–resistance oscillations. The result was interpreted as an artifact in determination of τ_{tr}/τ where τ_{tr} is the transport lifetime and τ is the single

particle lifetime. It was stated that when the difference between the two quantities is taken into account, the R_{xy} oscillations are in fact negligible. Dmitriev et al. [6] in the comment to the discovery reported in Ref. [3] stated that the observed R_{xy} oscillations can not be explained by the changes in the electron distribution function and suggested the changes were due to weak 2D electron concentration variations with ω/ω_c.

6.3.2 Microwave absorption

The common starting point of the above theoretical models is the microwave absorption by the 2DEG. A following simplistic model can be used to determine the expected MW absorption. The 2D density of states quantised by the magnetic field into discrete Landau levels are modelled by a sine function. This is sufficient for the basic reasoning, as the proper description of Landau level broadening by Gaussian or Lorentz functions gives similar general results [9]. The thermal distribution of electrons is described by the Fermi function.

The absorption process of microwaves of energy $\hbar\omega$ involves available electrons at energy ϵ whose number is determined by the DOS and the thermal population $D(\epsilon)f(\epsilon)$ and depends on the availability of empty states at energy $(\epsilon + \hbar\omega)$ which is determined by $D(\epsilon + \hbar\omega)\big[1 - f(\epsilon + \hbar\omega)\big]$.

Including a symmetric process of stimulated emission the absorption can be written as:

$$\begin{aligned} Absorption \;\sim\; \int d\epsilon \Big\{ & D(\epsilon)f(\epsilon) \cdot D(\epsilon + \hbar\omega)\big[1 - f(\epsilon + \hbar\omega)\big] \\ & - D(\epsilon + \hbar\omega)f(\epsilon + \hbar\omega) \cdot D(\epsilon)\big[1 - f(\epsilon)\big] \Big\} \end{aligned} \tag{6.17}$$

where $D(\epsilon)$ is the density of states at energy ϵ, $f(\epsilon)$ is the electron distribution function. The above can be written as:

$$Abs_{NR} \;\sim\; \int d\epsilon \; D(\epsilon)D(\epsilon + \hbar\omega)\big[f(\epsilon) - f(\epsilon + \hbar\omega)\big] \tag{6.18}$$

According to the above equation, the absorption of microwaves at fixed frequency ω is an oscillating function of the magnetic field (if the Landau level modulation of the density of states is sufficiently pronounced). This effect is illustrated in Figure 6.9. One should note here that the broadening of the oscillations shown in Figure 6.9 is determined by the Γ_{LL}, i.e. the broadening of the Landau levels.

The description of microwave absorption in terms of Eq. 6.18 takes into account the occupation factors but completely ignores the optical selection rules.

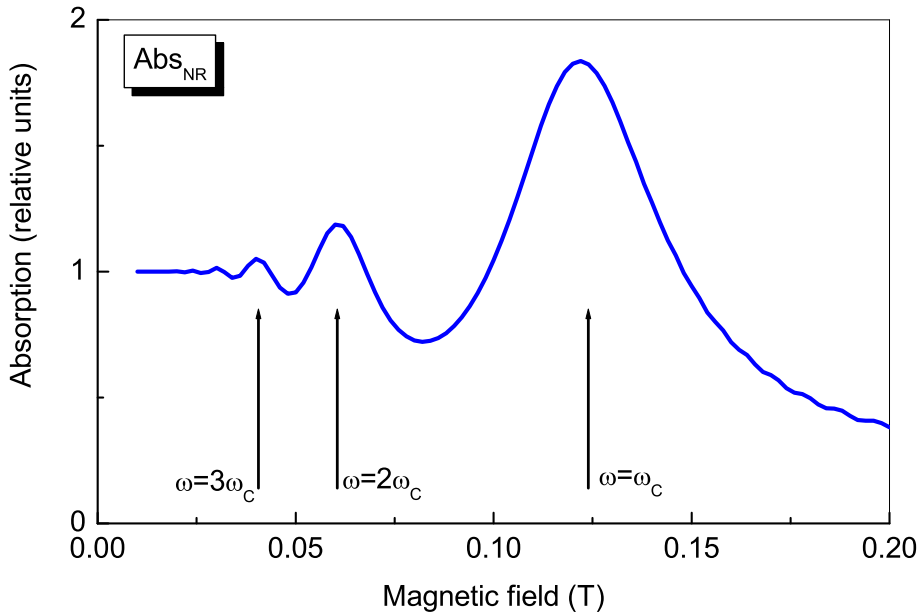

Figure 6.9: *Calculated non–resonant microwave absorption by a 2DEG with modulated DOS. (see Eq. 6.18)*

Cyclotron resonance. On the other hand, there exists a well established effect of the cyclotron resonance absorption which obviously should be taken into account when considering the microwave absorption of a 2DEG in a magnetic field. Within a simple model the effect of cyclotron resonance absorption can be described by a single Lorentz peak:

$$Abs_{CR} \sim \frac{1}{1+\left(\frac{\hbar\omega-\hbar\omega_c}{\Gamma_{CR}}\right)^2} \tag{6.19}$$

where Γ_{CR} is the broadening parameter which in general depends on mobility as well as concentration of the 2DEG.

At this point it is important to note that Γ_{CR} is expected to be smaller than the broadening parameter for Landau levels Γ_{LL} which on the other hand affects the absorption process described by Eq. 6.18.

Combination of processes

To combine both absorption processes in a very crude and phenomenological approximation one could think about two approaches.

Independent. The first approach is to assume that both processes are *independent* and that the resulting absorption is just a sum of both processes:

$$Abs_1 \;=\; \alpha \cdot \frac{1}{1+\left(\frac{\hbar\omega-\hbar\omega_c}{\Gamma_{CR}}\right)^2} \;+\; \beta \cdot \int d\epsilon\; D(\epsilon)D(\epsilon+\hbar\omega)\left[f(\epsilon)-f(\epsilon+\hbar\omega)\right] \tag{6.20}$$

where α and β are arbitrary and unknown coefficients which account for relative weight of each absorption process.

Optical selection rules in MIROs The second approach consists of an attempt to introduce the optical selection rule into Eq. 6.18. In a simple way, one could just multiply Eq. 6.18 and Eq. 6.19

$$\begin{aligned} Abs_2 \;&=\; \gamma \cdot \int d\epsilon\, D(\epsilon)D(\epsilon+\hbar\omega)\left[f(\epsilon)-f(\epsilon+\hbar\omega)\right] \cdot \frac{1}{1+\left(\frac{\hbar\omega-\hbar\omega_c}{\Gamma_{CR}}\right)^2} \\ Abs_2 \;&=\; \gamma \cdot \frac{1}{1+\left(\frac{\hbar\omega-\hbar\omega_c}{\Gamma_{CR}}\right)^2} \cdot \int d\epsilon\; D(\epsilon)D(\epsilon+\hbar\omega)\left[f(\epsilon)-f(\epsilon+\hbar\omega)\right] \end{aligned} \tag{6.21}$$

where γ is a proportionality factor.

Possible forms of the magnetic field dependence of the microwave absorption at a given frequency expected for the first and the second approach are shown in Figure 6.10 and Figure 6.11, respectively.

The second phenomenological approach is somehow consistent with the theoretical model presented by Dmitriev et al. [6, 9] (see Figure 6.12).

As can be seen in these figures, the absorption weight of the cyclotron resonance replicas with respect to the main peak is expected to be vanishingly small within the second approach. However, for the case of the first approach this ratio depends on relative strength of both absorption processes and can be arbitrarily chosen, depending on the actual value of α/β.

The two proposed approaches may have different consequences on the results of direct absorption measurements, which are presented in the following section.

Experiment

Figures 6.13, top and 6.14, top present the derivative spectra of microwave absorption measured in two 2DEG systems with different mobilities. The high mobility ($\sim 4 \cdot 10^6 cm^2/Vs$) *M1707* heterojunction and the lower mobility ($\sim 2 \cdot 10^6 cm^2/Vs$) *NTT-A* quantum well sample have been measured. The two samples have been chosen for their different transport properties.

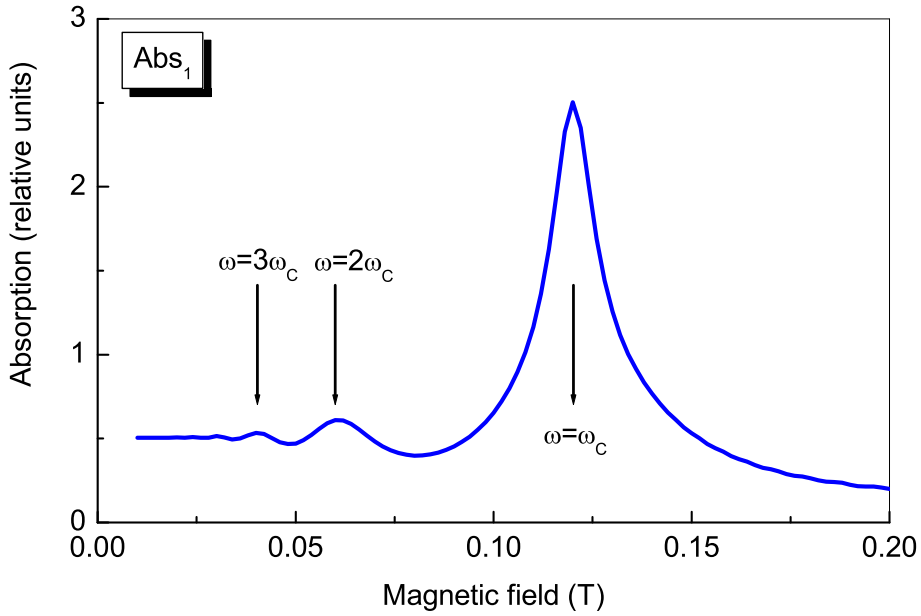

Figure 6.10: *Calculated microwave absorption by a 2DEG with modulated DOS for the first approach of independent absorption mechanisms.* $\alpha/\beta = 1$ *(See Eq. 6.20)*

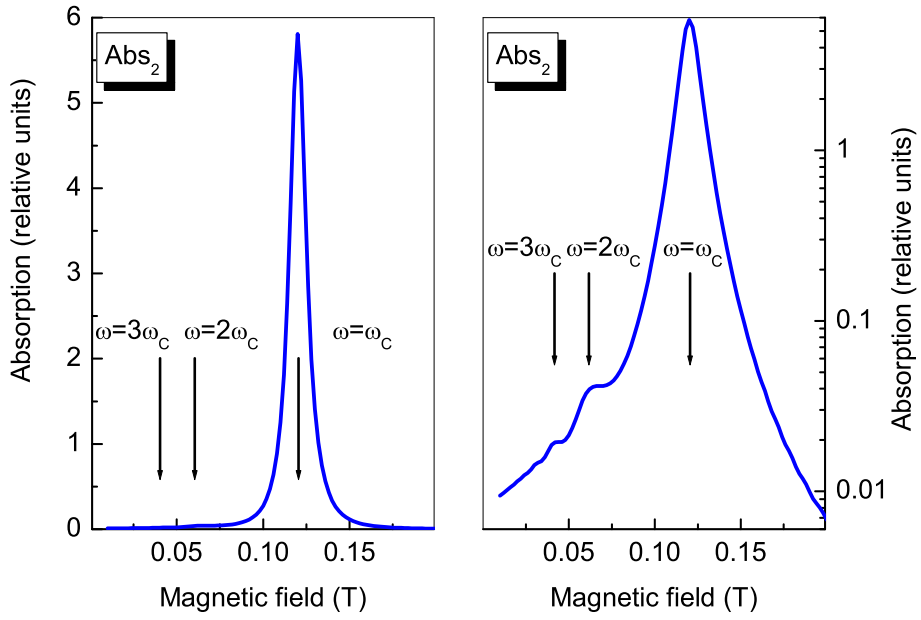

Figure 6.11: *Calculated microwave absorption by a 2DEG with modulated DOS for the second approach. Results presented in linear (left) and logarithmic (right) scales for better comparison. (See Eq. 6.21)*

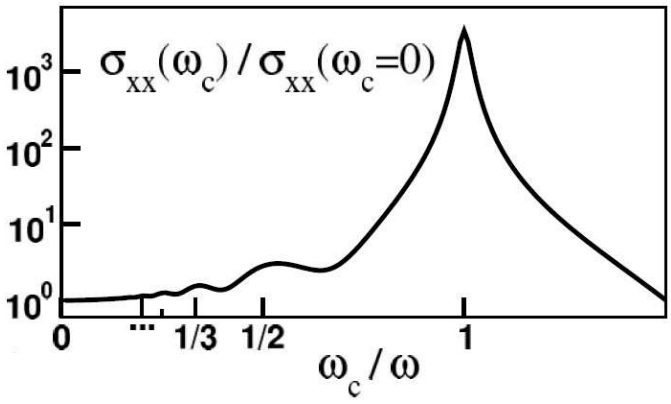

Figure 6.12: *Changes of conductivity due to microwave irradiation at cyclotron resonance harmonics calculated by Dmitriev et al. [9].*

The *M1707* sample shows much more pronounced MIROs than the lower mobility *NTT-A* sample.

The top traces present integrated spectra that reflect the microwave absorption. Both absorption spectra, regardless of the difference in the 2DEG mobility, present a cyclotron resonance peak at the corresponding magnetic field.

Remarkably, the higher mobility 2DEG absorption spectrum (Fig. 6.13) shows a complicated structure on the low field side of the cyclotron resonance. The observed low field absorption peaks might originate from the second and third harmonics of the cyclotron resonance. For comparison, arrows denoting the expected field positions of the cyclotron resonance harmonics were plotted.

On the other hand, the absorption curve of the NTT-A sample with lower mobility does not show features that could be identified with higher harmonics of the cyclotron resonance. Except from the cyclotron resonance signal only an additional low field shoulder close to the resonance is observed.

Discussion

The transport measurements show that MIROs are much more pronounced in the high mobility M1707 sample than in the low mobility NTT-A sample. This observation correlate with the measurement of the low field absorption of microwaves in the M1707 sample.

The observation of the cyclotron resonance absorption and the absorption peaks around the harmonics of the resonance that have comparable intensity suggest that the first approach to the microwave absorption modelling is more appropriate. The view of the two absorption processes being independent of each other better describes the direct microwave absorption

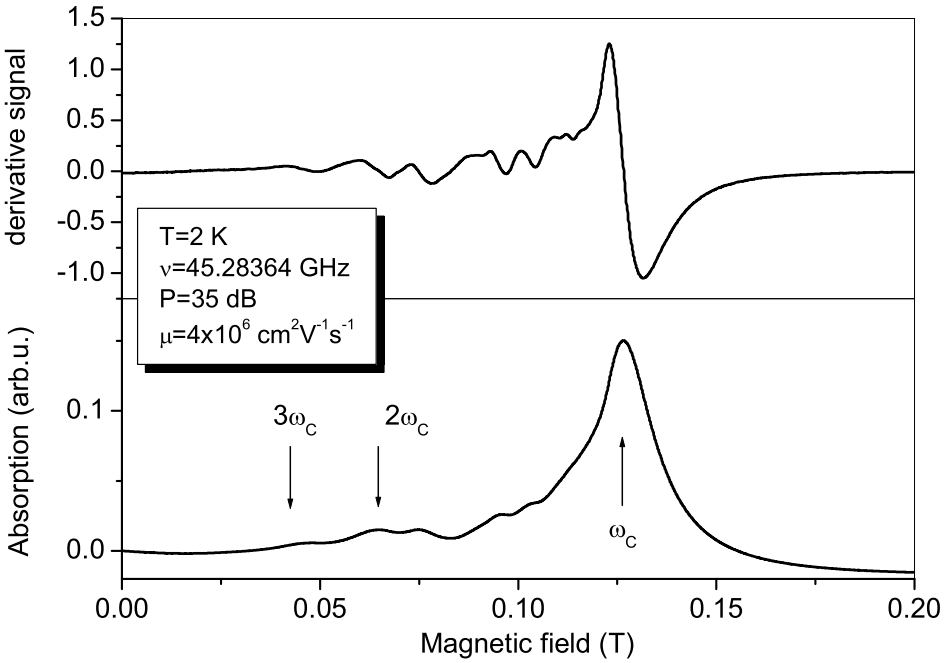

Figure 6.13: *Derivative (top) and integrated (bottom) spectrum of microwave absorption in the M1707 sample. The arrows point at magnetic fields where* $\omega = \omega_c$, $\omega = 2\omega_c$, $\omega = 3\omega_c$ *Maximal power is 5mW.*

data.

This viewpoint is in agreement with recent work by Smet et al. [10] on the polarisation dependence of the microwave photoconductivity. It has been found that while cyclotron resonance measured in transport depends on the polarisation of the irradiating microwaves, the simultaneously measured MIROs do not show any change.

To relate the referenced experiment to the terminology used here, the MIROs can be associated with the Abs_{NR} process (presumably not following the polarisation rules) but the Abs_{CR} could follow its characteristic polarisation rules.

Within the framework of the second approach, the well–known polarisation rules for the cyclotron resonance absorption would imply that MIROs should be observed only in CR-active configuration. The first approach does not necessarily imply such behaviour.

One should note the deficiency of the simple model. Eq. 6.20 describes two absorption processes, a known one (cyclotron resonance) and an unknown (non–resonant). The relative magnitudes of the processes, namely the ratio α/β is an unknown parameter.

A phenomenological examination allows to conclude that the α/β ratio depends on different parameters. From the above results it is clear that it

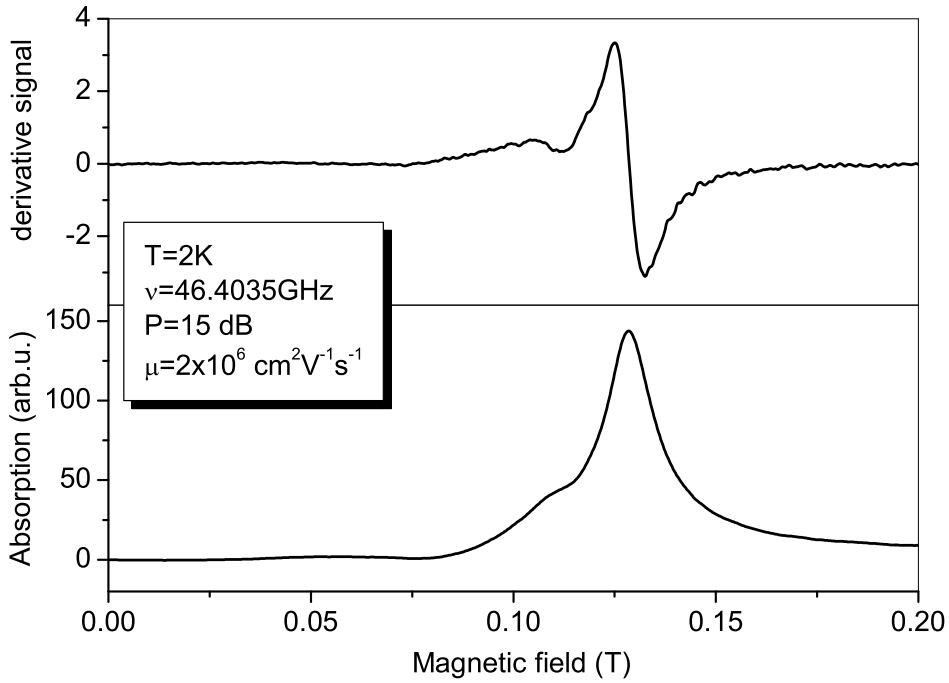

Figure 6.14: *Derivative (top) and integrated (bottom) spectrum of microwave absorption in in the NTT-A sample.*

depends on the mobility of the 2DEG, but also on the microwave frequency. Figure 6.15 presents frequency dependent measurements of the MIROs in the range of 80 - 226 GHz (green curves). The successive increase of the frequency gradually changes the ratio of the microwave cyclotron absorption (CR) to the resistance oscillations at higher harmonics (MIROs). Thus, a change of the α/β ratio is observed.

In two extreme limits, the traces are diametrally different. At low frequencies the cyclotron resonance has the same magnitude as MIROs while at the highest frequency measured the MIROs are nearly negligible as compared to the CR related minimum.

6.4 Conclusions

The experimental results of a recently discovered effect that manifests itself in a form of microwave induced resistance oscillations (MIROs) have been presented here along with two theoretical models.

From the comparison of transport measurements showing MIROs and direct microwave absorption measurements showing cyclotron resonance and its harmonics, the existence of two separate absorption processes was deduced.

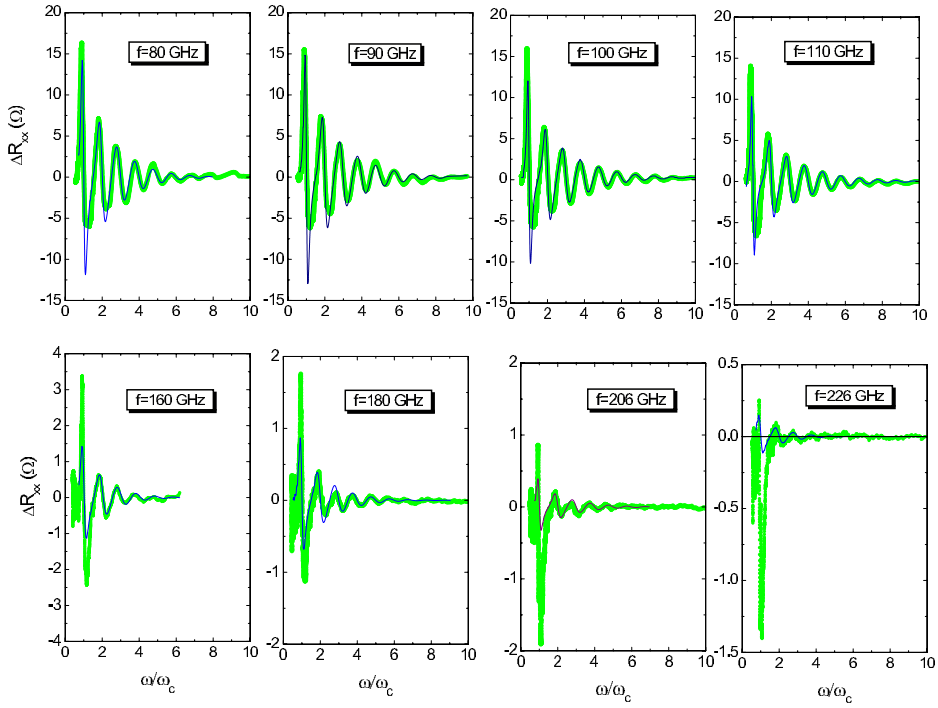

Figure 6.15: *Frequency dependence of the MIROs. The R_{xx} traces are plotted as a function of $\omega/\omega_c \sim 1/B$. T=1.5K. Power is not constant. Sample is "Bell" [11].*

The non–resonant absorption, depending only on the availability of the states taking part in the process, is more pronounced in the transport measurements in the form of microwave induced oscillations while the observation of the well known cyclotron resonance is enhanced in the measurements of the direct microwave absorption.

The relative intensities of absorption at cyclotron resonance and at its harmonics suggest that the view of the two absorption processes being independent of each other better describes the direct microwave absorption data.

The MIROs can be associated with the non–resonant absorption process that presumably does not follow the polarisation rules, in contrast to the resonant absorption that follows characteristic cyclotron resonance polarisation rules ($\Delta n = 1$).

Additionally, the fascinating gradual changeover from transport traces reflecting MIROs at low microwave frequencies, to a nearly cyclotron – resonance – only transport trace at high frequency has been observed.

Bibliography

[1] M. A. Zudov, R. R. Du, J. A. Simmons, and J. L. Reno, Phys. Rev. B **64**, 201311 (2001).

[2] R. G. Mani, J. H. Smet, K. von Klitzing, V. Narayanamurti, W. B. Johnson, and V. Umansky, Nature **420**, 646 (2002).

[3] S. A. Studenikin, M. Potemski, P. T. Coleridge, A. Sachrajda, and Z. R. Wasilewski, Solid State Commun. **129**, 341 (2004).

[4] R. G. Mani, V. Narayanamurti, K. von Klitzing, J. H. Smet, W. B. Johnson, and V. Umansky, Phys. Rev. B **69**, 161306 (pages 4) (2004).

[5] A. C. Durst, S. Sachdev, N. Read, and S. M. Girvin, Phys. Rev. Lett. **91**, 086803 (2003).

[6] I. A. Dmitriev, M. G. Vavilov, I. L. Aleiner, A. D. Mirlin, and D. G. Polyakov, Phys. Rev. B **71**, 115316 (pages 11) (2005).

[7] P. T. Coleridge, Phys. Rev. B **44**, 3793 (1991).

[8] S. Studenikin, M. Potemski, A. Sachrajda, M. Hilke, L. N. Pfeiffer, and K. W. West, Phys. Rev. B **71** (2005), accepted and cond-mat/0411338.

[9] I. A. Dmitriev, A. D. Mirlin, and D. G. Polyakov, Phys. Rev. Lett. **91**, 226802 (pages 4) (2003).

[10] J. H. Smet, B. Gorshunov, C. Jiang, L. Pfeiffer, and K. West, cond-mat/0505183 (2005).

[11] S. A. Studenikin, M. Byszewski, D. K. Maude, M. Potemski, A. Sachrajda, M. Hilke, L. Pfeiffer, and K. W. West (2005).

Chapter 7

Conclusions

Optical studies of a two–dimensional electron gas in magnetic fields have been presented. The two-dimensional electron gas in the regime of the fractional quantum Hall effect has been studied by photoluminescence and inelastic light scattering measurements. The obtained results allow to observe, even in the raw data, the photoluminescence analogue of the transport quantum Hall plateaus.

The effect of electron interactions in the 2DEG results in the fractional quantum Hall effect which has been thoroughly studied by the transport experiments in the past. The most pronounced fractional filling factor $\nu = {}^1\!/_3$ was discovered first, after which a whole range of fractions were observed. The symmetry and shape of transport features similar to integer filling factor suggested the introduction of a model of composite fermions – non interacting new quasi–particles.

Until now, the optical experiments did not allow to study the electron interactions in the whole range of the fractional quantum Hall effect. The previous works reported photoluminescence changes only at particular fractional filling factors.

Present work, reports the observation of the family of the $\nu = {}^1\!/_2$ fractional quantum Hall states, in the same sample, that are clearly visible in raw photoluminescence data (observed fractions include $\nu = {}^1\!/_3$, ${}^2\!/_5$, ${}^3\!/_7$, ${}^3\!/_5$, ${}^2\!/_3$, and $\nu = 1$). These data are analogous to magneto–resistivity traces of a high quality sample. The observed composite fermion symmetry of fractional states distributed on both sides around $\nu = {}^1\!/_2$ is a familiar picture in R_{xx} data but novel in optical experiments.

The observed changes of the emission energy were attributed to the changing state of the 2DEG based on the temperature dependence measurements. The effect can be explained qualitatively in the picture of electron screening as follows. At fractional filling factors the incompressibility of the 2DEG results in the inability of the electrons to screen the optically induced hole and the emission energy is higher. The lowering of the emission energy

outside of the incompressible state of the 2DEG has been explained by the ability of the 2D electrons to respond to the hole positive potential.

The theoretical calculations of the $\nu = 1/3$ case attributed the high energy emission at fractional filling factor to the emission from a quasi–exciton and the emission outside of a fractional filling factor to an emission from a charged quasi–exciton complex that binds a quasi–particle.

The broad magnetic field range where the higher emission is observed has been thus interpreted as an analog of a Hall plateau that is usually observed in transport. It has been confirmed by simultaneous transport and photoluminescence measurements around $\nu = 1/3$. Those measurements were preceded by careful studies of the effect of illumination on transport properties, which change dramatically during the sample illumination. The changes were accompanied by equally dramatic changes of the 2D electron density. Finally, a stable high density state, corresponding to the state detected in the optical measurements, has been found.

The temperature dependence of the photoluminescence shows the emission plateau narrowing with increasing temperature, an effect known in transport measurements. The low field jump of the emission energy at the plateau boundary, attributed to the occurrence of quasi–particles that form charged quasi–excitonic complexes of higher binding energy, moves to higher fields when the temperature is increased. This is clearly visible around filling factor $\nu = 1/3$.

The measurements in the fractional quantum Hall regime were preceded by careful characterisation of the samples. The standard parameters of a 2DEG, such as electron concentration and reduced effective mass, were determined from optical and transport experiments.

The three quantum well samples were classified into different categories depending on the ratio of electron – electron and 2DEG – hole interactions which determined the characteristic features of the photoluminescence for each sample. The influence of the well width was discussed on a previously studied example of filling factor $\nu = 1$. The two wider quantum wells were classified as having comparable magnitudes of the ratio of the 2D electron interaction and the electron – valence band hole interaction.

The narrow quantum well has electron – hole interaction much bigger than 2DEG correlations, thus the hole binds an electron and forms a neutral or charged exciton complex. In both cases, its photoluminescence has an excitonic character and is nearly insensitive to fractional quantum Hall states of the 2DEG.

On the other hand, the luminescence from the two other quantum wells is sensitive to the 2DEG state and displays different behaviour around filling factor $\nu = 1$. The *blueshift* in the case of the 20nm quantum well sample signifies that the electron – hole interaction is comparable but bigger than the electron – electron interaction in the 2DEG. The *redshift* in the case of the broader 50nm quantum well signifies the opposite case, the electron –

hole interaction is also comparable but weaker then the electron interactions. This, potentially the most interesting sample, could not be studied at all fractions because of technical reasons — bulk GaAs emission was in overlap with the 2DEG emission. The electron – electron interactions are similar in both samples because of similar sample parameters, while the electron – hole interaction is changed between the two samples due to different spatial separation of the hole and the 2DEG plane.

The photoluminescence of the 20nm quantum well shows a doublet structure. The comparison of the results of the temperature dependence measurements with theoretical calculations at $\nu = {}^{1}/_{3}$ allows us to assign the low energy line to an emission from an excited state of the quasi–exciton.

The inelastic light scattering experiments indicate the observation of a spin–flip process, and a scattering process to the Fermi energy of composite fermions, as two signals observed from the 2DEG. Additionally, a Raman scattering spin–flip process in a bulk GaAs has been identified.

The measurements of light scattering resulted in a slightly different 2D electron concentration, that did not correspond to the photoluminescence measurements, probably because of a higher intensity of excitation. Also, the simultaneous observation of a stronger photoluminescence emission in the energy range of the scattered light hindered the measurements of the light scattering signals.

The second part of the thesis described the recently discovered behaviour of the 2DEG properties under microwave irradiation in low magnetic fields. The 2DEG transport trace in the magnetic fields deviates strongly from the well known Shubnikov – de Haas oscillations when irradiated with microwaves. It exhibits a series of vanishing resistance states that are governed by the ratio of the microwave frequency to the cyclotron frequency.

The dependence of transport properties on microwave power and frequency has been presented. A gradual changeover of resistance traces from MIROs to cyclotron resonance – like was presented in the frequency dependence data.

Also, results of direct microwave absorption were presented for two samples with different electron mobilities. The lower mobility sample showed only a cyclotron absorption peak while the high mobility sample exhibited additional absorption peaks around cyclotron resonance harmonics. Different absorption spectra are accompanied by differences in resistance traces as the high mobility sample shows the MIROs much more pronounced.

The measurements allowed to deduce the existence of two separate absorption processes. The non–resonant absorption being better pronounced in the transport measurements is visible as MIROs. The MIROs associated with the non–resonant absorption process, presumably do not follow the polarisation rules. In contrast, the resonant absorption, better visible in the measurements of the direct microwave absorption should follow characteris-

tic cyclotron resonance polarisation rules.